

**RL-TR-96-115**  
**In-House Report**  
**OCTOBER 1996**



# **PHOTONIC TRUE TIME DELAY BEAMFORMER FOR A 20 ELEMENT L-BAND PHASED ARRAY**

**Paul M. Payson, John E. Malowicki, Herbert W. Klumpe III,  
Edward N. Toughlian, Capt.(Ret), USAF (Rome Laboratory),  
and Henry Zmuda (University of Florida)**

*APPROVED FOR PUBLIC RELEASE; DISTRIBUTION UNLIMITED.*

19961125 037

**Rome Laboratory  
Air Force Materiel Command  
Rome, New York**

**DTIC QUALITY INSPECTED 3**

## **Abstract**

A phased array is a directive antenna made up of individual radiating elements which generate a radiation pattern whose shape and direction are determined by the relative phases and amplitudes of the currents at the individual elements. Current state-of-the-art phased array radars implement electronic phase shifters for beamforming. The limitation of the phase shifters becomes apparent if multiple frequencies are transmitted simultaneously. The energy associated with the different frequencies will point in different directions in the antenna's far field causing an increase in beamwidth. This phenomena, called squint, restricts the phase shift approach to narrowband operation.

A true time delay line based on an optical heterodyning technique is used to generate properly phased signals enabling wide bandwidth operation. The theory, design, development, testing and analysis for photonicly controlling a 20 element, wide bandwidth (200 MHz) L-Band phased array radar are presented.

## Table of Contents

Abstract .....	i
Table of Contents .....	ii
List of Figures.....	iv
List of Figures from Appendixes .....	vi
List of Tables.....	vii
List of Tables from Appendixes.....	viii
Acknowledgments .....	ix
Preface .....	x
List of Symbols, Abbreviations, and Acronyms.....	xi
<b>1.0 Introduction.....</b>	<b>1</b>
<b>2.0 Background .....</b>	<b>3</b>
2.1 Theory of Phased Array Beamforming.....	3
2.2 Beam Squint .....	5
<b>3.0 Photonic Processing for Phased Array Applications .....</b>	<b>7</b>
3.1 Photonic Processing Fundamentals.....	7
3.1.1 Operation of an AO Cell.....	7
3.1.2 The Optical Heterodyne Process .....	9
3.2 Photonic Approach to Phased Array Beamforming for Narrowband Applications .....	11
3.3 Photonic Approach to Phased Array Beamforming for Broadband Applications .....	13
3.3.1 A Spatially Integrated Approach .....	15
3.3.2 Other Considerations .....	18
3.3.3 Feature Resolution.....	19
3.3.4 Delay Resolution.....	23
<b>4.0 System Description.....</b>	<b>26</b>
4.1 Electronic System .....	26
4.2 Optical System (as designed) .....	27
4.2.1 Front End .....	29
4.2.2 TTD Replication and Collimation Subsystem .....	30
4.2.3 TTD Selection and Feedback Subsystem .....	31
4.3 Antenna System .....	33
4.4 Computer Control System (as designed).....	34
4.5 Optical System (As Built) .....	36
4.6 Computer Control System (As Built).....	39
<b>5.0 Experimental Results.....</b>	<b>41</b>
5.1 Experimental Set-Up.....	41
5.2 The Experiment.....	42
5.3 Data.....	43
5.3.1 Single Channel Data .....	43
5.3.2 Twenty Channel Data.....	46
5.3.3 Five Element Line Array Data and Beam Patterns .....	46
5.3.3.1 Five Element Array Steered to Broadside.....	48
5.3.3.2 Five Element Array Steered to 30 Degrees .....	52
5.3.3.3 Five Element Array Steered to 60 Degrees .....	56

5.3.4	Summary of the Performance with Respect to Beam Squint .....	60
5.3.5	Phase Drift.....	62
5.3.6	Performance of the Integrated System vs. a Free Space Predecessor.....	63
<b>6.0</b>	<b>Discussions and Conclusions.....</b>	<b>65</b>
<b>7.0</b>	<b>Recommendations &amp; Future Work.....</b>	<b>69</b>
<b>8.0</b>	<b>References .....</b>	<b>70</b>
	<b>Appendices.....</b>	<b>following page 71</b>

## List of Figures

Figure 1.	A steered phased array antenna.....	4
Figure 2a.	Acousto-optic cell theory of operation configuration for frequency up shift.....	8
Figure 2b.	Acousto-optic cell theory of operation configuration for frequency down shift.....	8
Figure 3.	Optical heterodyne system.....	10
Figure 4.	Integrated narrow band high packing density phased array beamforming system.....	11
Figure 5.	Binary optic.....	12
Figure 6.	Delay line theory.....	14
Figure 7.	Electrostrictive 20 element deformable mirror device.....	16
Figure 8.	Integrated 20 element delay line system.....	17
Figure 9.	One pixel of a liquid crystal beamsteering device.....	19
Figure 10.	Integrated L-band photonic delay line system.....	20
Figure 11.	Feature resolution system to observe system amplitude transfer function.....	20
Figure 12.	Photonic delay line amplitude transfer function.....	21
Figure 13.	Simple optical system demonstrating the focused spot size (d) for an input beam of diameter (D).....	22
Figure 14.	Feature resolution system to observe system impulse response.....	22
Figure 15.	Input signal to photonic delay line for impulse response generation.....	23
Figure 16.	Impulse response of photonic delay line.....	23
Figure 17.	DMD pixel tilt.....	24
Figure 18.	Displacement of beam inside the AO cell ( $D_x$ ) due to tilt of the mirror element ( $D_f$ ).....	25
Figure 19.	Test and measurement equipment.....	26
Figure 20.	Mechanical Drawing of Optical Breadboard Design.....	28
Figure 21.	Front End Subsystem.....	29
Figure 22.	TTD replication and collimation subsystem.....	31
Figure 23.	TTD selection and feedback subsystem.....	32
Figure 24.	L-band antenna back plane.....	34
Figure 25.	Computer control system.....	36
Figure 26.	Spot locations of the five channels at the focal plane of the feedback loop.....	38
Figure 27.	Experimental set-up.....	42
Figure 28.	Phase vs. frequency for a single channel of an ideal TTD system.....	44
Figure 29.	Phase vs. frequency for a single channel of the Photonic TTD system.....	44
Figure 30.	Magnitude vs. frequency for a single channel of the Photonic TTD system.....	45
Figure 31.	Magnitude vs. frequency for all twenty channels of the Photonic TTD system.....	47
Figure 32.	Phase vs. frequency for all twenty channels of the Photonic TTD system.....	47

Figure 33.	Phase vs. frequency for a five element delay line of an ideal TTD system. ....	48
Figure 34.	Phase vs. frequency for a five element delay line of the Photonic TTD system. ....	49
Figure 35.	Magnitude vs. frequency for a five element delay line of the Photonic TTD system. ....	49
Figure 36.	Beam patterns at 1.25 GHz of the Photonic TTD system and the perfect phase shifter. ....	50
Figure 37.	Beam patterns at 1.275 GHz of the Photonic TTD system and the perfect phase shifter. ....	51
Figure 38.	Beam patterns at 1.3 GHz of the Photonic TTD system and the perfect phase shifter. ....	52
Figure 39.	Phase vs. frequency for a five element delay line of an ideal TTD system. ....	53
Figure 40.	Phase vs. frequency for a five element delay line of the Photonic TTD system. ....	53
Figure 41.	Magnitude vs. frequency for a five element delay line of the Photonic TTD system. ....	54
Figure 42.	Beam patterns at 1.25 GHz of the Photonic TTD system and the perfect phase shifter. ....	55
Figure 43.	Beam patterns at 1.275 GHz of the Photonic TTD system and the perfect phase shifter. ....	55
Figure 44.	Beam patterns at 1.3 GHz of the Photonic TTD system and the perfect phase shifter. ....	56
Figure 45.	Phase vs. frequency for a five element delay line of an ideal TTD system. ....	57
Figure 46.	Phase vs. frequency for a five element delay line of the Photonic TTD system. ....	57
Figure 47.	Magnitude vs. frequency for a five element delay line of the Photonic TTD system. ....	58
Figure 48.	Beam patterns at 1.25 GHz of the Photonic TTD system and the perfect phase shifter. ....	59
Figure 49.	Beam patterns at 1.275 GHz of the Photonic TTD system and the perfect phase shifter. ....	59
Figure 50.	Beam patterns at 1.3 GHz of the Photonic TTD system and the perfect phase shifter. ....	60
Figure 51.	Typical phase drift of a single channel vs. network analyzer reference signal. ....	62
Figure 52.	Inter channel phase drift. ....	63
Figure 53.	Phase vs. frequency for a single channel of the free space system. ....	64
Figure 54.	Phase vs. frequency for a single channel of the integrated system. ....	64

## List of Figures from Appendixes

Figure A-1.	Mechanical Drawing of Optical Breadboard Design.....	A-3
Figure A-2.	Front End.....	A-4
Figure A-3.	Schematic of Glass Spacers in Front End.....	A-5
Figure A-4.	TTD Replication and Collimating Optical Subsystem .....	A-7
Figure A-5.	TTD Selection and Feedback Subsystem .....	A-8
Figure A-6.	Continuous Phase Grating Compared with 2 and 4 Discrete Phase Levels.....	A-11
Figure A-7.	3 Dimensional View of Single Cycle of the Binary Optic.....	A-13
Figure A-8.	2 Dimensional View of a Single Cycle of the Binary Optic.....	A-14
Figure A-9.	Responsivity of ARX-GP Detector .....	A-19
Figure A-10.	Bias Circuit for ARX-GP Detector .....	A-19
Figure A-11.	MSS4X5 Matrix Shutter Mechanical Drawing .....	A-20

## List of Tables

Table 1.	Beam squint of the Photonic TTD system and the perfect phase shifter for the frequencies 1.25, 1.275, and 1.3 GHz at steer angles of 0, 30, and 60 degrees. ....	61
----------	--	----



## **List of Tables from Appendixes**

Table A1. Specifications of Front End Components .....	A-6
Table A-2 Specification of TTD Beam Replicating and Collimating Subsystem.....	A-7
Table A-3 Multi-Level Diffraction Efficiency for Various Numbers of Phase Levels .....	A-12
Table A-4 Specifications for BG30 Grin Rod.....	A-17

## **Acknowledgments**

The authors would like to thank Jeffrey Carlo, Reinhard Erdmann, David Gucza, Douglas Norton, and Paul Repak of Rome Laboratory and Kevin Baldwin and Dr. David Sumberg of the Rochester Institute of Technology for their technical contributions.

The authors would like to thank James Cusack, chief of the Rome Laboratory Photonics Division, for his support and guidance.

## **Preface**

The purpose of this final report is to document all work associated with Rome Laboratory (RL) Photonics Center effort 4600P210. The project 4600P210 encompasses the development, construction, testing, and evaluation of a breadboard for photonically controlling a 20 element, wide bandwidth (200 MHz) L-Band phased array radar. The concepts, theoretical development, and design of the photonic beamformer were completed under a separate, preceding effort (4600P204). For completeness, this report includes previously documented material outlining both the theoretical basis for, and the design of the photonic beam steerer. The work documented herein represents one of a number of concepts that Rome Laboratory is pursuing to generate true time delays for wide bandwidth radar and communication systems. The intention of this particular work was to combine in-house and contractual Expert in Science and Engineering(ESE) efforts with industry, through Collaborative Research and Development Agreements(CRDAs), to analyze practicality and viability of prototype photonic systems for the afore mentioned and other applications.

Dr. Henry Zmuda, of the University of Florida, and Captain Edward Toughlian of Rome Laboratory, with assistance from Dr. David Sumberg of the Rochester Institute of Technology, performed the theoretical, developmental and design tasks.

Mr. Paul Payson, Mr. John Malowicki and Mr. Herbert Klumpe, III, all of Rome Laboratory, performed construction, testing, and analysis of the photonic breadboard.

## List of Symbols, Abbreviations, and Acronyms

AF	Array Factor
AO	Acousto-Optic
BW	Bandwidth
CRDA	Cooperative Research and Development Agreement
DMD	Deformable Mirror Device
FFT	Fast Fourier Transform
GPIB	General Purpose Interface Bus
GRIN	Gradient Index Lens
HeNe	Helium Neon
IR	Infrared
MCE	Mirror Control Electronics
PZT	Piezo Electric Transducer
RF	Radio Frequency
TTD	True Time Delay
$\lambda$	Wavelength
$\tau$	Time delay

## 1.0 Introduction

The concept of the phased array antenna system is a powerful one. Single element antenna systems only offer a fixed radiation pattern and must be physically moved in order to steer the radiation. In contrast, the phased array system can both steer the beam and generate complex radiation patterns by means of appropriately phased signals applied to each of the antenna elements.

Two general approaches exist for generating properly phased signals. One is the phase shift method and the other the true time delay method [1]. The phasing required by the phase shift method is easily achieved with electronic phase shifters and is the approach currently employed in the majority of phased array systems. Although easily realized electronically, the phase shifters tend to be bulky and require significant power at the antenna back plane. An additional problem with the phase shift method of beamforming becomes apparent if multiple frequencies are transmitted simultaneously. The energy associated with the different frequencies will point in different directions in the antenna's far field causing an increase in beam width. This phenomena, called squint, restricts the phase shift approach to narrowband operation.

A true time delay system in its most general form is a set of variable delay lines—each providing a signal to a single antenna element. True time delay systems offer the advantage that they are not afflicted with beam squint; i.e., all radiating frequency components point in the same direction. This may be necessary, for example, to avoid unwanted detection of the transmission (security), to avoid receiving an unwanted signal (a jamming signal), or simply to accurately place radiated beam(s) for low observable detection and tracking. Attempts to implement a true time delay system in practical form have not yet been realized. Variable delay lines currently exist only in very crude forms such as mechanical line stretchers. Attempts to achieve variable delay line performance have focused mainly on constrained feed systems where different lengths of optical fiber or electrical cable can be switched in and out to vary the path length, and hence, achieve the proper delay. This approach requires the use of many switches to achieve good resolution beamforming, especially for large arrays. The large fan-out of these switched cable schemes results in the need for large amounts of power to operate the switches and significant signal losses through the many switches.

Photonics offers the potential, due to its inherent ability to spatially process information, to use an optical signal processing approach to realize a continuously variable RF delay line. This delay line, placed in parallel with other delay lines, provides the true time delay signals required for a phased array antenna system.

## 2.0 Background

### 2.1 Theory of Phased Array Beamforming

To gain a general understanding of the operation of a phased array system, we consider a linear array of equally spaced isotropic point sources and determine its radiation pattern or array factor ( $AF$ ) [2]. We start by only considering the far field radiation pattern. By doing so, the incoming rays from a point source in the far field can be approximated as traveling parallel to one another by the time they reach the antenna array. This approximation allows for the concise analytical expression of the  $AF$ . The approach taken to find an analytical expression for the  $AF$  is to first consider the receive mode of operation. From Figure 1 we find the  $AF$  in the receive mode by summing the far field excitation of all the elements:

$$AF = I_0 + I_1 e^{j\beta d \sin \theta} + I_2 e^{j\beta 2d \sin \theta} + \dots = \sum_{n=0}^{N-1} I_n e^{j\beta n d \sin \theta} \quad (1)$$

where  $N$  is the total number of elements in the array,  $n=0, 1, \dots, N-1$  is the element number,  $d$  is the element spacing,  $\beta$  is the propagation constant in free space,  $I_n$  is the received element current, and  $\theta$  is the observation, or measurement angle.

Since an antenna is a reciprocal device, we can immediately see how to steer a transmitted beam to a desired angle ( $\theta_0$ ), simply by forcing all the rays to travel the same path length to reach the desired location in the far field. The  $AF$  can be written:

$$AF = \sum_{n=0}^{N-1} I_n e^{j(\beta n d \sin \theta + \beta_L L_n)} \quad (2)$$

where  $L_n$  is the physical length of the line used to delay the signal at element  $n$ , and  $\beta_L$  is the propagation constant for the line. This is the same condition as requiring the relative phase between elements to be zero in the far field at the desired steer angle. Therefore, we find the incremental delay line length ( $L$ ) from:

$$0 = \beta n d \sin \theta_0 + \beta_L L_n. \quad (3)$$

Therefore:

$$L_n = -\frac{\beta}{\beta_L} nd \sin \theta_0. \quad (4)$$

Of course, more complicated radiation patterns can be achieved by applying other than a linear phase progression across the array.

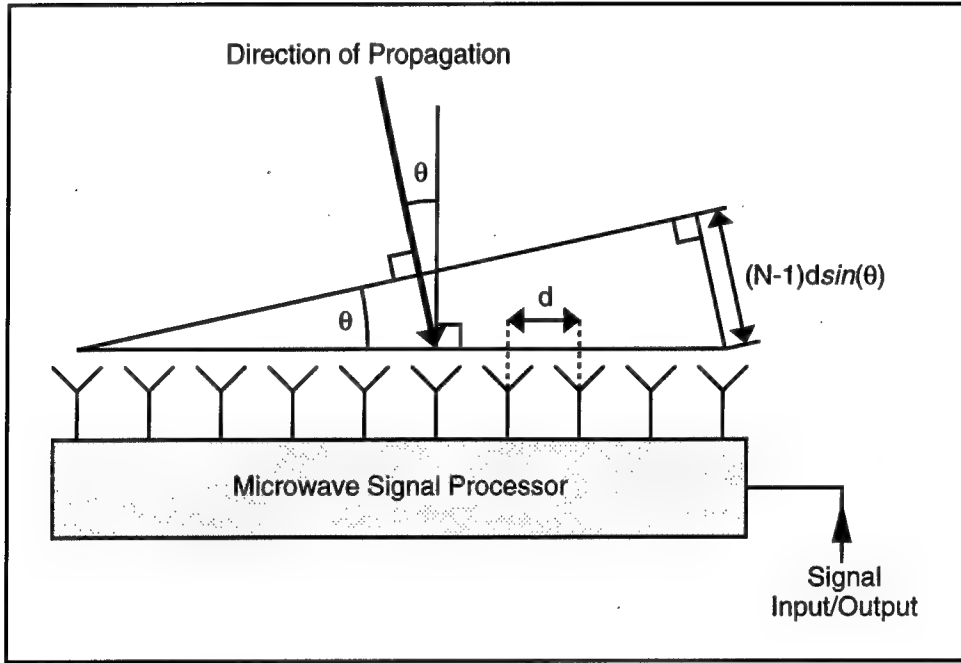


**Figure 1.** A steered phased array antenna.

We are now at a point where we can distinguish between phase shift and true time delay beam steering techniques. The differential phase ( $\Delta\phi$ ) between elements for a linear phase progression between elements can be written:

$$\Delta\phi(\omega) = \beta_L \Delta L = \omega T \quad (5)$$

where  $T = \frac{\Delta L}{v}$  is the time delay of the line,  $\Delta L = \frac{-\beta}{\beta_L} d \sin \theta_0$  is the differential line length between elements, and  $v$  is the signal velocity of propagation in the line. When all frequencies see the same time delay as is the case for the system described by Equation (5),



the system is said to be of the true time delay type. Also, from Equation (5), it should be noted that for the true time delay system, the phase is a linear function of frequency with a slope of  $T$ .

A beamformer implemented using only phase shift is accomplished by setting the differential phase equal to a constant, typically:

$$\Delta\phi = \omega_c T \quad (6)$$

where  $\omega_c$  is the center frequency of the band to be radiated. In other words, all frequency components receive the same phase shift. This results in the energy associated with the center frequency being radiated in the desired direction, but the energies of the other frequency components being radiated in other directions centered about the desired direction.

## 2.2 Beam Squint

Beam squint is a phenomena where the energy associated with the different frequencies points in different directions in the antenna's far field. For a wide bandwidth system this phenomena shows up as an increase in beam width. True time delay systems, like the one presented herein, generate properly phased signals theoretically eliminating beam squint, thus enabling wide bandwidth operation. In the following section the beam squint problem of a conventional phase shift radar system is described.

At the  $N^{th}$  element of a linear array the phase may be described as follows:

$$\Phi = \frac{2\pi Nd}{\lambda} \sin \theta \quad (7)$$

where  $\lambda$  is the wavelength of the design transmit frequency,  $d$  is the element spacing (for our system  $\lambda/2$ ) and  $\theta$  is the angle of the wave front as measured from the plane of the linear array.

Rewriting the equation gives:

$$\sin \theta = \frac{\Phi \lambda}{2\pi Nd} \quad (8)$$

For an incremental change in frequency the equation becomes:

$$\frac{\partial}{\partial \lambda} \sin \theta = \frac{\partial}{\partial \lambda} \frac{\Phi \lambda}{2\pi N d} \quad (9)$$

or

$$\cos \theta \frac{\partial \theta}{\partial \lambda} = \frac{\Phi}{2\pi N d} \quad (10)$$

Solving for  $\partial \theta$  and substituting using Equation (8) gives:

$$\partial \theta = \frac{\partial \lambda}{\lambda} \tan \theta. \quad (11)$$

Therefore:

$$\partial \theta = \frac{\partial f}{f} \tan \theta \quad (12)$$

or the beam squint ( $\Delta \theta$ ) is given by:

$$\Delta \theta = -\frac{\Delta f}{f} \tan \theta. \quad (13)$$

The negative sign is added to indicate that as frequency increases the scan angle decreases.

The relationship described in Equation (13) has some interesting ramifications. The aperture size and the beam width have no influence on the beam squint. Perhaps most significantly, the frequency sensitivity depends on the boresight angle  $\theta$ . As the steer angle increases (gets further away from broad side) beam squint increases[3].

### **3.0 Photonic Processing for Phased Array Applications**

The purpose of this section is to present two optical signal processing systems which can be used to realize the properly phased signals at the back plane of a phased array antenna system. The first system to be presented is a phase shift system while the second is a true delay system. A detailed discussion of the theory, configuration, and operation, as well as some experimental results, will be presented.

#### **3.1 Photonic Processing Fundamentals**

In this subsection, two concepts are introduced which are fundamental to understanding the operation of the photonic processors to be presented. The first concept to be discussed is single sideband, suppressed carrier modulation via Bragg (acousto-optic (AO)) cell interaction. Additionally, we'll discuss how the AO cell can provide the time delay for variable delay line purposes. The second concept relates to using the single sideband, suppressed carrier modulated signal in an optical heterodyne configuration. We'll see that the optical heterodyne configuration not only provides a very efficient way of realizing an RF phase shift, but also is fundamental towards realizing variable time delay by allowing a local oscillator signal to selectively point inside the delay line AO cell.

**3.1.1 Operation of an AO Cell:** The systems to be introduced in later sections have as one of their key components an AO cell. Therefore we start with a review of its operation [4]. Referring to Figures 2a & 2b, the RF is applied to the Bragg cell via a transducer which generates acoustic waves within the crystal of the cell. If the orientation of the traveling acoustic waves within the cell relative to the incoming light is at an angle such that interaction between a phonon and photon is of high probability, the Bragg cell is said to be oriented at the Bragg angle ( $\theta_B$ ).

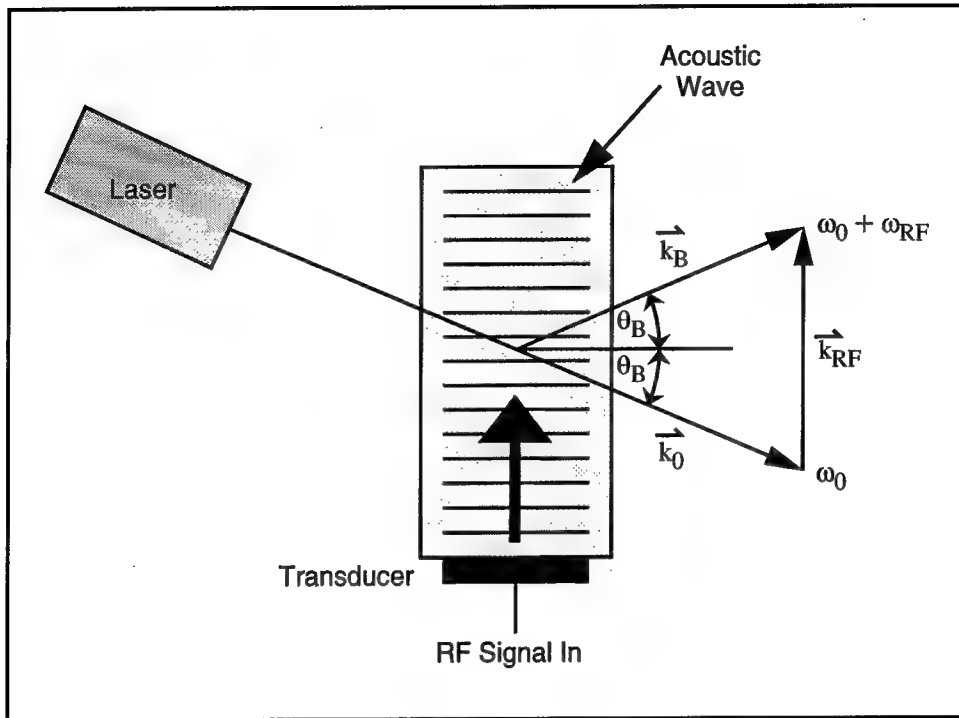


**Figure 2a.** Acousto-optic cell theory of operation configuration for frequency up shift.

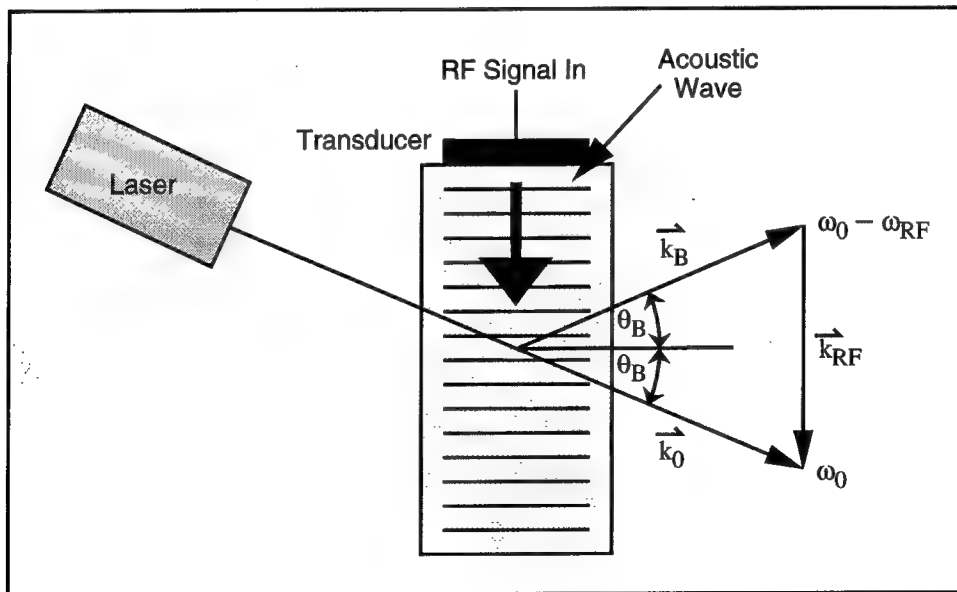


**Figure 2b.** Acousto-optic cell theory of operation configuration for frequency down shift.

This effect can be explained and quantified from a conservation of momentum argument. The vector sum of the propagation vectors for the interacting particles of light ( $\vec{k}_0 h / 2\pi$ ) and sound ( $\vec{k}_{RF} h / 2\pi$ ) (where  $h$  is Planck's constant, and  $\vec{k}$  represents the particles' propagation vector) allows us to find the Bragg angle from:

$$\sin(\theta_B) = \frac{|\vec{k}_{RF}|}{2|\vec{k}_0|} = \frac{\lambda_o}{2\Lambda} = \frac{\lambda_o f_{RF}}{2v} \quad (14)$$

where  $\lambda_o$  is the wavelength of light,  $\Lambda$  is the acoustic wavelength,  $v$  is the velocity of the sound wave in the crystal, and  $f_{RF}$  is the RF frequencies of the input signals to the transducer. The light coming out at the various angles is not only directed at an angle as a function of the RF frequency, but it is also up or down Doppler shifted by the corresponding frequency. This can be seen if a similar argument involving energy conservation is invoked:

$$\frac{h}{2\pi} \omega_B = \frac{h}{2\pi} \omega_0 \pm \frac{h}{2\pi} \omega_{RF}$$

$$\therefore \omega_B = \omega_0 \pm \omega_{RF} \quad (15)$$

The result is that the optical carrier signal up shifted or downshifted by the RF frequency component. Additionally, the AO cell (due to its low velocity of acoustic wave propagation) can provide a significant amount of signal delay. This will be discussed later.

**3.1.2 The Optical Heterodyne Process:** In order to recover the RF signal from light that has been frequency shifted by an AO cell, as just discussed, an optical heterodyne process is employed to beat the signal back down by stripping off the optical carrier [5]. This is understood by referring to Figure 3 where the output of a laser source is split into two paths. One path is frequency shifted, by an AO cell for example, to result in an output which is  $A_1 \cos[(\omega_o + \omega_{RF})t]$ . If the other leg of the heterodyne system is phase shifted by  $\Phi$ , then the output of that leg of the heterodyne system will be  $A_2 \cos[\omega_o t + \Phi]$ , where  $\Phi$  is an optical phase shift. These two signals are then summed in a photodetector which takes the time average of the incident intensity.

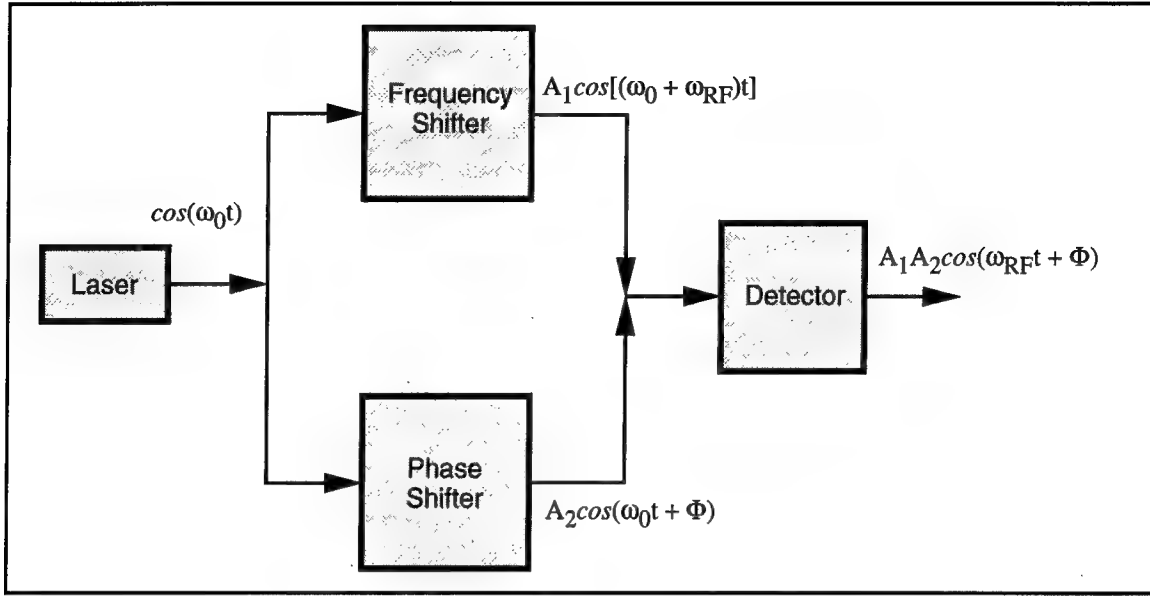


**Figure 3.** Optical heterodyne system.

Mathematically the result is found first by rewriting the sum of the two signals ( $E$ ):

$$E = A_1 \cos[(\omega_0 + \omega_{RF})t] + A_2 \cos[\omega_0 t + \Phi]$$

$$E = \cos(\omega_0 t) \cdot [A_1 \cos(\omega_{RF} t) + A_2 \cos(\Phi)] - \sin(\omega_0 t) \cdot [A_1 \sin(\omega_{RF} t) + A_2 \sin(\Phi)]. \quad (16)$$

We next take the square of  $E$  and rearrange to find:

$$E^2 = \cos^2(\omega_0 t) \cdot [A_1 \cos(\omega_{RF} t) + A_2 \cos(\Phi)]^2 + \sin^2(\omega_0 t) \cdot [A_1 \sin(\omega_{RF} t) + A_2 \sin(\Phi)]^2 - 2 \cos(\omega_0 t) \cdot \sin(\omega_0 t) \cdot [A_1 \cos(\omega_{RF} t) + A_2 \cos(\Phi)] \cdot [A_1 \sin(\omega_{RF} t) + A_2 \sin(\Phi)] \quad (17)$$

and finally time average over a time much greater than an optical period ( $T_0$ ):

$$\begin{aligned} \overline{E^2} &= \frac{1}{T_0} \int_t^{t+T_0} E^2 dT = \frac{A_1^2 + A_2^2}{2} + A_1 A_2 [\cos(\omega_{RF} t) \cos(\Phi) + \sin(\omega_{RF} t) \sin(\Phi)] \\ \overline{E^2} &= \frac{A_1^2 + A_2^2}{2} + A_1 A_2 \cos(\omega_{RF} t - \Phi). \end{aligned} \quad (18)$$

The first term in the above result is a DC term. It is the second term that is of particular interest for this application, namely that we retrieve the RF signal at the detector output. We also preserve the phase shift applied to our optical signal, i.e. the amount of RF phase shift

numerically equals the amount of optical phase shift. Depending on the application, the phase shift capability can be very significant. It provides a simple way of achieving an RF phase shift capability from an optical phase shift. The importance of this result can be seen if we go back to the previous figure and consider how the phase shift is achieved. One way to realize an optical phase shift is to vary the path length. Since we are dealing with optical signals with wavelengths on the order of 500~1500nm, one wave (or  $2\pi$  radians) of phase shift would require a path length modification of less than 2  $\mu\text{m}$ . In other words, by mixing the two light beams in this way provides a means of obtaining substantial variable RF phase shift, achievable with optical components using phase shifts arising from optical path differences on the order of optical wavelengths.

### 3.2 Photonic Approach to Phased Array Beamforming for Narrowband Applications

If we reconsider the concepts presented in the previous sections and utilize the idea of spatial integration of bulk optical components, we can realize a high packing density phase shift beamforming system for phased array applications [6]. The approach can be understood by referring to Figure 4. The optical carrier output from the laser is sent to a beamsplitter cube where one of the two output beams acts as the local oscillator reference while the other is to be frequency shifted by the RF, as discussed in the optical heterodyne section.

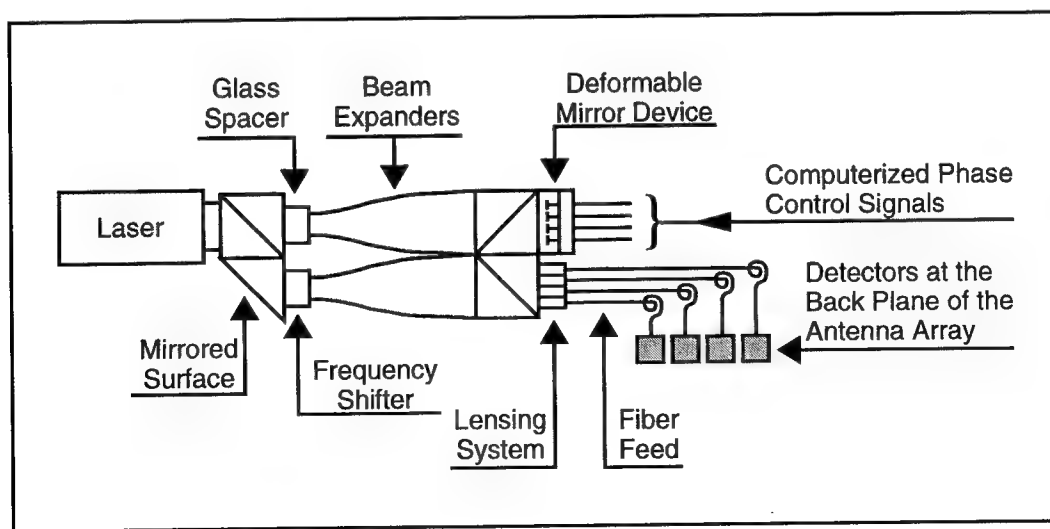


**Figure 4.** Integrated narrow band high packing density phased array beamforming system.

If the two beams are then expanded and collimated, and the phase of the local oscillator beam is tailored in a controllable fashion across the wavefront, a detector array can be used to directly obtain the RF signal required for the antenna drive. Such phase control of an optical wavefront can be achieved using a deformable mirror device (DMD). This device, to be more fully discussed and detailed in later sections, can be envisioned as a computer driven NxM array of mirrors each capable of moving independently in a piston-like fashion. The excursion is typically on the order of a few optical wavelengths which is more than sufficient to produce the required RF phase shifts. Because high-speed, high-packing density detector arrays are difficult to realize, a graded index (GRIN<sup>1</sup>) lens array pig-tailed with fiber is used to carry the signal to the

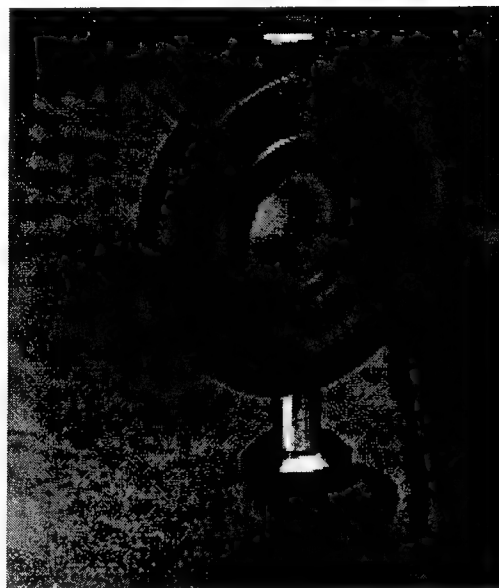


**Figure 5.** Binary optic.

detector elements. Additionally, the use of fiber to carry the properly phased signals to the antenna eliminates the need to use heavy, bulky, lossy waveguide to realize the RF signal at the back plane of the antenna.

---

<sup>1</sup>The GRIN or graded index lens is a substrate usually in cylindrical form which efficiently guides light. The substrate is doped such that the index of refraction component perpendicular to the direction of propagation of light is graded, typically with a parabolic distribution to mimic the operation of a lens. The cylinder is cut to length, typically to focus or image the incoming beam.



Alternatively, a more efficient use of the light can be achieved by spatially splitting the reference and signal beams into  $N$  equal-intensity beams. This can be accomplished by using a diffractive device sometimes referred to as a binary optic [7]. A 25 element device, which is described qualitatively in the Appendix, is pictured in Figure 5.

### 3.3 Photonic Approach to Phased Array Beamforming for Broadband Applications

In this section an optical signal processing system which provides broadband, continuously variable time delay will be presented [8]. A theoretical and analytical representation of its operation and performance will be reviewed. Additionally, a spatially integrated version of this system will be presented.

The operation of the delay line can be explained with reference to Figure 6. By utilizing an acousto-optic cell as the frequency shifter in a heterodyne configuration, a continuously variable time delay is achieved. The laser output is split into a plane wave local oscillator (upper path) which simply acts as a reference, and a beam which is sent to an acousto-optic (AO) cell frequency shifter. As discussed earlier, the acousto-optic cell operates by applying the RF signal input to a piezoelectric transducer mounted on a substrate which efficiently propagates an acoustic wave in the  $x$  direction as shown. The physical length of the cell divided by the velocity of the acoustic wave,  $v_s$ , provides a significant time delay  $\tau$  across the length of the cell, or  $\tau = x(t) / v_s$ . Using the lensing system shown in the figure, each point along the path of the  $x$  axis in the AO cell generates a plane wave which is incident on a tiltable mirror. The angle of this plane wave uniquely corresponds to a spatial coordinate  $x(t)$  along the axis of propagation of sound in the cell.

It is now to be proven that two plane waves, one frequency shifted relative to the other, can only beat efficiently when they are of the same angle (spatial frequency). For optical frequency,  $f_0$ , the plane wave which represents the signal beam can be expressed as:

$$a_s(t) = A_1 \cdot e^{j(2\pi f_s t + 2\pi \alpha x + \phi_0)} \cdot e^{j2\pi f_o t} \quad (19)$$

where  $\alpha$  represents the spatial frequency or tilt of the wave measured with respect to the plane wave reference beam given by:

$$a_{LO}(t) = A_{LO} \cdot e^{j2\pi f_o t} \quad (20)$$

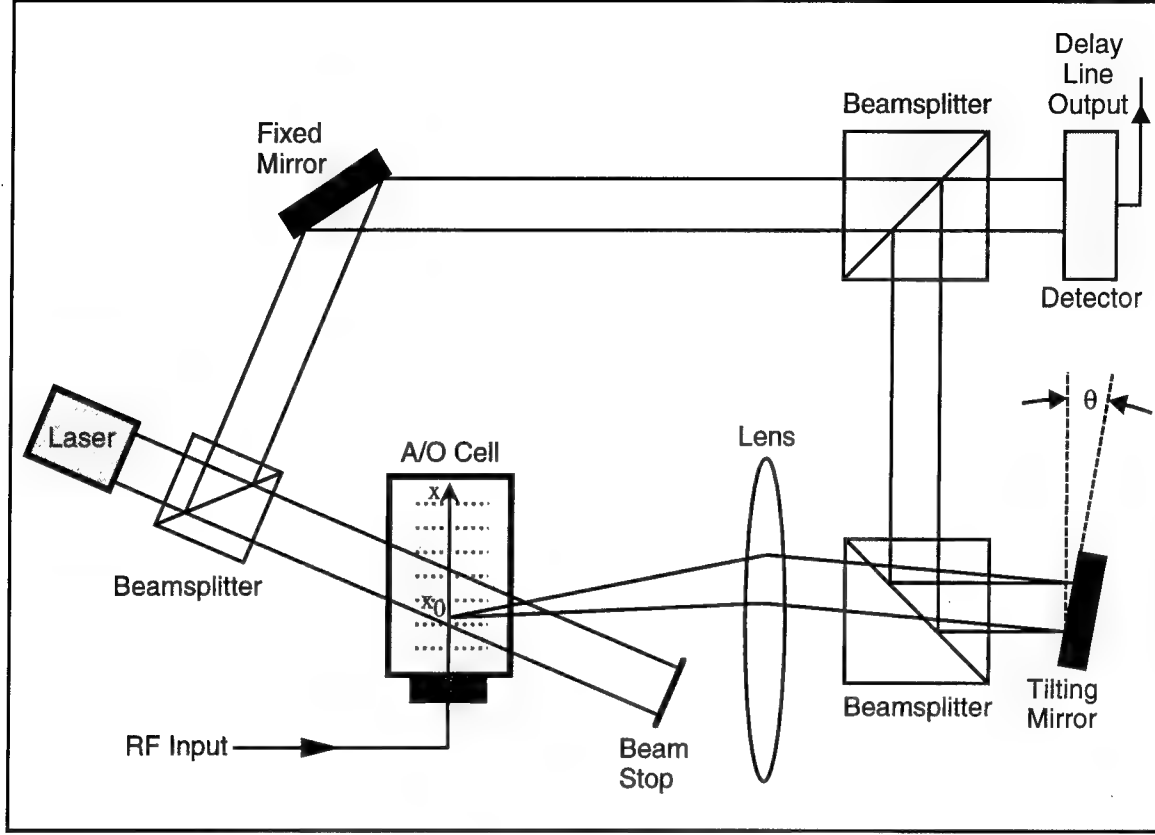


**Figure 6.** Delay line theory.

Note that the reference phase of the local oscillator beam is arbitrarily taken to be zero. The photodetector integrates the intensity over all space of the summed signal and reference plane waves producing the electrical signal  $i(t)$  proportional to the time-averaged intensity:

$$i(t) = \frac{1}{2} \int_{-\infty}^{\infty} \left| A_{LO} + A_s e^{j(2\pi f_s t + 2\pi \alpha x + \phi_o)} \right|^2 dx. \quad (21)$$

Using an identity from Fourier analysis, the impulse or delta function  $\delta(\alpha)$  can be expressed as [9]:

$$\delta(\alpha) = \int_{-\infty}^{\infty} e^{j2\pi \alpha x} dx. \quad (22)$$

The integral of Equation (21) is readily evaluated. Neglecting the DC terms we find that:

$$i(t) = A_{LO} A_s \cdot \cos[2\pi f_s t + \phi_o] \cdot \delta(\alpha). \quad (23)$$

Clearly then by tilting the mirror (i.e. by choosing  $\alpha$ ), we select which plane wave will beat with the local oscillator in the detector—recalling that each plane wave represents a different point of time (delay) on the signal. Of course in a non-ideal system—plane waves are not realizable, and therefore diffraction limiting effects give the system finite resolution.

For the simplified system of Figure 6, a straightforward geometrical (ray) optical analysis shows that the time delay realized as a function of the lens focal length  $F$  mirror tilt angle  $\theta$  and acoustic velocity,  $v_s$ , is  $T = \tan(2\theta)F / v_s$ . Of course, in a fully engineered system, the simplified optical system typically becomes more sophisticated due to design requirements. A system similar to the one discussed was constructed on an optical bench. The experimental results can be found in the references [10]. Delay on the order of 50  $\mu$ secs is achievable with commercially available AO cells. This is equivalent to several tens of thousands of feet of delay in cable.

A comment on carrier frequency and system bandwidth is appropriate. The single laser approach presented here limits the system bandwidth including the carrier to several gigahertz. Carrier frequencies into the millimeter wave frequency range and beyond can be obtained utilizing a variety of approaches to phase lock two lasers operating at slightly different colors (wavelengths) [11,12]. The AO cell is placed in the path of one of these laser beams to provide RF modulation.

It is to be emphasized that the delay achieved is continuously variable. This, and the ability to integrate many such delay lines in an efficient manner, provides a unique capability which can be applied to traditional microwave systems. A discussion follows in the next section.

**3.3.1 A Spatially Integrated Approach:** A compact system incorporating the multiple delay lines in the spatially integrated optical implementation is now presented. Such an arrangement provides mechanical stability, reduces the drift problems encountered in free space optical systems as well as provides the ability to achieve higher packing densities. The basis of this integrated optical implementation is a class of spatial light modulator known as a deformable mirror device (DMD). A DMD is a pixelated mirror structure where each element (pixel) can be moved in tip, tilt, and piston. Various types of DMDs exist, each with distinct characteristics. For instance, the mirror elements might be controlled using an electrostatic or electrostrictive effect. One such electrostatic device is a 128 by 128

element array in a one square centimeter area [13,14]. The elements of this type of device can be independently moved in a piston-like fashion or rotation; but not both. A commercial electrostrictive device uses PZT material with three electrodes attached at each element to achieve tip, tilt, and piston movement at the element [15]. The element size for these devices is typically about 7mm on a side. This device is shown in Figure 7.

Figure 8 shows one possibility for a 20 element spatially integrated optical implementation. The output of the laser is split into its two polarizations by a polarizing beamsplitter cube.

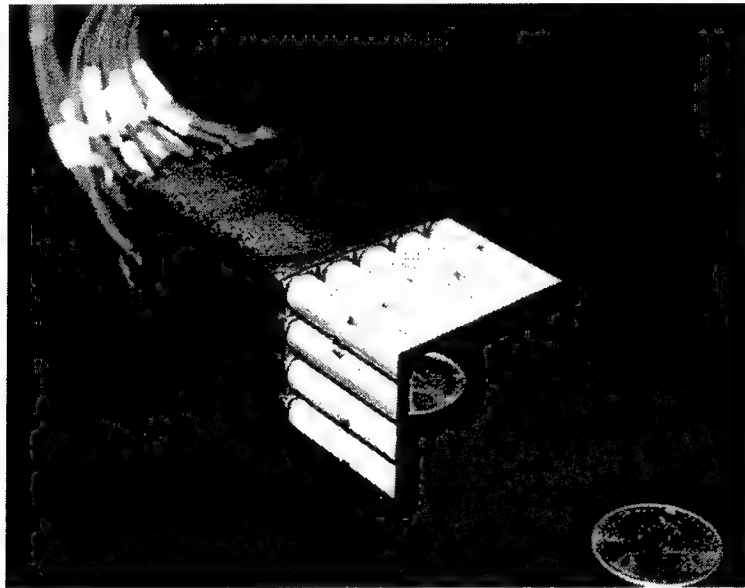


**Figure 7.** Electrostrictive 20 element deformable mirror device.

One polarization is frequency shifted by the Bragg cell which also spatially disperses the frequency components. The two polarizations are then recombined in order to make use of some common optics for beam replication. The next step is to image all frequency components onto each deformable mirror element such that the energy is equally distributed between the mirror elements. The unshifted beam must also be distributed such that an equal portion of it appears at each detector. The binary optic introduced earlier in Figure 5 provides a very efficient way of replicating the beams into 25 approximately equal intensity beams of which 20 are used (note that this technology can be extended to realize thousands of beams) [7]. The two polarizations are then later separated via a third polarizing

beamsplitting cube where the frequency shifted signal is imaged onto the DMD. Here each DMD element is tipped and/or translated to provide the correct delay and phasing.

On each pass to and from the DMD, the frequency shifted signal traverses a quarter wave-plate. The purpose of the double pass through the quarter-wave plate is to provide a 90 degree rotation of the electric field polarization in order to steer the signal via the same beamsplitting cube into the lens array. To see how this is accomplished we consider the operation of a quarter wave plate. A quarter-wave plate is a crystal which is oriented such that it provides a quarter wave of additional effective path length to one polarization of an incoming beam for a specified wavelength, i.e. it is a birefringent device.

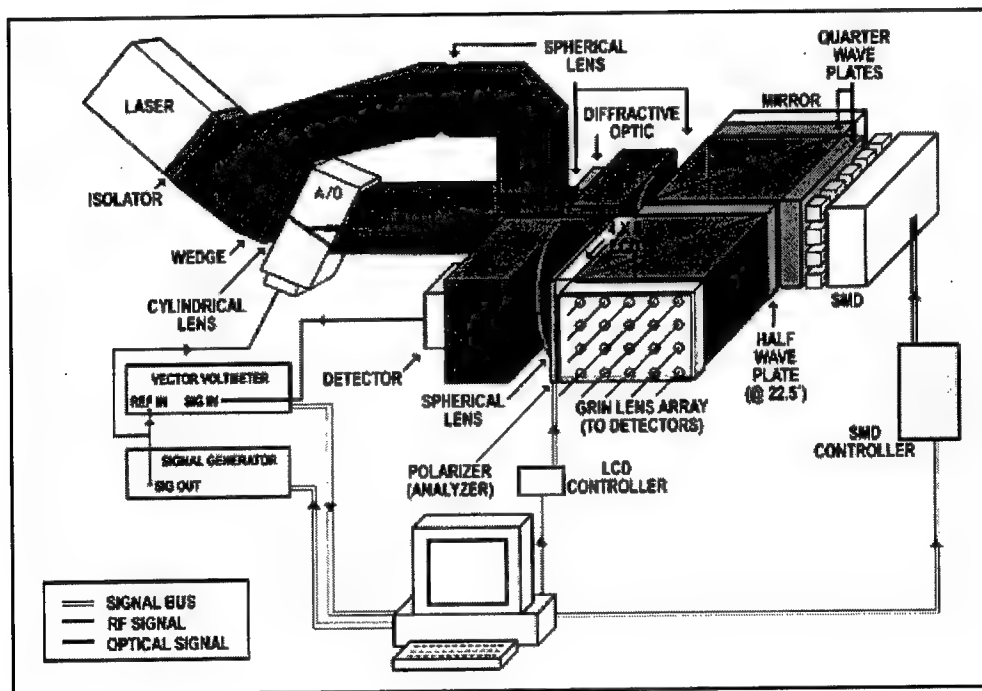


**Figure 8.** Integrated 20 element delay line system.

With one polarization advanced (or delayed by 90 degrees) relative to the other, the output is seen to be circularly polarized if the magnitudes of the two polarizations are equal, otherwise it is elliptically polarized. The effect of bouncing off the mirror element changes the handedness of the circularly (elliptically) polarized beam where the second pass through the quarter-wave plate returns the beam to linear polarization with the result of being 90

degree rotated relative its input orientation. The unshifted beam undergoes a similar operation but instead of being imaged onto the DMD, it is reflected off a flat mirror during which it also makes a double pass through a quarter-wave plate.

A polarizer is required before coupling the signals into the fiber. Since the two polarizations are orthogonal to each other they will not interfere (or more correctly, heterodyne). An additional polarizing beam splitter cube is used. The cube sends half the energy of the frequency shifted and local oscillator signals at a common polarization to a GRIN lens array. The output of the GRIN lens array is detected and contains the properly delayed RF signals. The twenty beams at the other output are summed by a lens which focuses the beams onto a single detector. Using a twenty element array of shutters prior to the summing lens, each delay may be individually monitored to provide closed loop delay control.

**3.3.2 Other Considerations:** Although DMDs provide a clean and efficient method of obtaining a frequency dependent phase shift, they do not preclude the possibility of obtaining the same results in other ways. For example, an electro-optic beam deflector can be used to obtain a linear spatial index variation, and consequently, provide the differential path (electrical) lengths needed [16]. The device is illustrated in Figure 9. The operation of the liquid crystal devices is fairly straight forward.

By applying a voltage to a resistive layer attached to the back of a given liquid crystal pixel, a linear voltage drop is experienced across the pixel. This linear voltage drop gives rise to a linear electric field across the pixel with a corresponding linear refractive index change as a result. Therefore, for an input plane wave incident on the pixel, the linear refractive index change will cause the plane wave to be tilted relative to the input angle. By changing the voltage across the pixel, the steer angle of the optical beam can be changed. The advantages of this approach are numerous including lower voltage requirements (typically 3~5 volts), much lower hysteresis and therefore increased controllability, but most importantly the ability to integrate the function of beamsteering into a monolithic system is possible since there are no moving elements (mirrors) with this approach.

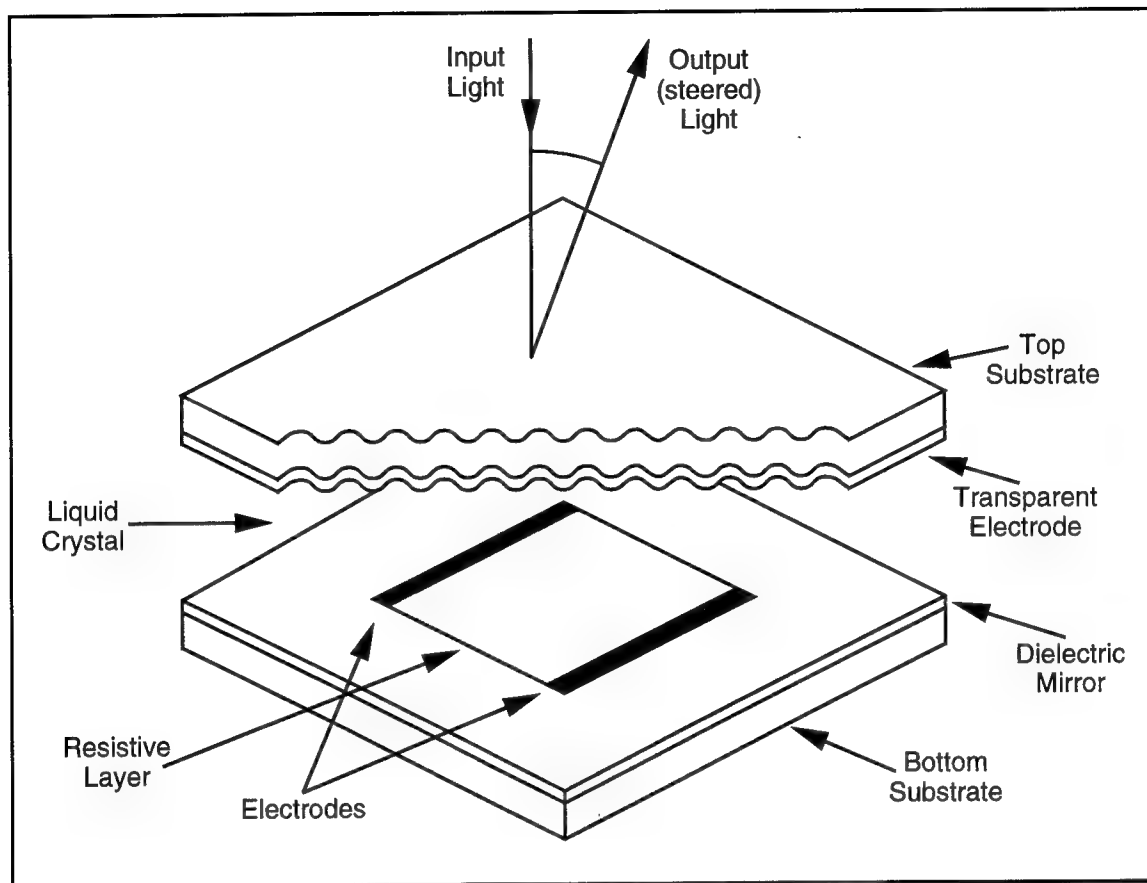


**Figure 9.** One pixel of a liquid crystal beamsteering device.

**3.3.3 Feature Resolution:** This section provides the theoretical basis and calculates the expected performance for resolving time delay. An experiment performed under project 4600P204 demonstrated the ability of a photonic delay line to resolve delay. The basic structure of the experimental setup is very similar to Figure 6. Some of the key components, (which are described in greater detail in Appendix A), include a Lightwave Electronics diode-pumped Nd-Yag laser at 1.3  $\mu\text{m}$ , a Brimrose AO cell that has 200 MHz passband centered at 1.3 GHz, and an Antel photodiode. The optical system pictured in Figure 10 was used for this experiment.

Two parts to this experiment were attempted—the impulse response and the system transfer function (amplitude only). The transfer function was generated in order to determine the 3 dB system bandwidth. The experimental configuration is shown in Figure 11. The RF signal generator was swept from 1.2 to 1.4 GHz and the transfer function was measured on a Tektronix spectrum analyzer. The transfer function is plotted in Figure 12. The

transfer function reveals that, in a 3 dB sense at least, the system does not adequately support the 200 MHz bandwidth of the AO cell. This is believed to be due to a non-optimal lensing system. The lensing system used did not adequately collect the spatially dispersed frequency shifted signals (as discussed earlier). This is easily remedied by a more sophisticated lensing system. For our purposes here, we were able to get a respectable result for the impulse response using off-the-shelf components.

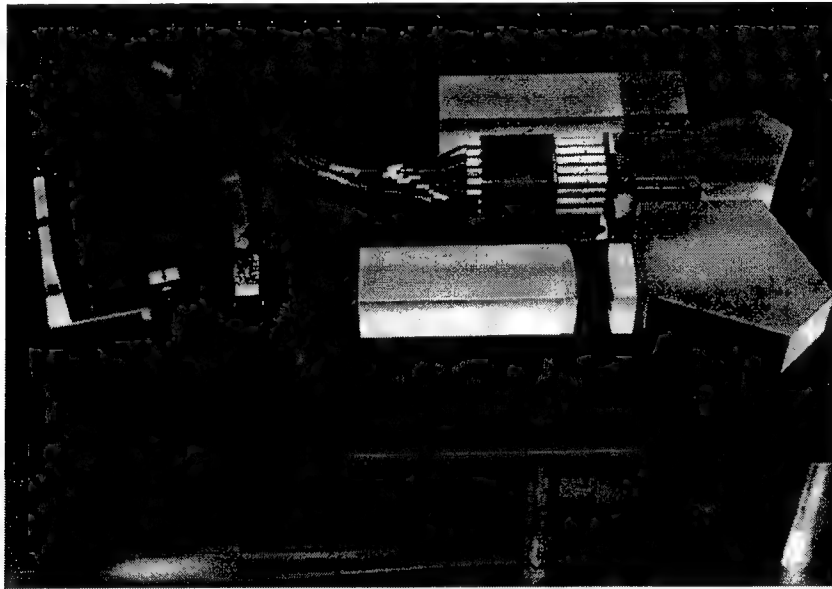


**Figure 10.** Integrated L-band photonic delay line system.

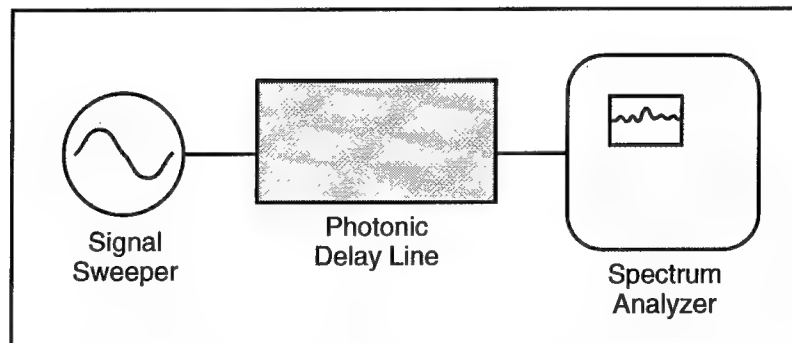


**Figure 11.** Feature resolution system to observe system amplitude transfer function.

Before the impulse response is presented, a few words are necessary to understand what results we should expect. To determine the resolution we should expect from the optical



delay line system requires that we determine the diffraction limited spot size of the optical system. As implied earlier, an alternate way of thinking about the operation of the optical delay line system is to imagine the local oscillator beam being imaged back through the system to the AO cell.

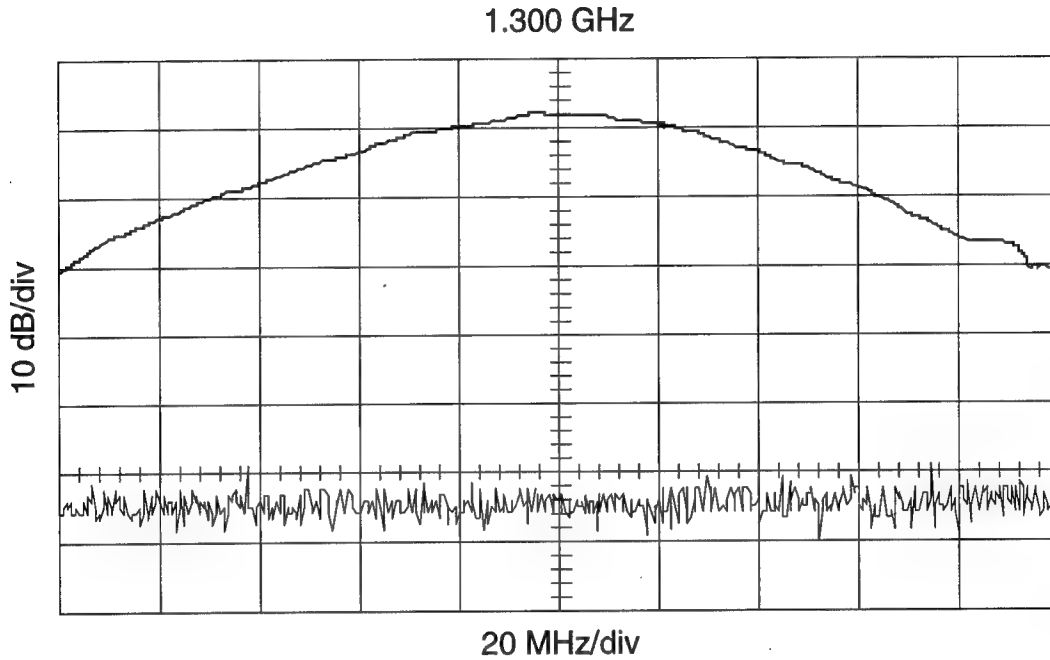


**Figure 12.** Photonic delay line amplitude transfer function.

The best resolution one could achieve would be due to the diffraction limited spot size of the local oscillator beam image in the AO cell. The Spot size ( $d$ ) for a Gaussian beam of diameter( $D$ ), referring to Figure 13 is given by [17]:

$$d = \frac{4\lambda F}{\pi D} \quad (24)$$

where  $\lambda$  is the optical wavelength and  $F$  is the effective focal length of the lens system. For the system used for this experiment, the local oscillator had a diameter of 2.4 mm, effective focal length of 36 mm, and optical wavelength  $\lambda = 1.3 \mu\text{m}$ . Therefore, the spot size is found to be  $d = 4(1.3 \mu\text{m})(36 \text{ mm})/(\pi \cdot 2.4 \text{ mm}) = 24.8 \mu\text{m}$ . The AO cell had a velocity of propagation  $v = 5120 \text{ m/s}$ . Therefore, the smallest pulse that could be resolved by this system would have a duration of  $\tau = d/v = 4.8 \text{ nsec}$ .

This corresponds to a support bandwidth of  $BW = 1/\tau = 206.5 \text{ MHz}$ . This is on the order of the passband of the AO cell. Since the bandwidth supported is on the order of that of the AO cell, the finite size (diameter) of the local oscillator (pointer beam) has negligible effect on the output signal.

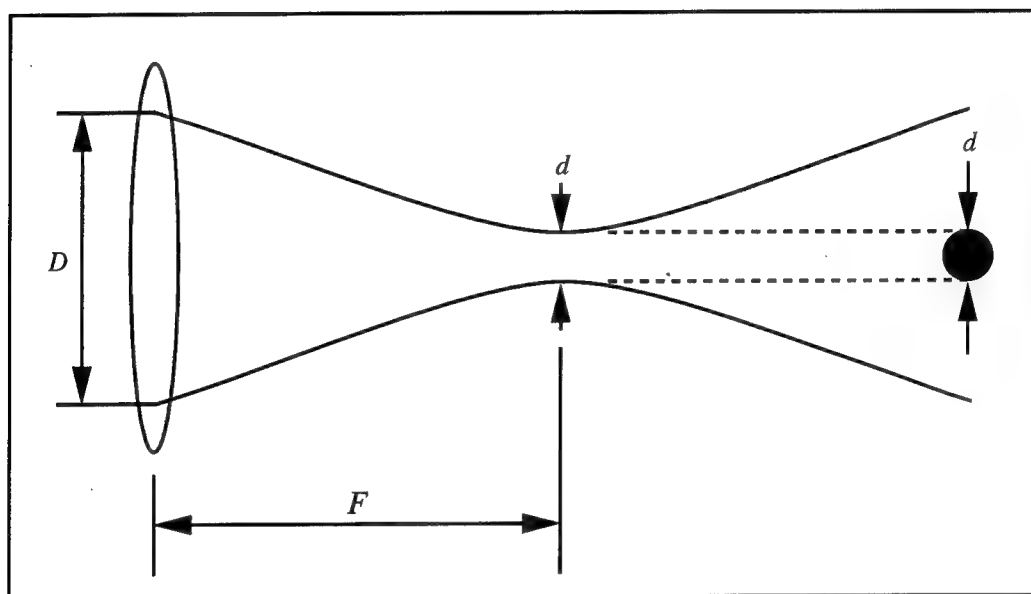


**Figure 13.** Simple optical system demonstrating the focused spot size ( $d$ ) for an input beam of diameter ( $D$ ).

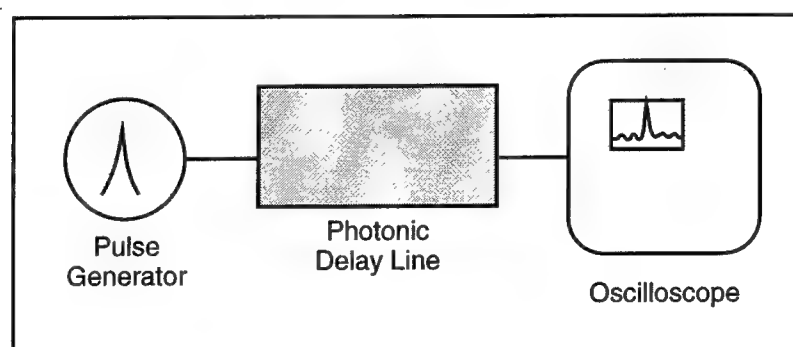


**Figure 14.** Feature resolution system to observe system impulse response.

The system to measure the impulse response is shown in Figure 14. The input pulse was viewed on an oscilloscope and is plotted in Figure 15. As seen by the vertical cursors in the figure, the input pulse had a 3 dB pulse width of 385 ps and a corresponding bandwidth of

$BW = 1 / \tau \cong 2.6GHz$ . This is more than sufficient bandwidth to support the AO cell. The system impulse response is shown in Figure 16. The impulse pulse response 3 dB width was measured to be  $\tau = 4 nsec$ . The implied spatial resolution for the target ranging and imaging applications is about 4 feet for this type of cell. It is easily seen that a cell with greater bandwidth will provide even better spatial resolution.

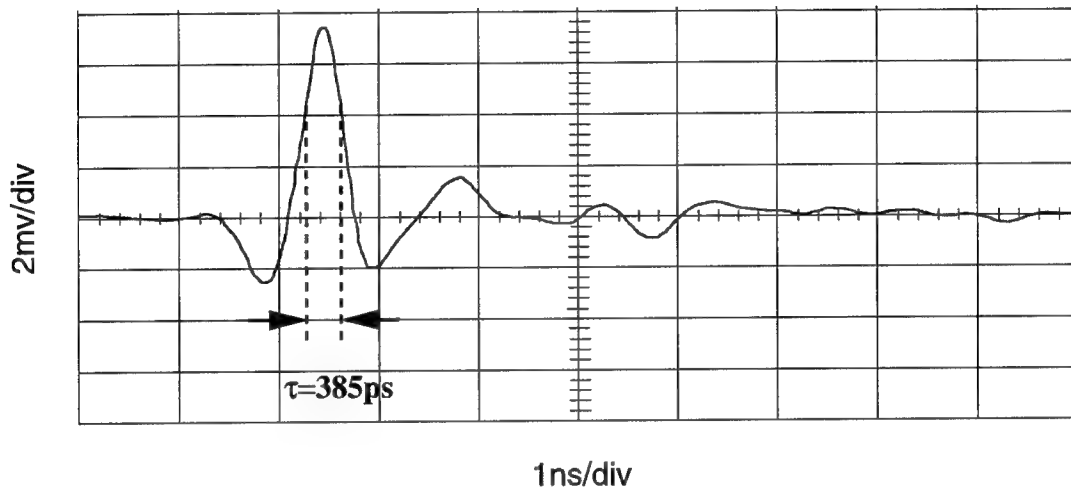


**Figure 15.** Input signal to photonic delay line for impulse response generation.

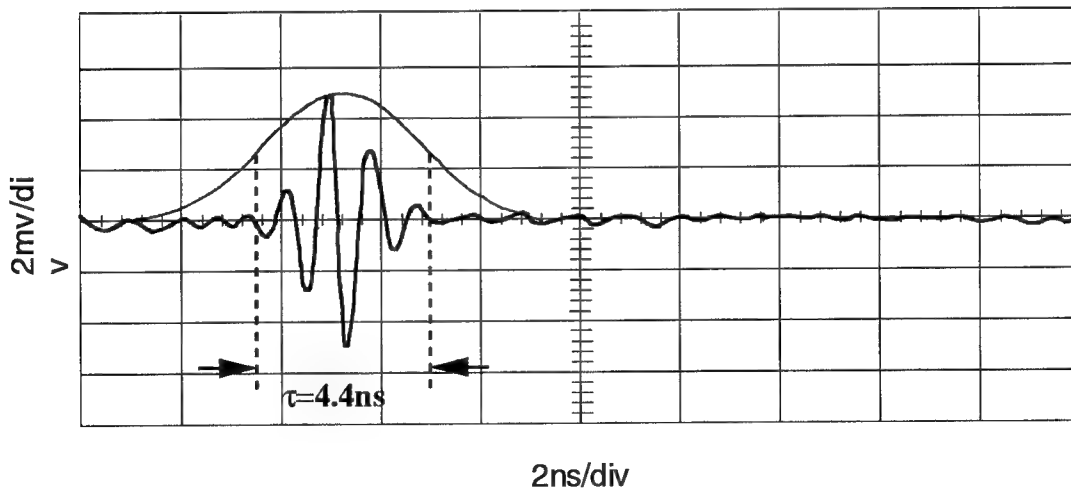


**Figure 16.** Impulse response of photonic delay line.

**3.3.4 Delay Resolution:** In the following section the delay resolution of the photonic beamformer is calculated. The resolution of the DMD element combined with the

magnification effects of the lensing system and the velocity of propagation in the AO cell affect the delay resolution. The delay resolution determines how finely the beam can be stepped across angle space. The maximum available delay is also calculated. The maximum delay establishes the upper limit of the antenna size which can be supported.

To calculate system delay resolution, First the angular resolution of the DMD ( $\Delta\phi$ ) (refer to Figure 17) is found:

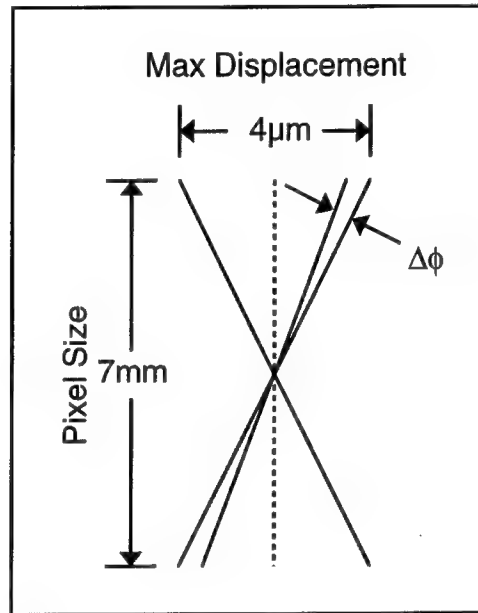


**Figure 17.** DMD pixel tilt.

$$\tan(\Delta\phi) = \frac{\frac{Max\_Displacement}{\frac{Number\_of\_Resolveable\_Displacements}{2}}}{\frac{Pixel\_Size}{2}} = \frac{\frac{4 \times 10^{-6}}{\frac{1024}{2}}}{\frac{7 \times 10^{-3}}{2}}. \quad (25)$$

Note that the number of resolveable displacements (1024) equals  $2^8$ , or the resolution of the applied 8-bit digital control signal.

Solving for  $\Delta\phi$  gives:

$$\Delta\phi = 1.116 \times 10^{-6} \text{ radians} \quad (26)$$

Next the spatial resolution [displacement ( $\Delta x$ )] inside the AO cell due to a ( $\Delta\phi$ ) displacement of the mirror element (see Figure 18) is calculated:

$$\Delta x = F \tan(2\Delta\phi) = 36 \times 10^{-3} \tan(2 \times (1.116 \times 10^{-6})) = 80.36 \text{ nm} \quad (27)$$

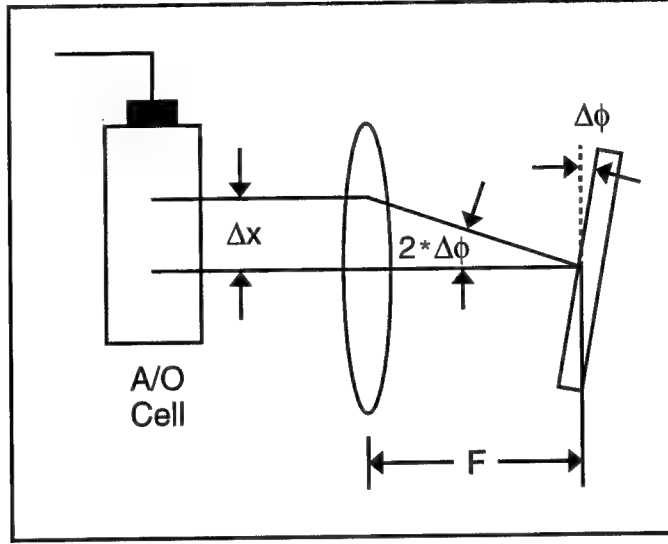


**Figure 18.** Displacement of beam inside the AO cell ( $\Delta x$ ) due to tilt of the mirror element ( $\Delta\phi$ ). Where  $F$  is the system effective focal length (approximately 36mm).

Finally, the delay resolution ( $\Delta t$ ) is found by converting the above spatial displacement ( $\Delta x$ ) to a temporal displacement:

$$\Delta t = \frac{\Delta x}{v} = \frac{80.36 \times 10^{-9}}{5120} = 15.69 \text{ psec} \quad (28)$$

where  $v = 5120 \text{ m/s}$  is the velocity of acoustic propagation in the AO cell.

The total distance across the 20 element phased array antenna is approximately 3 feet. To achieve a beam steer to endfire ( $90^\circ$ ) would require a delay of approximately 3 nsec.

Therefore the result given in Eq. (28) above indicates that approximately  $(3 \text{ nsec}) / (15.69 \text{ psec}) = 191$  different steer angles (in each direction ( $\pm 90^\circ$ )) or about 380 steer angles total might be possible.

The maximum delay realizable for this system, with this DMD, is  $\Delta t * 1024 \approx 16 \text{ nsec}$ . This delay is more than sufficient to support our 20 element antenna and in fact should support a 20 ft antenna at  $\pm 60^\circ$  steer angles.

## 4.0 System Description

In this section, a description of the overall physical system is presented. The overall system consists of three major subsystems—the electronics (test equipment), the optical system, and the computer control system. Functional diagrams and mechanical drawings of all pertinent features are illustrated. Information on system assembly including practical lessons learned is included.

### 4.1 Electronic System

The electronic system is shown in Figure 19. Originally, it was to consist of a 8657B HP signal generator and a 8508A HP Vector Voltmeter. Both the signal generator and the vector voltmeter would be under computer control. Sweeping the signal generator via automated computer command and then retrieving the phase value from the vector voltmeter would allow the user to plot the phase curve over any specified bandwidth and with any resolution. The vector voltmeter combined with the signal generator and computer (already used to control the DMD) were designed to work as a low-cost network analyzer. In practice, this combination worked well, however the required communications between the instruments and the computer slowed down the entire process. Needless to say, this low-cost network analyzer provided us with less functionality than a network analyzer.

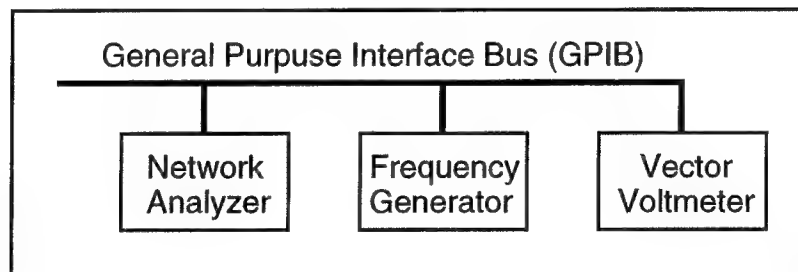


**Figure 19.** Test and measurement equipment.

During assembly of the system, an 8340B HP Synthesized Sweeper was used as the signal source and a Tektronix 2753 Spectrum Analyzer measured the output signal. Later, a 8753C HP Network Analyzer with an 85047A HP S-parameter set replaced the signal source and analyzer pair. The Network Analyzer has the advantage of being able to

measure both the magnitude and phase of a test signal. Obviously, phase is the critical parameter in phased array systems, thus it is absolutely necessary to have a mechanism to measure this quantity. Due to ease of use and its ability to provide both magnitude and phase data, the Network Analyzer remained as the primary piece of test equipment throughout the assembly of the beamformer and the subsequent data collection.

## **4.2 Optical System (as designed)**

The overall optical system is shown in the mechanical drawing, Figure 20. The active elements of the optical portion of the TTD beamformer are the acousto-optic cell, the binary optic, and the deformable mirror device (DMD). The functions of these individual components are to generate the heterodyne signal, replicate the signal 20 times, and control the time delay, respectively. Based on the active components, the optical system can be naturally divided into three subsections. The subsections of the optical beamformer will be referred to as the front end subsystem, the TTD replication and collimation subsystem, and the TTD selection and feedback subsystem, respectively. The following sections give a brief description of each subsection and trace the optical path illustrated in the figures.

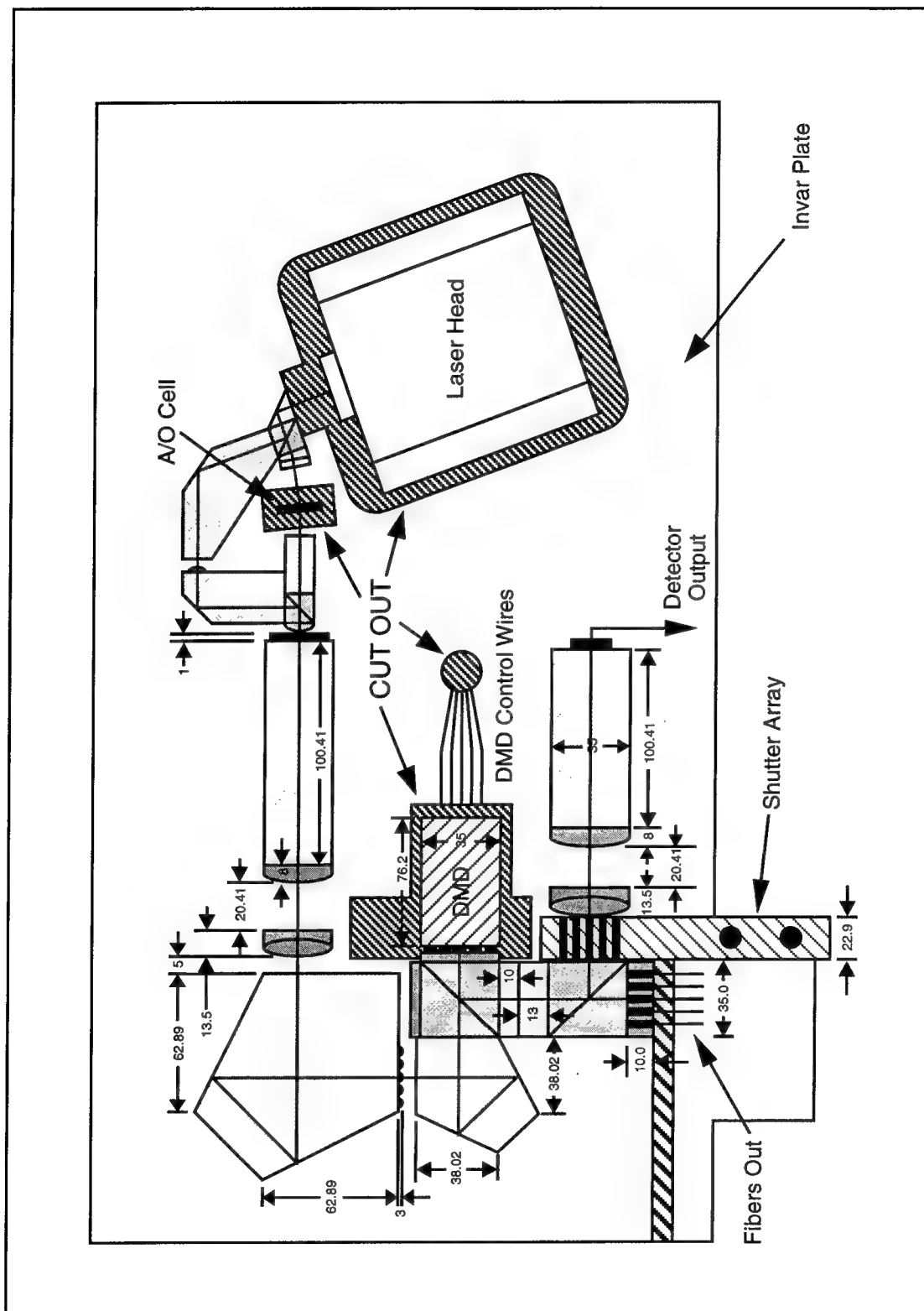


**Figure 20.** Mechanical Drawing of Optical Breadboard Design.



**4.2.1 Front End:** The purpose of the front end, Figure 21, is to make available a continuum of up to 100nsec of RF signal delay to be transmitted to the radar, and to impress the RF signal onto the optical carrier. This is all done through the acousto-optic (AO) cell which compresses the RF signal into an acoustic wave, and, through interaction with the laser beam, impress the RF onto the optical beam.

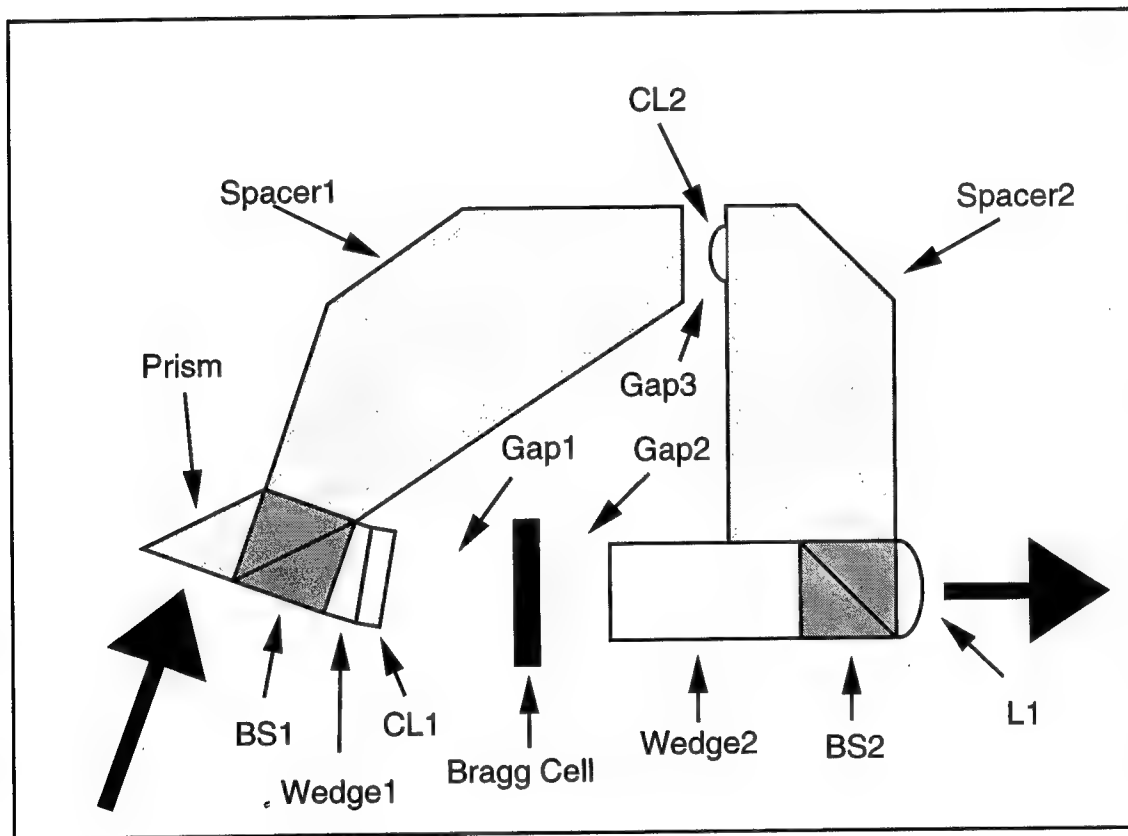


**Figure 21.** Front End Subsystem.

Now, we'll trace the optical path. The laser light from a Lightwave 122 laser is directed into the prism which redirects the light to the first beamsplitter, BS1. The light is initially polarized to an angle which results in the beamsplitter allowing 80% of the light to be directed to the AO cell and the other 20% travels a separate path around the AO cell, to be recombined with the light from the AO cell path at the output. More of the light is directed to the AO cell to compensate for the low diffraction efficiency of the cell (26%). The diffracted light power is approximately the same intensity as that in the reference leg so that

optimal heterodyning can occur. The detected heterodyne signal is maximum when the power in both beams is equal.

The desired RF transmit signal is fed to the AO cell from the electronic system. A cylindrical lens, CL1, focuses the light sent to the AO cell to a line that overlaps the acoustic wave path in the cell to increase diffraction efficiency. As the laser passes through the AO cell, approximately 20% of the light diffracts off of the grating and the radar signal is impressed on the optical carrier as a corresponding frequency shift. This signal beam is then combined with the reference beam at the second beam splitter, BS2. A final spherical lens, L1, collimates the signal beam in the vertical dimension, compensating for the focusing effect of the cylindrical lens, but it focuses the signal beam in the horizontal dimension. The signal beam continues to expand after focus through out the system. The angle of propagation is directly related to the horizontal, or off axis position. This is done to create a curved wavefront and allows the DMD, discussed later, to select the appropriate time delay. A small spherical lens, CL2, in the reference beam path focuses the beam so that the final spherical lens collimates the reference beam and magnifies it 2.25 times.

**4.2.2 TTD Replication and Collimation Subsystem:** The TTD replication and collimation subsystem, Figure 22, immediately follows the front end. In fact, it is butted right up against the spherical lens of the front end. Again, the purpose of this section is to replicate the heterodyne signal 20 times. Through the use of a single binary optic, this can be achieved without the need for 20 additional lasers or AO cells. Not only is this a weight and cost savings, but it also reduces complexity by not having to phase lock lasers.

The first surface is the binary optic (Appendix A contains information on development of the Binary Optic). The binary optic replicates the input beam 25 times in a 5 by 5 array. The TTD system consists of only 20 channels so the bottom row of 5 beams is not used. Next, these beams propagate through a rectangular spacer block while diverging with respect to each other. A spherical lens, L2, cemented to the end of the block in combination with a doublet, L4 and L3, collimate the 20 beams with respect to each other. The lens also focuses the individual beams so an array of 20 microlenses, L5, are needed to recollimate the individual beams. The microlenses are cemented to the output face of the penta-prism. The penta-prism is used to increase path length while keeping the entire system compact, and also to keep as much of the optical path in glass to minimize phase distortion due to air currents.

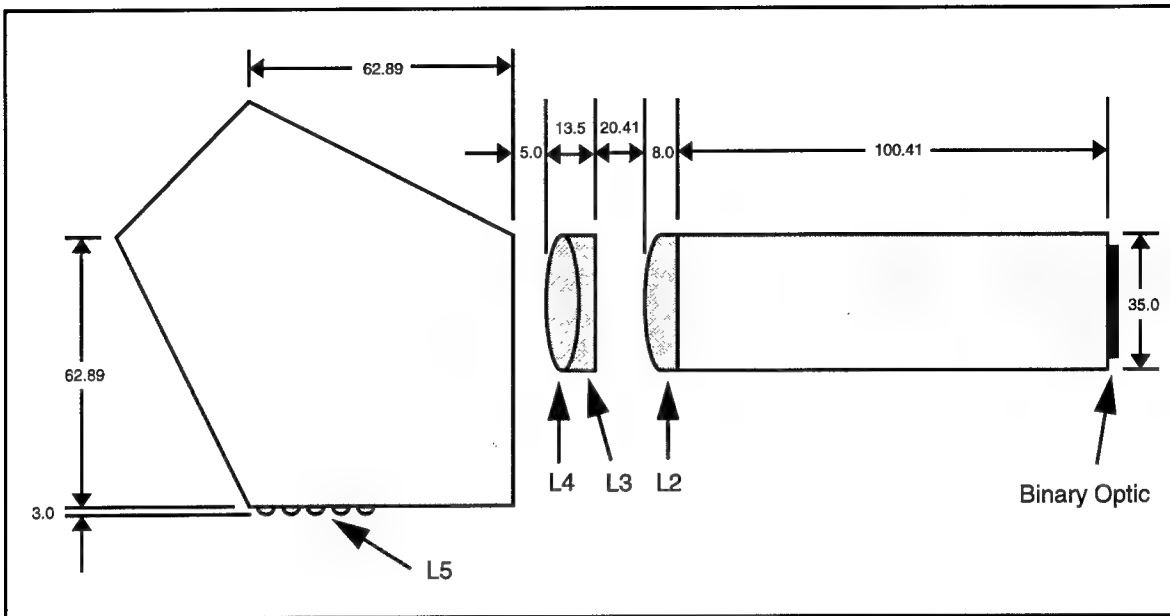


**Figure 22.** TTD replication and collimation subsystem.

**4.2.3 TTD Selection and Feedback Subsystem:** The final subsystem, shown in Figure 23, actively controls the time delay selection and contains the feedback portion of the optical system. The first element is a smaller penta-prism used to fold the beams. A polarizing beamsplitter separates the signal and reference beams. The reference beam reflects off the beamsplitter to one side of the cube. A quarter wave plate cemented on the face of the cube rotates the polarization to circular polarization. The back of the quarter wave plate is mirrored so that the beam is reflected back on itself and makes a second pass through the plate. This completes the polarization rotation to a full 90 degrees making the reference beam the correct polarization to now pass the beamsplitter. The reference now travels towards the output. The signal beam is initially the correct polarization to pass the beamsplitter, but it too passes a quarter wave plate on the other face of the beamsplitter on its way to the DMD. After reflecting off of the DMD, it too completes a full 90 degrees of rotation as it passes the quarter wave plate a second time. Now the beam reflects off of the beamsplitter towards the output of the optical system.

The DMD consists of 20 individual mirrors arranged in a 5 by 4 array. Each is controlled by three piezo-electric (PZT) crystals. The three PZT's act to give the mirror full tip and tilt as well as piston control. Depending on the tilt of the mirror, a specific location in the AO cell is imaged at the output of the optical system. The vertical tip of the mirror segment can

also be used to affect the amplitude of the heterodyne signal. Piston of the mirror is important for the proper phasing of the channel signals. If the path lengths of the channels are not the same, then a phase difference exists between channels and a good beam profile will not be achievable. The heterodyne process preserves phase information, meaning that an optical phase difference becomes a RF phase difference. Since many waves of the optical carrier can exist in a short space (recall that  $\lambda = 1.3\mu m$ ), phasing of the mirror segments is critical.

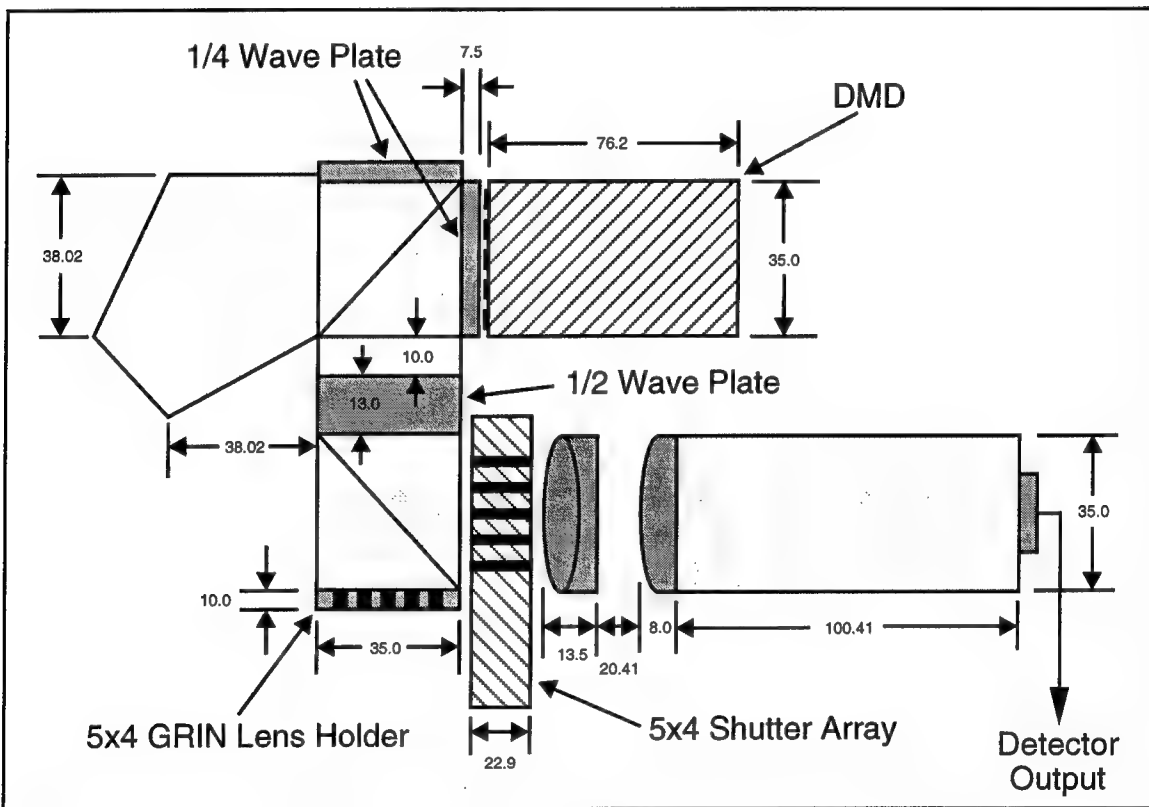


**Figure 23.** TTD selection and feedback subsystem.

The reference and signal beams now travel past the beamsplitter, through a glass spacer, to a half wave plate. The wave plate changes the polarization of all the beams to circular. The purpose of this—in combination with the next beamsplitter in the path—is to split each of the reference and signal beams in equal halves to the output of the system and the feedback portion of the system. The polarizing nature of the cube also ensures that the reference and signal beams are the same polarization so that they will heterodyne effectively.

Finally, the output path is directed to an array of multi-mode grin rods which carry the signal to the antenna array. Multi-mode grin rods were chosen over single mode grin rods due to the lack of available power per channel. Single mode grin rods would be preferred because of the absence of many modes of propagation, and thus produce a cleaner signal. Single mode grin rods are not used in our system due to low coupling efficiency and the difficulty of alignment. Additionally, in the TTD system, the division of the initial laser power into 25 channels left little signal power for coupling into the grin rods.

The feedback path uses light reflected off the last beamsplitter. The light passes a shutter array, which permits individual channel analysis. The shutter array can be programmed (via computer control) in any combination to allow light to pass or not pass from individual channels or groups of channels. For the TTD system, it is used to allow only one beam to pass at a time. Next, a summing lens combination that is the exact duplicate of the collimating assembly in the TTD replication subsystem, focus all the beams to a single detector. The detector is used to verify and actively adjust the time delay of the individual channels.

### **4.3 Antenna System**

The antenna back-plane is shown in Figure 24. This section mates directly to the back of the antenna built by Lockheed-Martin. The grin rods from the optical system are fed to an array of Antel Optronics fiber coupled photodetectors. In our system, there is approximately 10 meters of fiber between each grin rod and detector pair. The heterodyne signal is converted to an electrical signal at the detectors, where it is further amplified by JCA 12-3115A amplifiers. The amplifiers feed the signal to the individual antenna elements.

The amplifiers have a gain potentiometer adjustment to allow for more or less signal to be supplied to the antenna element. For optimum performance of the antenna, it is important to have all the elements at approximately the same power level. Matching the magnitude of each channel is not as important as having the phases properly adjusted (Appendix A contains a diagram of the amplifier biasing circuit).

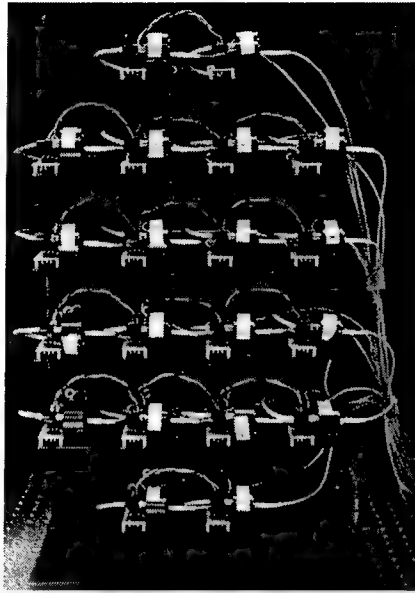


**Figure 24.** L-band antenna back plane.

#### **4.4 Computer Control System (as designed)**

The optical beamforming system is designed to use a single computer as the experiment controller. The computer is a standard IBM PC compatible computer (486-based computer running at 25MHz). As shown in Figure 25, the computer uses two interfaces to control the system. First, the COM1 serial port is used to control the Mirror Control Electronics. A General Purpose Interface Bus (GPIB) card is installed in the computer to serve as the second interface to external components. The shutter electronics are controlled via the GPIB interface. All of the test and measurement equipment is also controlled by this computer via the GPIB.

The Mirror Control Electronics (MCE) were built by Thermotrex to control the 20 segment segmented mirror device (DMD) in the optical system. The MCE is a self-contained mini-rack mount that houses both the DMD driver cards and requisite high voltage power supplies, as well as a 486-based PC compatible computer that is used to control the operation of the DMD<sup>2</sup>. This MCE-computer is mounted to the VME bus in the MCE. In

---

<sup>2</sup>A historical note: The current MCE is greatly improved from the original version. In the original MCE, the MCE-computer was a 68000 - based single board computer that allowed external control via a serial port through a monitor program running from the on-board ROM. This board required additional control computer software to parse monitor commands, etc. to control the DMD. During a repair cycle of the

this configuration, the MCE-computer is able to issue commands on the VME bus to control all aspects of the high voltage control cards that power the DMD. Thermotrex provided software ('C' source code and executables) for this MCE-computer that controls many positioning functions available for the DMD. We modified the Thermotrex software to accept commands via the COM1 serial port on the MCE-computer. With this interface, it is possible to issue commands to the MCE from the main system control computer. To accomplish complete control of the DMD, we wrote a set of complementary software to run on each computer. The software includes a high-level handshake protocol that allows the controlling computer to know that the command executed properly on the MCE-computer. This control scheme worked well during operation of the integrated system.

A National Instruments GPIB interface card is installed in the control computer, and the control computer is set as the bus-master. The electronics for the shutter in the optical system is controlled via GPIB. Using this configuration, the control computer can signal the shutter to open each of the 20 channels individually as part of the feedback loop. The GPIB is also connected to the group of rack-mounted test and measurement equipment.

---

DMD, this single board MCE-computer was replaced with a VME-bus PC-compatible computer. Thermotrex also delivered control software (written in C) that accessed the VME bus. These modifications enabled significant improvements in how the DMD is controlled.

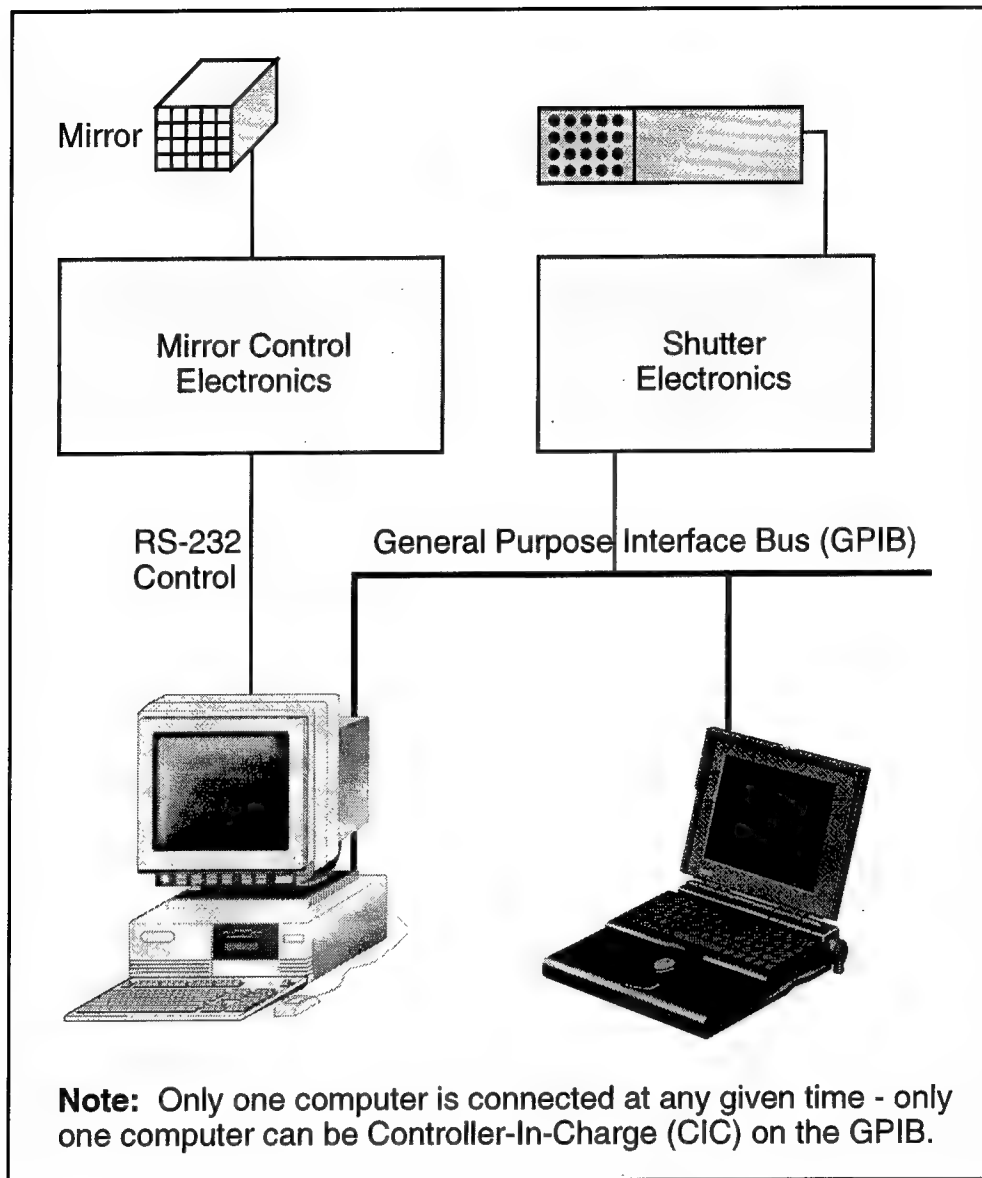


**Figure 25.** Computer control system.

#### 4.5 Optical System (As Built)

The actual assembly of the optical system encountered some difficulties. Many of the problems arose from the use of off-the-shelf optics which were not optimal for the system. Another unique challenge of the whole optical assembly was the fact that all of the optics had to be glued to an invar plate. This left little flexibility in adjusting the optics once they



were in place, and naturally, any imperfections in the optical path are carried throughout the system. Finally, the invar plate itself was a source of problems in the final performance of the beamformer.

In the optical assembly, two major problems were encountered. The first involved the alignment of the front end and subsequent effects on the heterodyne signal. Second, the placement of the microlenses, L5, in Figure 22, led to the beams propagating along slightly different paths with respect to one another. This led to a problem in the feedback path, but did not disturb the signal sent to the antenna.

The front end was designed with off-the-shelf optics which were not optimal for the system. The end result was that the reference beam and local oscillator did not overlap well. This had a negative effect on the efficiency of the heterodyne signal. A secondary effect was that the wavefront of the reference and signal beams at the detector, varied with frequency, giving a quadratic phase curvature in the RF signal when plotted versus frequency. Although all 20 channels exhibited the same general curvature, the beam profiles didn't suffer as long as all 20 channels varied in the same amount. The curvature could be minimized by adjusting the position of the AO cell along the optical axis, effectively changing how it is imaged onto the detector, and thus flattening the RF phase [18,19].

The second problem involved the microlenses (L5 in Figure 22). Two problems with the lenses were the quality of the lenses themselves, and the alignment of the lenses in the optical system. The main effect of imperfections in the lenses and their misalignment was to cause the 20 beams to no longer be collinear. This would not have mattered, except the design of the feedback system depended on summing optics to bring all 20 beams to focus on a single small area detector (the GRIN rods at the output could be independently positioned to adjust the alignment of each channel). Because of the divergence of the beams with respect to one another, the spots at the focal plane did not all overlap on the detector as designed. The best we could achieve was 5 channels focused on the detector at once. Unfortunately, the use of a larger detector is not an option since larger area detectors do not provide the needed frequency response. Figure 26 illustrates the separation of the channels at the focal point with respect to the size of a typical detector.

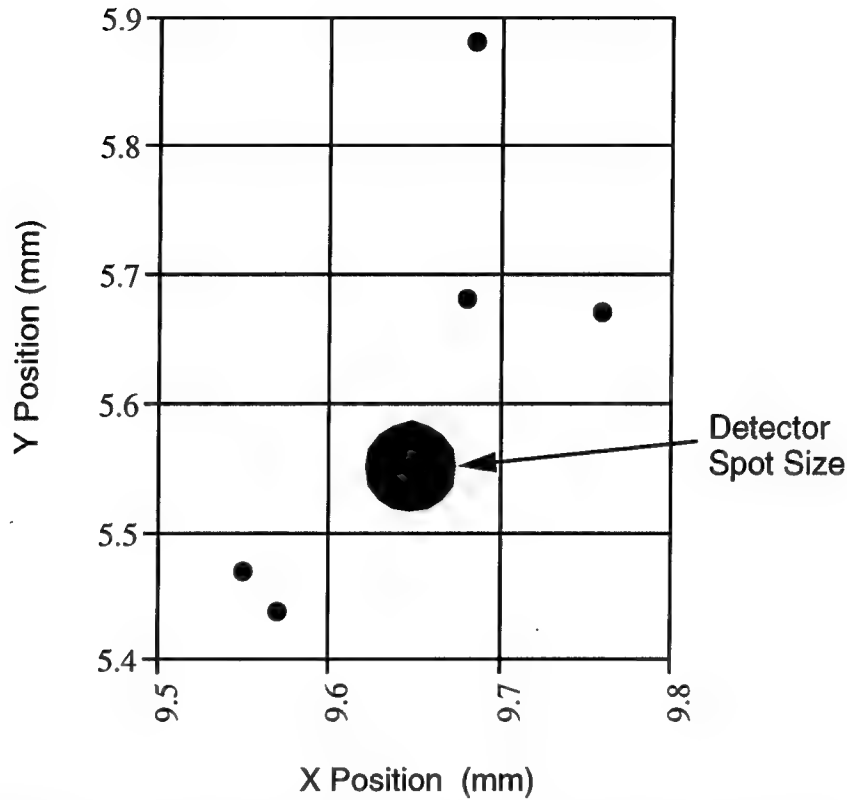


**Figure 26.** Spot locations of the five channels at the focal plane of the feedback loop.

The microlenses were a stock Melles Griot item, but the diameter was too large. The lenses were cut down to a smaller diameter to fit in the system but in the process of resizing them, the optical axis did not always remain coincident with the mechanical axis. In other words, the optical center was displaced from the physical center of the lens. The misalignment varied as much as 2mm. Considering that the diameter of a microlens was only 5mm, 2mm was a large error. Lenses that we determined to be 'good' (minimal centering error) were used in the system, and new ones were ordered to replace the unusable ones.

The alignment of the lenses and placement on the block was facilitated by the use of a Helium-Neon laser. Channel (3,3) of the 20 beams travels along the optical axis of the bulk optics and was used as a reference for aligning all 20 channels. First, the HeNe was aligned to be collinear with the optical axis of a reference lens such as the doublet combination L3 and L4 in Figure 22. Next, the microlenses were aligned to the HeNe, the reflections from the front and back of the lens were centered on the HeNe beam to produce a bull's-eye interference pattern. A drop of optical cement was then placed on the lens and it

was carefully moved into contact with the pentaprism, while maintaining the alignment. The position of the other channels was known and the laser was translated on micrometer stages to the next channel and the process was repeated. The alignment was also checked by looking at the location of the spots at some distance with an IR camera and beam profiler. Although the alignment seemed correct, even small errors lead to problems at the focal plane (recall that the detector diameter is 50  $\mu\text{m}$ ). In retrospect, the alignment may have been more accurate if the feedback path and detector were set up to aid in the alignment of the lenses. This would have helped to make sure that all 20 spots fell on the detector.

The final difficulty affecting the whole assembly was the placement of all of the optics on the invar plate while the active elements—the laser, AO cell, and the DMD—were placed on an aluminum plate 5 inches below. The invar is attached to the aluminum by six individual 3/4 inch diameter posts. This created vibration problems, especially for the AO cell which is fixed on top of a 2.5 inch post that is mounted to a translation and rotation stage on the aluminum plate. The DMD is also fixed on top of a 4 inch post that is attached to a stage on the aluminum plate. The AO cell suffers the most vibration due to a mount that is not as rigid as the others. Naturally, the long lever arms that these elements were placed on only aggravated the situation.

#### **4.6 Computer Control System (As Built)**

During the actual testing of this system, the GPIB-controlled shutter was never used. Once we discovered that the 20 beams did not align to a single detector (in the feedback path), it was clear that the shutter would serve no purpose, and we would not continue with its integration into the system. Additionally, we used the HP Network Analyzer exclusively to measure phase in the system. Since the Network Analyzer was a relatively new piece of measurement equipment inserted into our system (replaced the frequency generator and vector voltmeter combination), no existing software for our controller computer existed. Given that we were also not going to pursue the feedback loop and its requisite software development, we chose instead to use a working Macintosh data acquisition system to test and measure the system performance. The Macintosh data acquisition system, which included its own GPIB hardware, allowed us to test and measure various operational characteristics of the system. Additionally, the software for the Macintosh allowed us to

---

easily acquire and save system data. The final control system used in this experiment consisted of this Macintosh-based data acquisition system and a PC-based mirror control system. Instead of integrating the system into a fully closed-loop experiment, we opted for keeping a human in the feedback path as we measured parameters necessary to understand how well the entire system worked.

## 5.0 Experimental Results

This section documents the experimental performance of the photonic TTD beamformer. First, the experimental set-up is described. Measured magnitude and phase data along with simulated beam patterns are plotted. Data for steering the beamformer to 0, 30, and 60 degrees is included. Additionally, the performance of the photonic TTD beamformer is compared with that of an ideal phase shifter (one that applies the same phase shift to all frequencies). Also presented is a comparison the integrated photonic TTD system and a free space predecessor.

### 5.1 Experimental Set-Up

The experimental set-up is illustrated in Figure 27. The HP 85047A S-Parameter Test Set generates a -10 dBm test signal which is then amplified by the 40 dB Mini Circuits Amplifier, model ZHL-4240. The amplified signal drives the acousto-optic (AO) cell in the integrated system. This amplified input signal is the desired RF transmit signal. In order to simulate the application of a wide bandwidth signal, the test signal generator sweeps over the range of the desired bandwidth. As previously described, a grating is set up in the AO cell and the test signal is impressed on the laser light carrier (refer to this as the signal beam). The orthogonally polarized reference and signal beams propagate through the system.

The DMD selects the desired time delay by tilting to an appropriate angle. The DMD and its requisite Mirror Control Electronics (MCE) are controlled by a central controlling computer (a PC) via a serial interface as described earlier in Section 4.4 of this report. A program running on the PC accepts commands to move the DMD segments to a certain position. Using known actuator influence functions (calculated a priori) for each actuator, the software then processes the command to determine the required actuator movements that will affect a positional change of a DMD segment. Once the new actuator positions are known, they are sent to the MCE, where the command is translated into a series of high voltage settings that are applied to the actuators.

Once the DMD is positioned properly, an appropriately delayed version of the signal beam and the reference beam propagate through the system and are coupled by a GRIN rod into a multi-mode fiber. The fiber then feeds the signal and reference beams onto a photodetector

where the optical heterodyning (mixing) is accomplished. The band-limited photodetector detects and passes the difference frequency between the signal and reference beams (the RF transmit signal) and filters the sum. A variable 10-30 dB JCA Technology Amplifier, model JCA12-3115A, amplifies the RF transmit signal which is then input to an HP 8753C Network Analyzer.

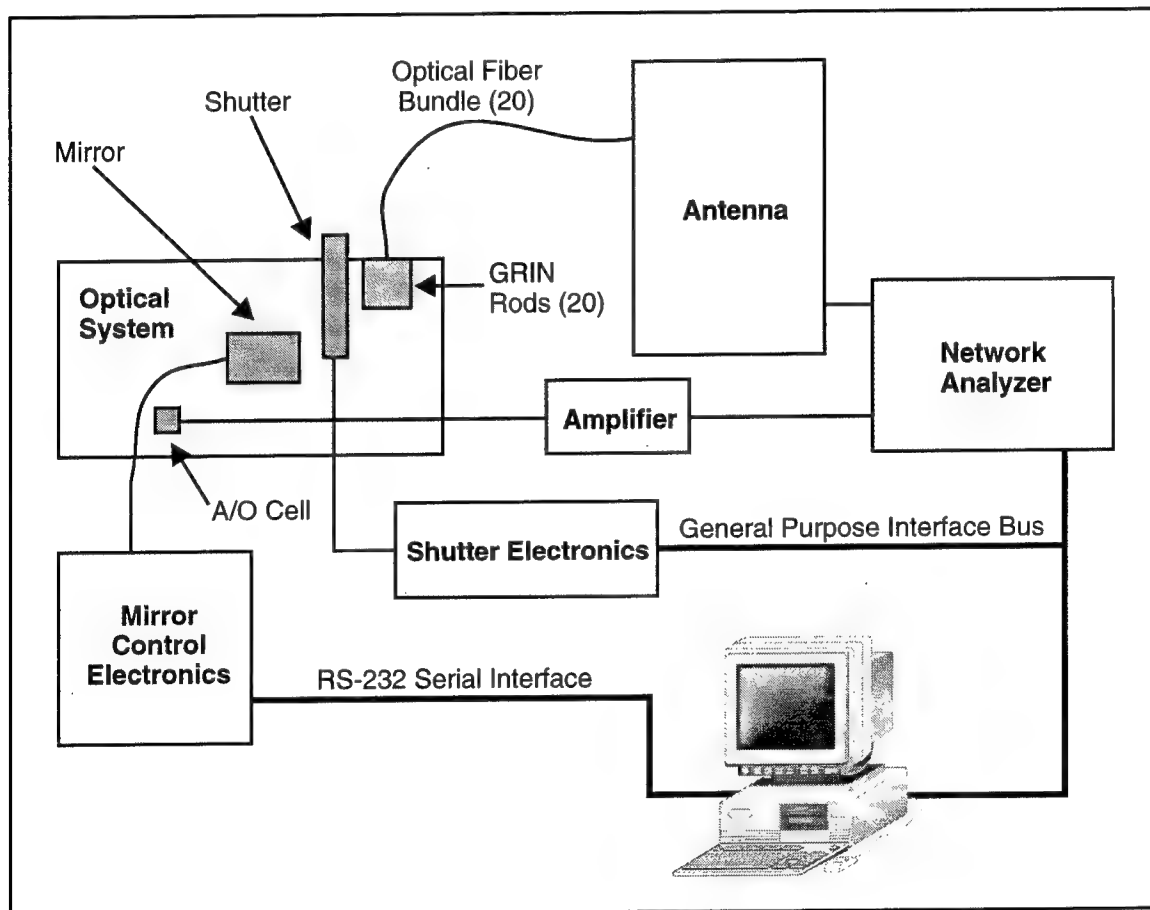


**Figure 27.** Experimental set-up.

**Note:** Specifications on the AO-cell, DMD, GRIN rod, and photodetector are documented in Appendix A.

## 5.2 The Experiment

The experimental goal of the project is to evaluate the performance of the photonic TTD beamformer in reducing/eliminating beam squint. System performance at three different beam steering positions (0, 30, and 60 degrees) is analyzed and evaluated. To accomplish

this goal, the appropriate time delays for each of the twenty antenna elements are calculated using the following:

$$\tau = \frac{d \sin \theta}{c} \quad (29)$$

where  $\tau$  is time delay,  $d$  is the element spacing (for our system  $d = \lambda/2 = 0.115 \text{ m}$ ),  $\theta$  is the steering angle of the main lobe, and  $c$  is the speed of light. A set of time delays are computed for each of the three beam positions.

Using the experimental set-up described above, the network analyzer measures magnitude and phase over a frequency range of 100 MHz (1.25 - 1.35 GHz). A simulator program accepts the measured magnitude and phase data as inputs and generates the beam pattern for a single specified frequency. This program also performs an FFT on the magnitude and phase data at a single frequency and plots the resulting beam pattern. Wide band performance is evaluated by generating beam patterns at multiple single frequencies and examining the amount of beam squint for each.

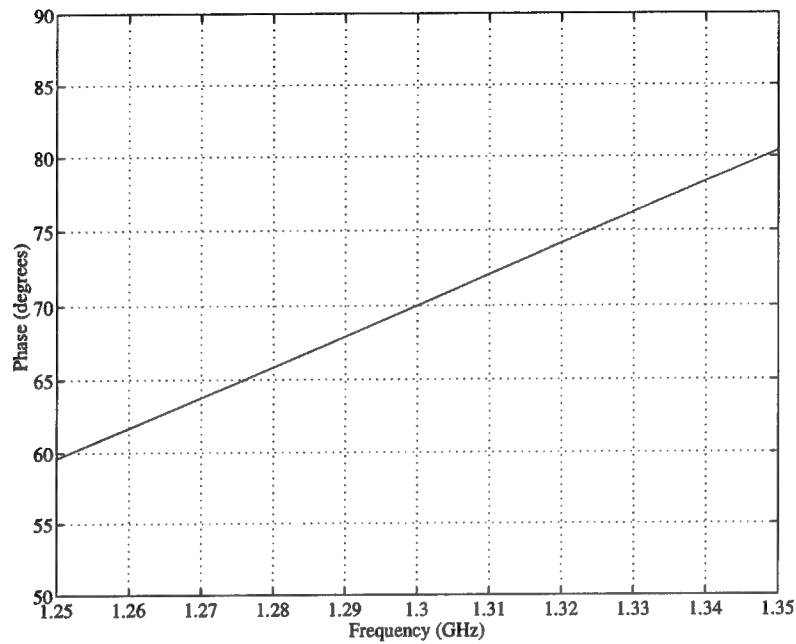
Measurements of magnitude and phase for all twenty channels in the two dimensional phased array were made at 0, 30, and 60 degree beam positions. However, for simplification of the analysis, the beam patterns of a single row (a five element line array) are shown. The results of the five element line array are quite sufficient for illustrating the proof-of-concept.

## 5.3 Data

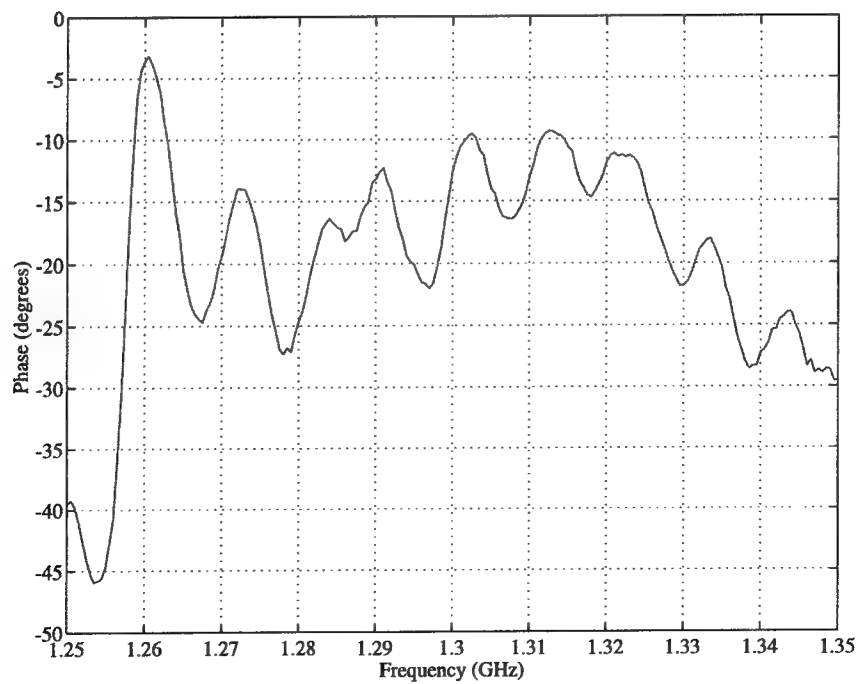
**5.3.1 Single Channel Data:** A perfectly functioning TTD system exhibits a linear relationship between phase and frequency (See Figure 28). In order to steer the main lobe, properly phased signals (i.e. signals with the correct slope) are sent to the individual antenna elements. For an array steered to broadside (0 degrees), the slope of the line is zero; meaning the same phase shift is applied to all frequencies.

Figure 29 shows the measured data of phase vs. frequency for a single channel. Any deviation from the desired zero slope linear relationship between phase and frequency

manifests itself as beam squint. For the channel shown, phase deviation ranges over approximately  $\pm 9$  degrees for the 60 MHz operational bandwidth.



**Figure 28.** Phase vs. frequency for a single channel of an ideal TTD system.



**Figure 29.** Phase vs. frequency for a single channel of the Photonic TTD system.



This phase deviation is typical of all twenty channels as illustrated in Figure 32.

Imperfections in the system's optical surfaces contribute to phase deviation. Over 20 separate optical surfaces make up the integrated system. To keep costs affordable, most of the optical components were obtained from off-the-shelf stock. Each of these surfaces has the potential to degrade the system performance with respect to phase. The additive effects from all the surfaces result in the significant phase deviation observed. With the range of phase deviation measured, beam squint is expected.

Figure 30 displays magnitude vs. frequency for the same single channel. Obviously, the ideal relationship between magnitude and frequency is linear with zero slope. The system bandwidth (-3 dB bandwidth) is shown to be approximately 60 MHz. The system is designed to have a bandwidth of 200 MHz. The system bandwidth is limited by the optical system as discussed in Section 3.3. Note that deviation of the magnitude response from the ideal has no effect on the pointing accuracy of the main beam. Thus, magnitude deviation does not contribute to beam squint, but rather affects the location of the sidelobes and the depths of the nulls in the antenna pattern.

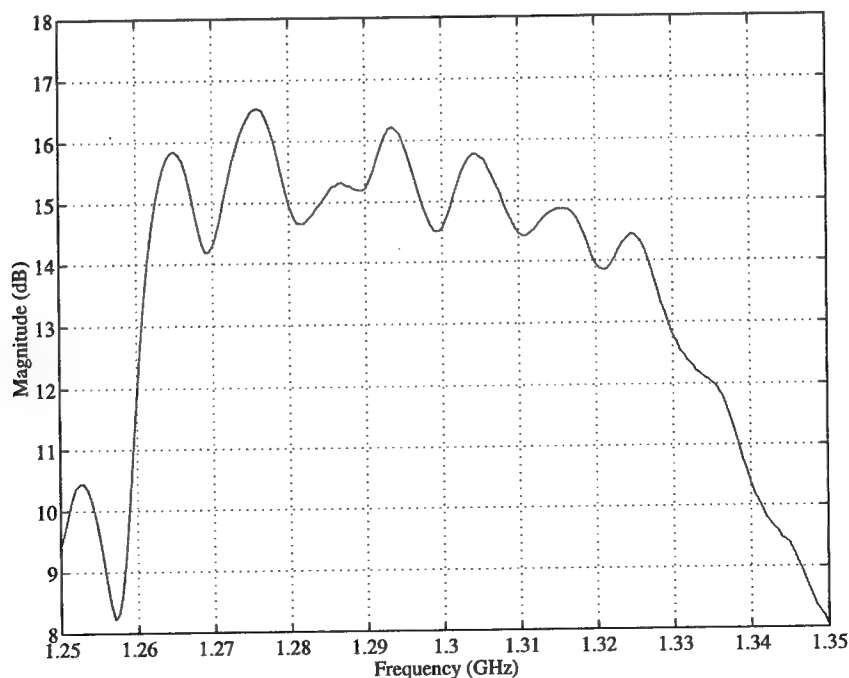


**Figure 30.** Magnitude vs. frequency for a single channel of the Photonic TTD system.

**5.3.2 Twenty Channel Data:** Figures 31 and 32 show the magnitudes vs. frequency and phases vs. frequency respectively for all twenty channels as the antenna is steered to broadside zero degrees. The data was collected using 1.3 GHz (the antenna design frequency) as a reference and forcing all the channels to have the same phase value at the reference frequency while maintaining zero slope for each channel. Two problems surfaced that made these measurements challenging. First, each channel drifts rather quickly, thus exacerbating the problem of fixing all twenty phases to a single phase value at the reference frequency. Second, the measured phase vs. frequency relationships are quite curved making the judgment of zero slope difficult.

This 20 channel data (Figures 31 and 32) is presented to illustrate the uniformity between channels and for completeness. An outlying channel clearly separates its performance from the rest. The outlier is caused by a GRIN rod with poor coupling efficiency.

**5.3.3 Five Element Line Array Data and Beam Patterns:** While data was taken for all twenty channels at each of the three steering angles (0, 30, and 60 degrees), only a single row of five elements are used for generating the beam patterns. The reduction to a five element line array simplifies the analysis and clarifies the presentation of the results. From this point forward, the report addresses only those five elements used for evaluating the proof-of-concept.

A computer simulator program accepts the measured magnitude and phase data as input and generates the beam pattern for a single specified frequency. The simulator performs an FFT on the magnitude and phase data at a single frequency and plots the resulting beam pattern. Wide band performance is evaluated by generating beam patterns at several different frequencies and examining the amount of beam squint for each. Each figure represents system performance at a different specified frequency. The amount of deviation in angle from the desired steer angle (specified in each section) to the actual main lobe position at the specified frequency is the beam squint. For comparative analysis the software generates the beam pattern of a simulated perfect phase shifter (a phase shifter applying the identical phase to each frequency across the band). The phase shifter is set so that 1.3 GHz steers the line array to the desired angle. In the figures, a dashed line represent the beam pattern of the Photonic TTD system and a solid line represents the beam pattern of an simulated Perfect Phase Shifter at a single specified frequency. Also, a horizontal dashed line is plotted to mark the 3dB points.

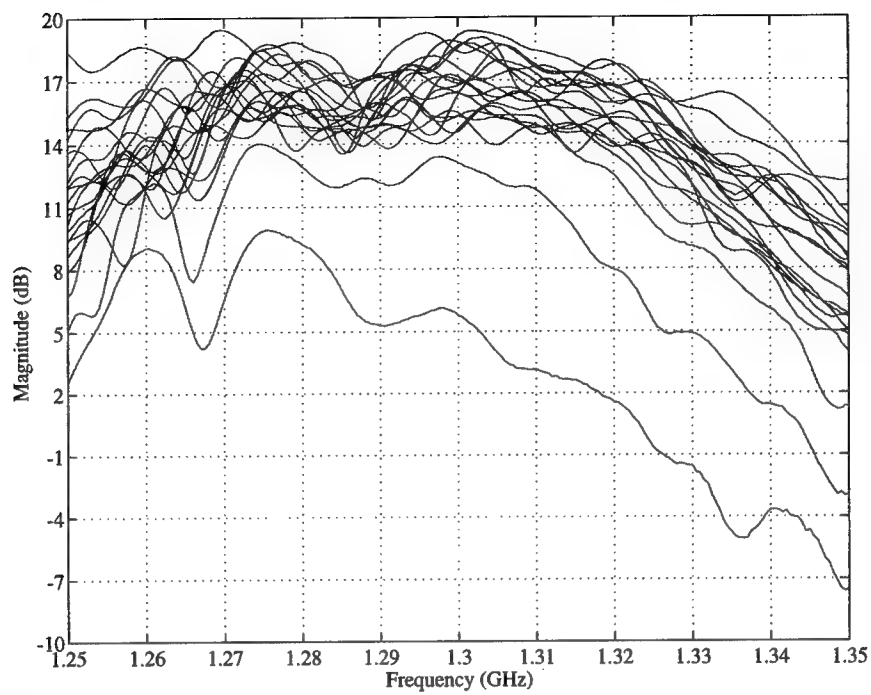


**Figure 31.** Magnitude vs. frequency for all twenty channels of the Photonic TTD system.

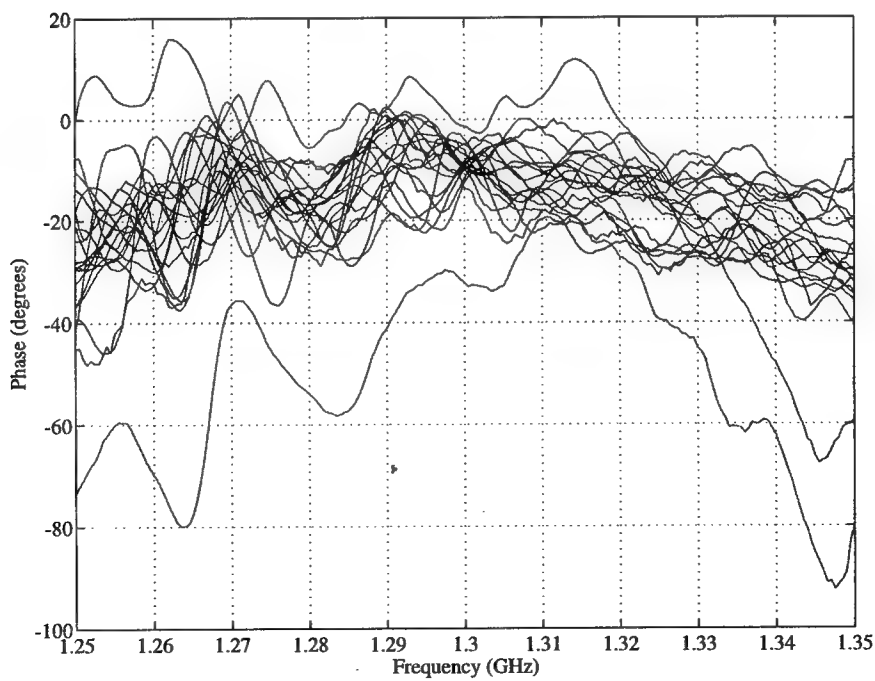


**Figure 32.** Phase vs. frequency for all twenty channels of the Photonic TTD system.

**5.3.3.1 Five Element Array Steered to Broadside (0 degrees):** Figures 34 and 35 show the phases vs. frequency and magnitudes vs. frequency respectively for a five element line array steered to broadside (zero) degrees. The ideal phase vs. frequency relationship for all five channels is linear with zero slope as shown in Figure 33. Upon examination of Figure 34, which shows the phases vs. frequency, similarities in shape (i.e. the correlation of peaks and valleys) between the five channels become evident. This phenomena indicates that the major factors/components causing the phase deviations are common to all channels. Thus, components such as the microlenses, DMD elements, and GRIN rods are eliminated from consideration as significant contributors to the phase deviation. The optical surfaces in common impose the major detrimental effects on phase over the bandwidth. Note: when comparing Figures 33 and 34, the ideal and measured TTD phase vs. frequency data, keep in mind that only the relative phases between the channels and not the absolute phases are important.

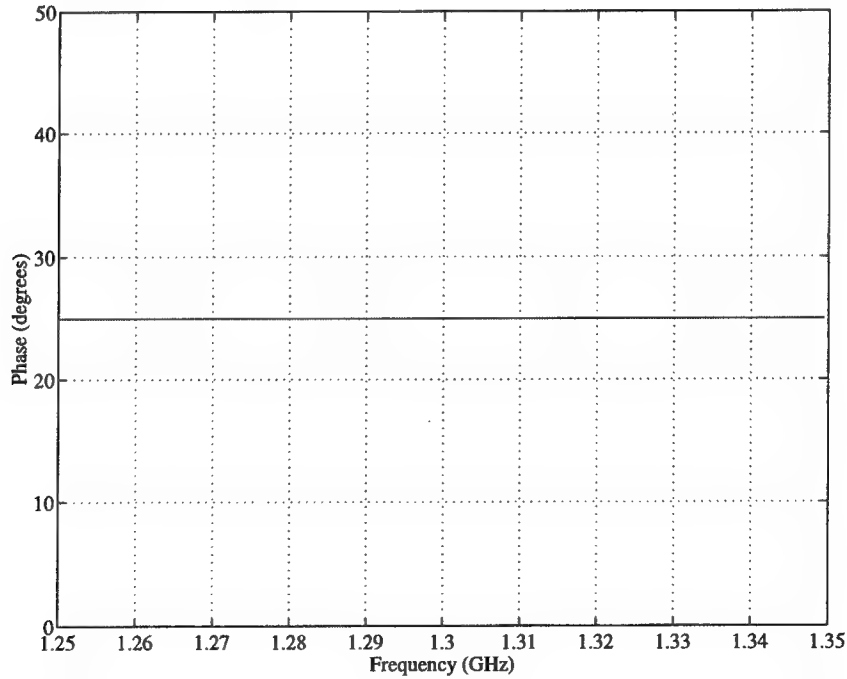


**Figure 33.** Phase vs. frequency for a five element delay line of an ideal TTD system.

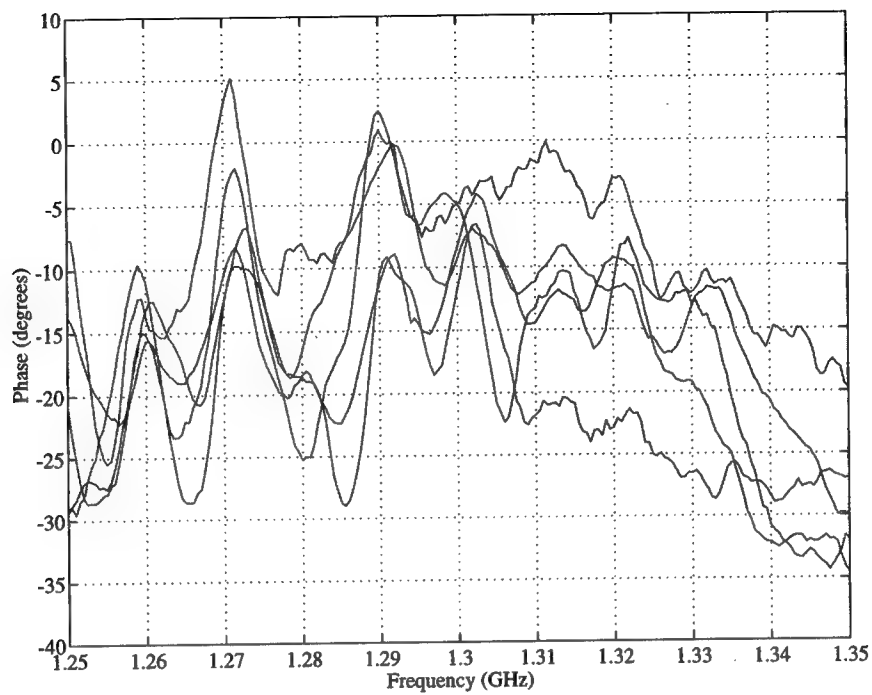


**Figure 34.** Phase vs. frequency for a five element delay line of the Photonic TTD system.

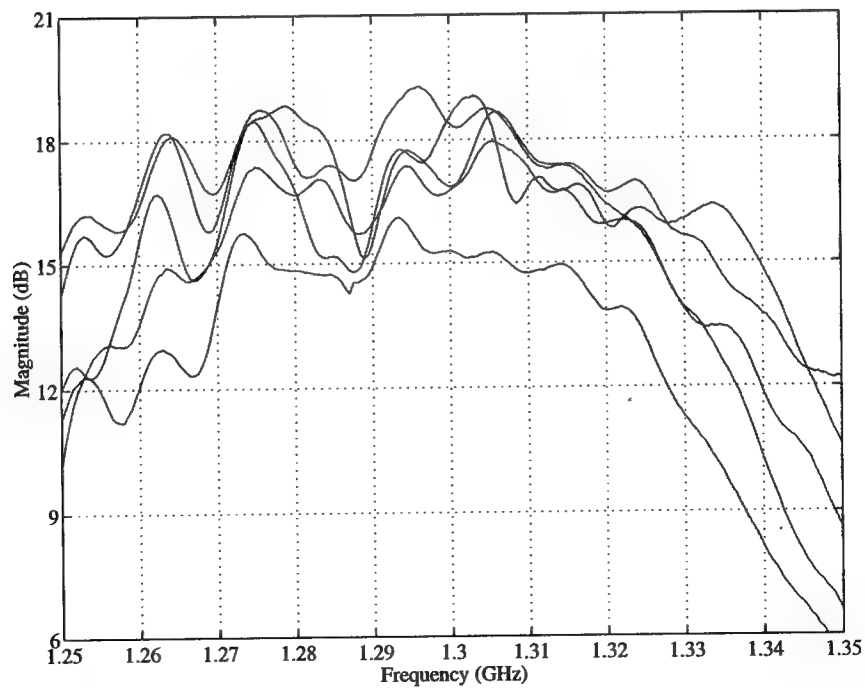


**Figure 35.** Magnitude vs. frequency for a five element delay line of the Photonic TTD system.

Beam patterns for the broadside case are plotted in Figures 36, 37, and 38 for frequencies 1.25, 1.275, and 1.3 GHz respectively. The amount of deviation in angle from the desired steer angle of zero degrees to the actual main lobe position at the specified frequency is the beam squint.

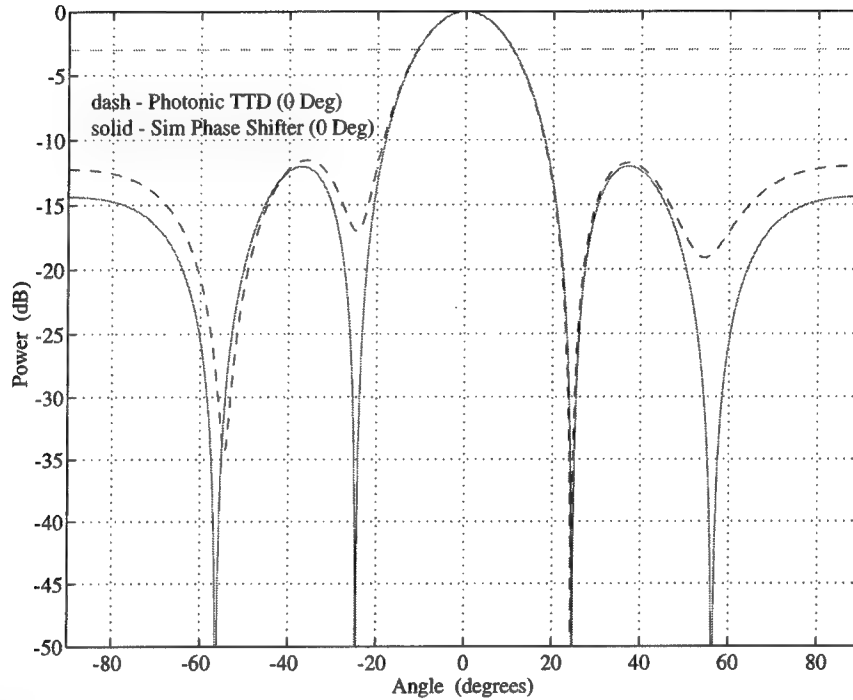


**Figure 36.** Beam patterns at 1.25 GHz of the Photonic TTD system and the perfect phase shifter.

Figure 36 shows the beam pattern for 1.25 GHz. Both the Photonic TTD beamformer and the simulated perfect phase shifter steer the main lobe to zero degrees as desired.

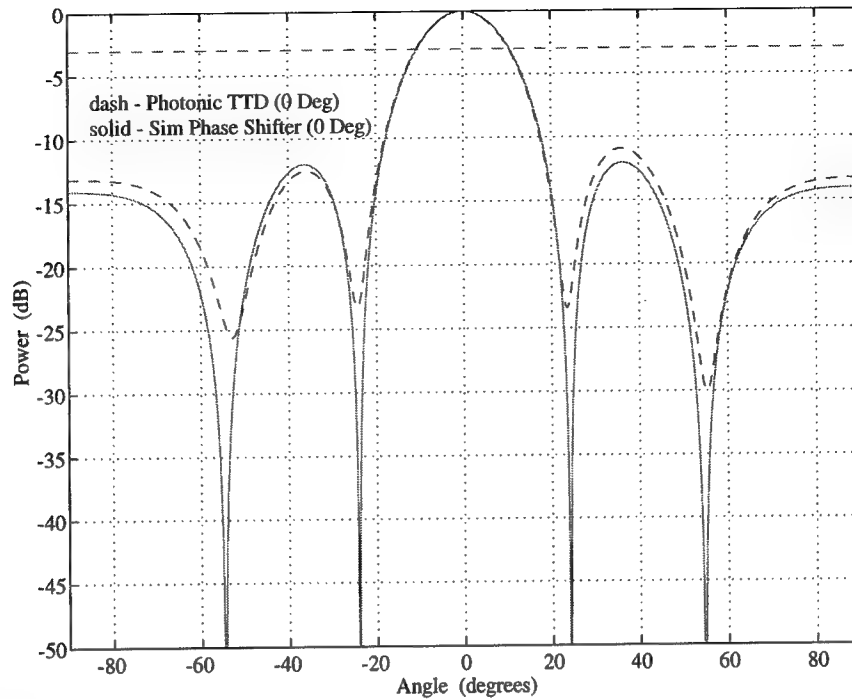


**Figure 37.** Beam patterns at 1.275 GHz of the Photonic TTD system and the perfect phase shifter.

Figure 37 shows the beam pattern for 1.275 GHz. Both the Photonic TTD beamformer and the simulated perfect phase shifter steer the main lobe to zero degrees as desired.

Figure 38 shows the beam pattern for 1.3 GHz. The Photonic TTD beamformer steers the main lobe to -0.35 degrees, while the simulated perfect phase shifter steers the main lobe to zero degrees as desired. Thus, the beam squint of the Photonic TTD system is 0.35 degrees. For the broadside case, the simulated perfect phase shifter suffers no beam squint (as expected).

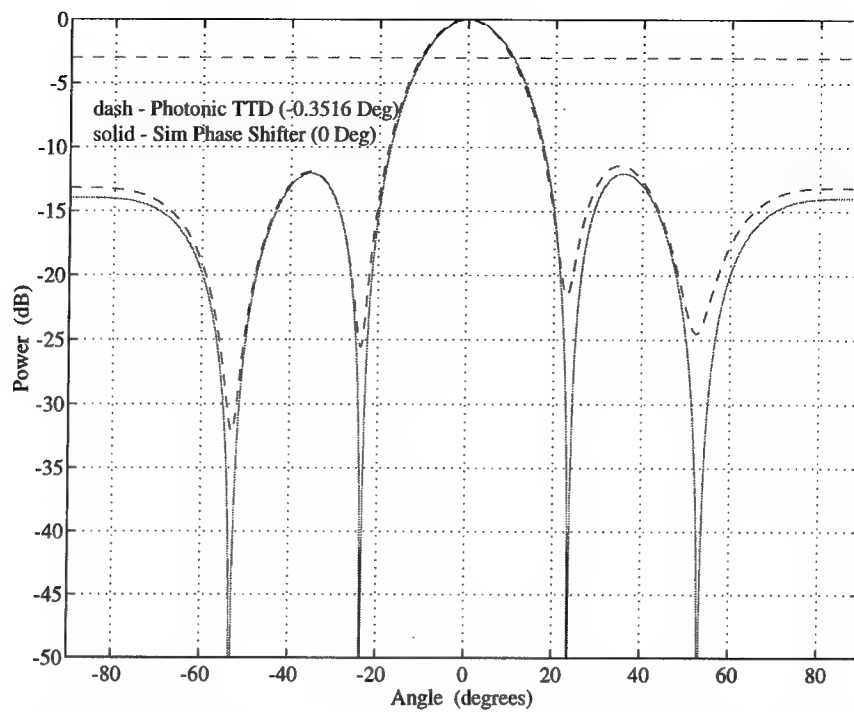


**Figure 38.** Beam patterns at 1.3 GHz of the Photonic TTD system and the perfect phase shifter.

**5.3.3.2 Five Element Array Steered to 30 Degrees:** Figures 40 and 41 show the phases vs. frequency and magnitudes vs. frequency respectively for a five element line array steered to 30 degrees. When comparing Figures 39 and 40, the ideal and measured TTD phase vs. frequency data, keep in mind that only the relative phases between the channels and not the absolute phases are important.



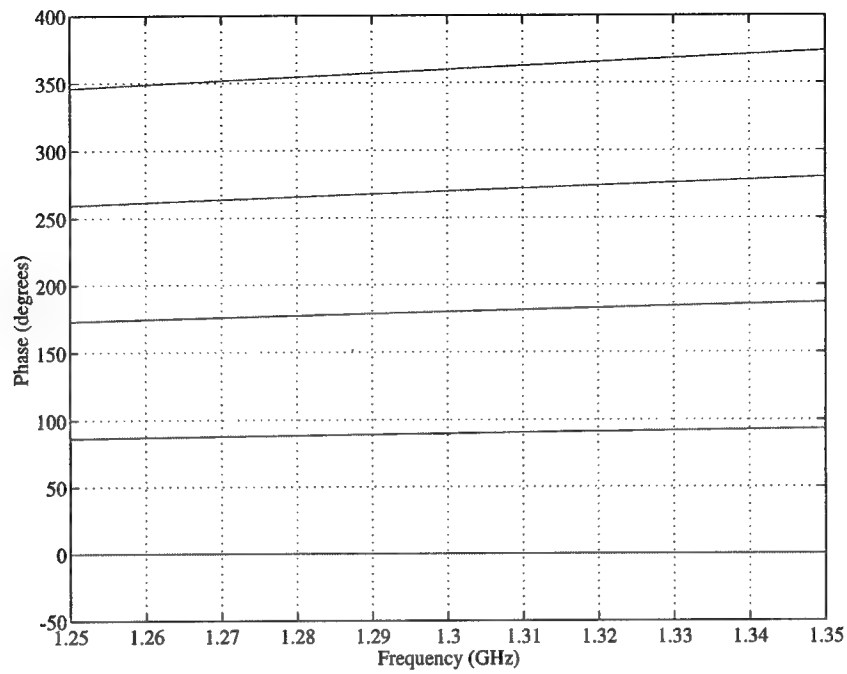


**Figure 39.** Phase vs. frequency for a five element delay line of an ideal TTD system.

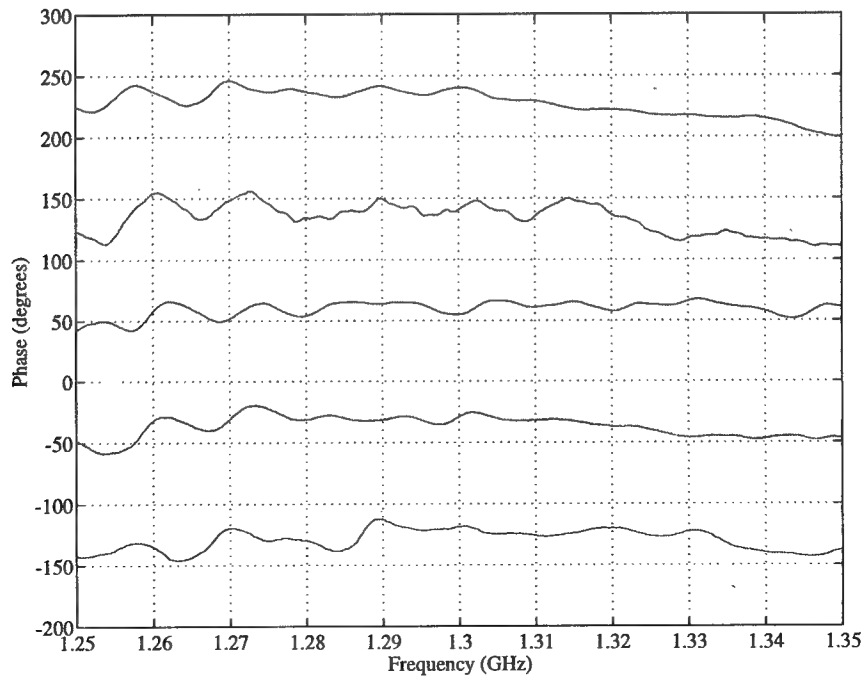


**Figure 40.** Phase vs. frequency for a five element delay line of the Photonic TTD system.

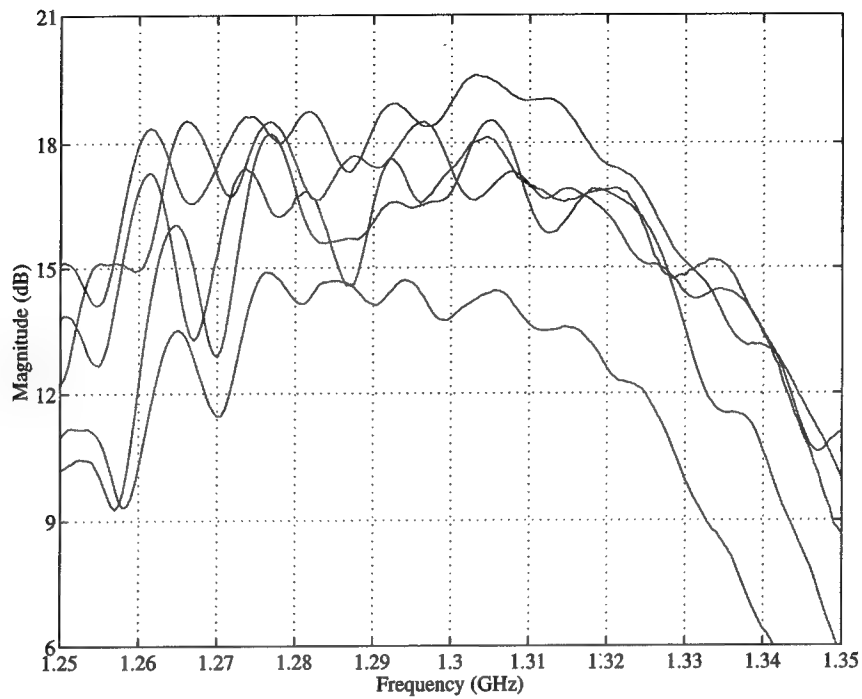


**Figure 41.** Magnitude vs. frequency for a five element delay line of the Photonic TTD system.

Beam patterns for the 30 degree case are plotted in Figures 42, 43, and 44 at frequencies 1.25, 1.275, and 1.3 GHz respectively. Recall that the amount of deviation in angle from the desired steer angle of thirty degrees to the actual main lobe position at the specified frequency is the beam squint.

Figure 42 shows the beam pattern for 1.25 GHz. The Photonic TTD beamformer steers the main lobe to 31.64 degrees causing 1.64 degrees of beam squint. The simulated perfect phase shifter steers the main lobe to 31.29 degrees causing 1.29 degrees of beam squint.

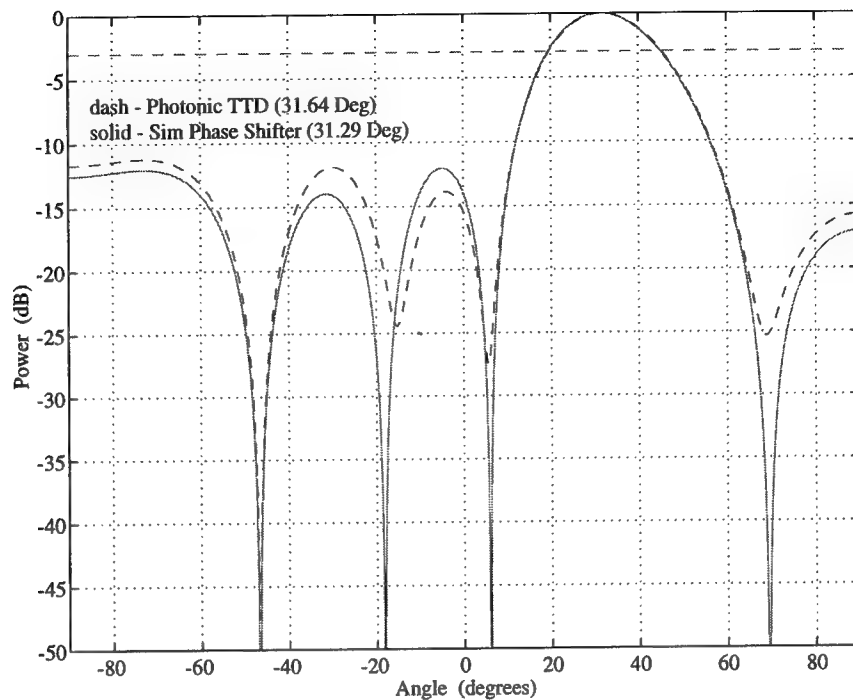


**Figure 42.** Beam patterns at 1.25 GHz of the Photonic TTD system and the perfect phase shifter.

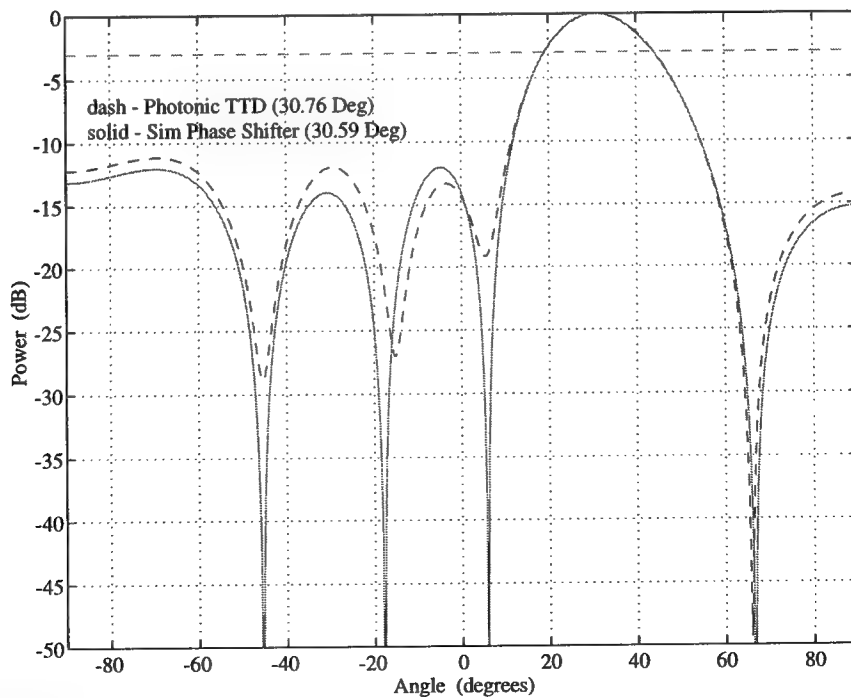


**Figure 43.** Beam patterns at 1.275 GHz of the Photonic TTD system and the perfect phase shifter.

Figure 43 shows the beam pattern for 1.275 GHz. The Photonic TTD beamformer steers the main lobe to 30.76 degrees causing 0.76 degrees of beam squint. The simulated perfect phase shifter steers the main lobe to 30.59 degrees causing 0.59 degrees of beam squint.

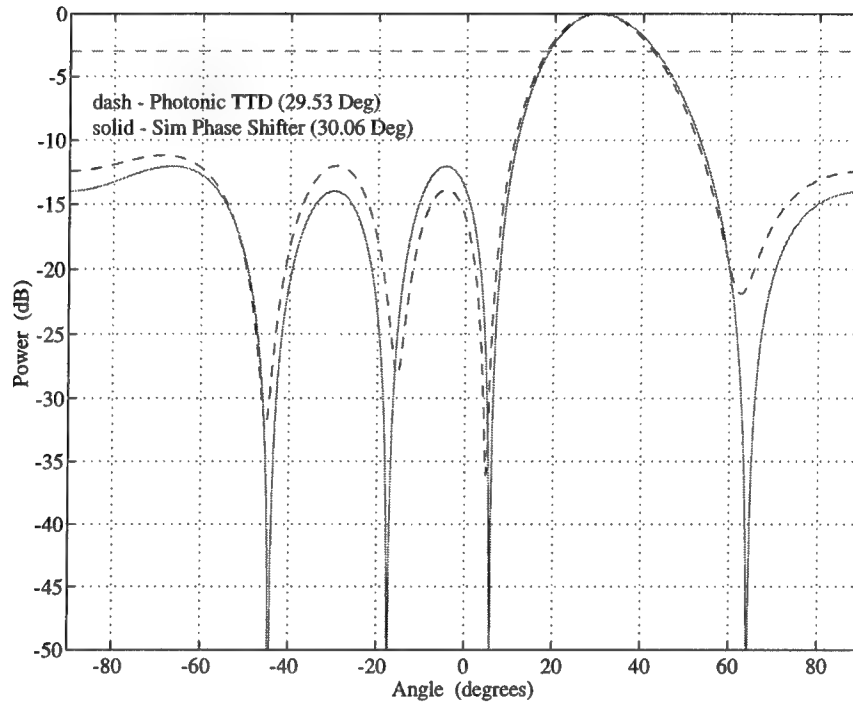


**Figure 44.** Beam patterns at 1.3 GHz of the Photonic TTD system and the perfect phase shifter.

Figure 44 shows the beam pattern for 1.3 GHz. The Photonic TTD beamformer steers the main lobe to 29.53 degrees causing 0.47 degrees of beam squint. The simulated perfect phase shifter steers the main lobe to 30.06 degrees causing 0.06 degrees of beam squint. The simulated perfect phase shifter should have not been afflicted by beam squint at 1.3 GHz, the design frequency. Error due to finite sampling before performing the FFT is the cause for the reported beam squint.

**5.3.3.3 Five Element Array Steered to 60 Degrees:** Figures 46 and 47 show the phases vs. frequency and magnitudes vs. frequency respectively for a five element line array steered to 60 degrees. When comparing Figures 45 and 46, the ideal and measured

TTD phase vs. frequency data, again keep in mind that only the relative phases between the channels and not the absolute phases are important.

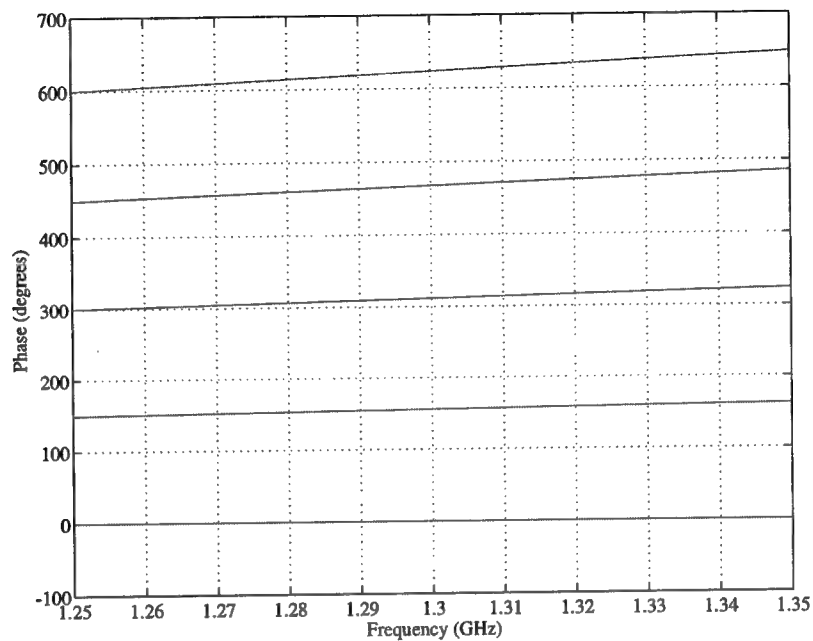


**Figure 45.** Phase vs. frequency for a five element delay line of an ideal TTD system.

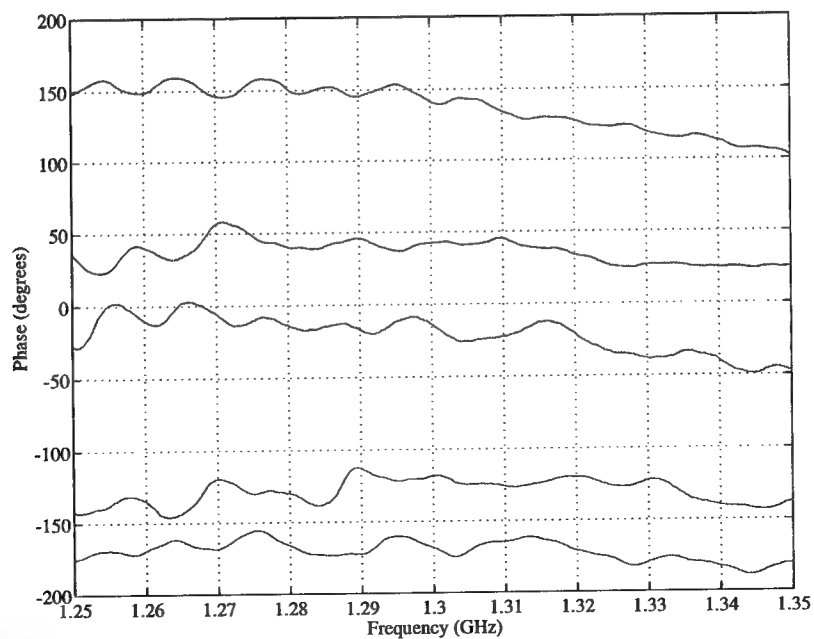


**Figure 46.** Phase vs. frequency for a five element delay line of the Photonic TTD system.

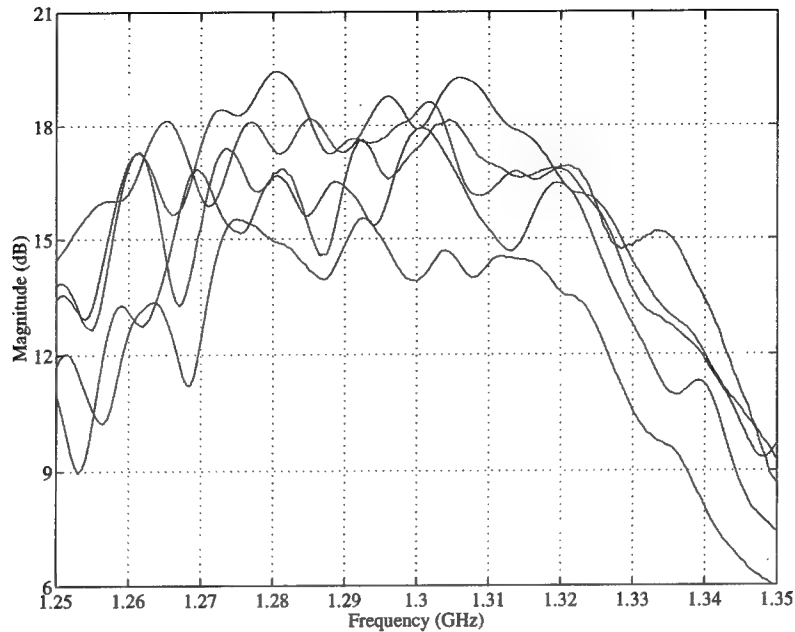
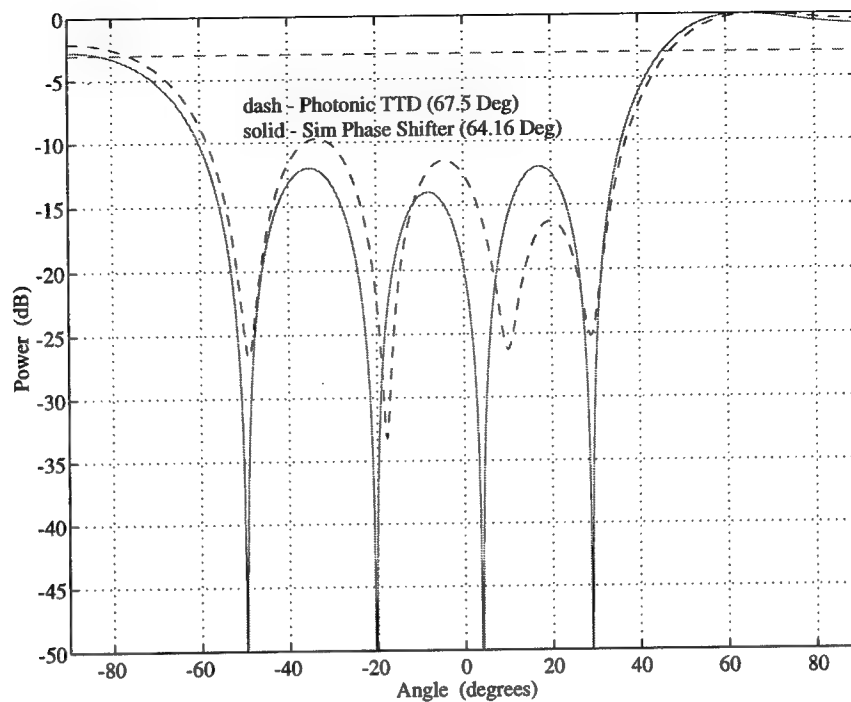


**Figure 47.** Magnitude vs. frequency for a five element delay line of the Photonic TTD system.

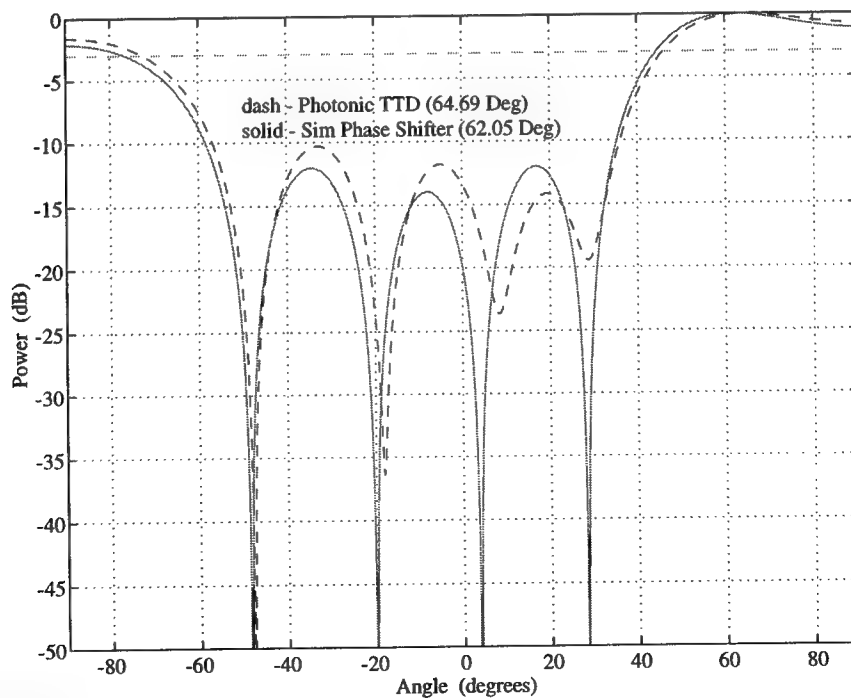
Beam patterns for the 60 degree case are plotted in Figures 48, 49, and 50 or frequencies 1.25, 1.275, and 1.3 GHz respectively. Recall that the amount of deviation in angle from the desired steer angle of sixty degrees to the actual main lobe position at the specified frequency is the beam squint.

Figure 48 shows the beam pattern for 1.25 GHz. The Photonic TTD beamformer steers the main lobe to 67.5 degrees causing 7.5 degrees of beam squint. The simulated perfect phase shifter steers the main lobe to 64.16 degrees causing 4.16 degrees of beam squint.

Figure 49 shows the beam pattern for 1.275 GHz. The Photonic TTD beamformer steers the main lobe to 64.69 degrees causing 4.69 degrees of beam squint. The simulated perfect phase shifter steers the main lobe to 62.05 degrees causing 2.05 degrees of beam squint.



**Figure 48.** Beam patterns at 1.25 GHz of the Photonic TTD system and the perfect phase shifter.



**Figure 49.** Beam patterns at 1.275 GHz of the Photonic TTD system and the perfect phase shifter.

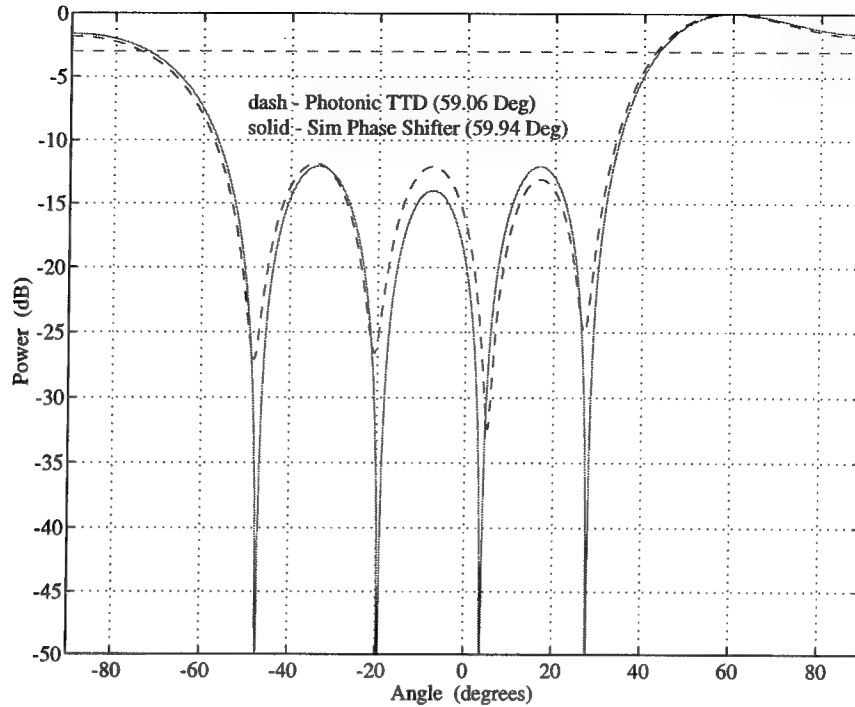


**Figure 50.** Beam patterns at 1.3 GHz of the Photonic TTD system and the perfect phase shifter.

Figure 50 shows the beam pattern for 1.3 GHz. The Photonic TTD beamformer steers the main lobe to 59.06 degrees causing 0.94 degrees of beam squint. The simulated perfect phase shifter steers the main lobe to 59.94 degrees causing 0.06 degrees of beam squint. The simulated perfect phase shifter should have not been afflicted by beam squint at 1.3 GHz the design frequency. Error due to finite sampling before performing the FFT is the cause for the reported beam squint.

**5.3.4 Summary of the Performance with Respect to Beam Squint:** Table 1 summarizes the performance of the photonic TTD beamformer and that of a perfect phase shifter with respect to beam squint. The beam squint suffered by each of the two systems are given for the frequencies 1.25, 1.275, and 1.3 GHz at steer angles of 0, 30, and 60 degrees.

Table 1 shows that a perfect phase shifter suffers less beam squint than the Photonic TTD beamformer. In fact, the perfect phase shifter exhibits beam squint less than or equal to that of the Photonic TTD beamformer in each case. This beam squint can be directly traced to



phase deviation. Figure 29, as well as all the other phase vs. frequency plots, are illustrative of this problem. As stated previously, imperfections in the optical surfaces contribute to the phase deviations. Over 20 separate optical surfaces make up the integrated system. Each of these surfaces has the potential to degrade the system performance with respect to phase. The additive effects from all the surfaces produce phase deviation ranging from  $\pm 9$  degrees over the operational bandwidth.

**Table 1.** Beam squint of the Photonic TTD system and the perfect phase shifter for the frequencies 1.25, 1.275, and 1.3 GHz at steer angles of 0, 30, and 60 degrees.

	1.25 GHz	1.275 GHz	1.3 GHz
	<b>0 degrees</b>		
<b>Photonic TTD</b>	0.00°	0.00°	0.35°
<b>Phase Shifter</b>	0.00°	0.00°	0.00°
	<b>30 degrees</b>		
<b>Photonic TTD</b>	1.64°	0.76°	0.53°
<b>Phase Shifter</b>	1.29°	0.59°	0.06°
	<b>60 degrees</b>		
<b>Photonic TTD</b>	7.50°	4.69°	0.94°
<b>Phase Shifter</b>	4.16°	2.05°	0.06°

The concept of the TTD line is that a proper and precise linear relationship between phase and frequency be generated. Tight control of phase is required to achieve the advantages of the TTD line in reducing/eliminating beam squint. The photonic TTD system developed does not meet this requirement and thus the beam squint problem is still unsolved.

**5.3.5 Phase Drift:** As previously mentioned phase drift afflicts the Photonic TTD beamformer. Each channel drifts rather quickly—approximately one half degree per second (See Figure 51). Vibrations caused by the heating and air conditioning systems in the lab and other vibration sources are likely culprits. Unstable temperature gradients on the surface of the optical table due to poor thermal control in the entire laboratory also contributes. Inter-channel drift, or the difference between how two channels drift with respect to one another over time, is shown in Figure 52. The measured inter-channel drift is considered to be negligible, meaning that the two measured channels drift together.

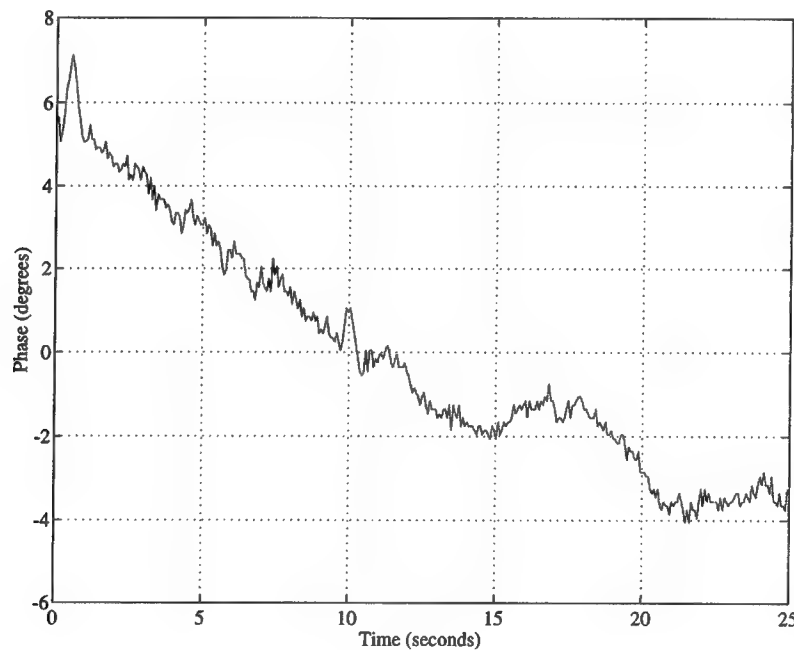


**Figure 51.** Typical phase drift of a single channel vs. network analyzer reference signal.

The consequence of phase drift is a massively increased requirement for feedback. To compensate for drift, the system must continually update the positions of all twenty DMD mirror segments. The feedback sub-system as designed falls short of this requirement. The designed feedback sub-system measures only a single channel at a time. It sequences through the channels by opening the shutter associated with the channel of interest and closing the rest. The current system can't cycle through the channels quickly enough to provide required feedback and control in a timely manner.

The lack of inter-channel drift may lead the reader to believe a single channel feedback system as currently designed is possible. However, the hysteresis associated with the DMD nullifies this hope. Due to hysteresis, it takes several updates per mirror actuator to position each DMD segment properly. The feedback and mirror control sub-systems must outpace the phase drift to be of any utility. Simultaneous feedback on all twenty channels is required.

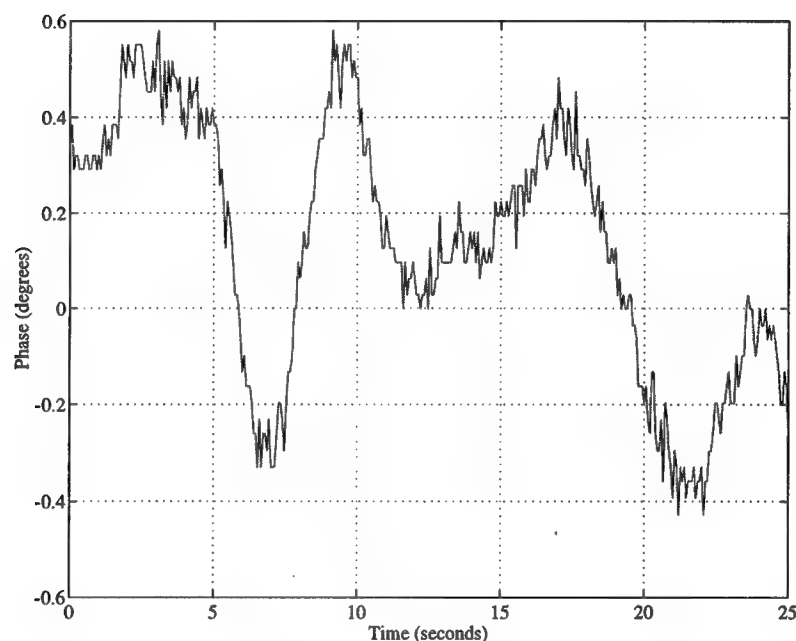


**Figure 52.** Inter channel phase drift.

**5.3.6 Performance of the Integrated System vs. a Free Space Predecessor:** In 1992, Toughlian & Zmuda constructed a free space system which implemented the same basic optical heterodyning concept for generating TTD as this integrated system uses. In fact, the motivation for constructing the integrated system was to overcome some of the observed problems with the free space system. The integrated system minimizes susceptibility to vibration and air currents—long considered the Achilles heel for a free space system. Figures 53 and 54 illustrate the gains in performance which have been realized by going from free space to the integrated system. The free space system operates at a design frequency of 67.5 MHz and has a 25 MHz bandwidth, while the integrated system operates at a design frequency of 1.3 GHz and has 60 MHz bandwidth.

The free space system displays massive phase deviation as compared to the integrated system. Obviously, mounting the system on a fixed invar plate and piping the light through glass to the maximum extent practical has paid dividends in terms of the system phase performance.

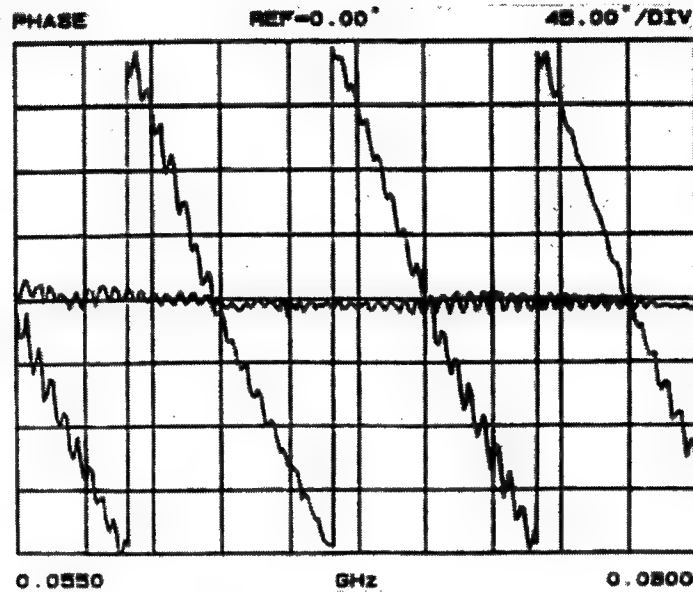


**Figure 53.** Phase vs. frequency for a single channel of the free space system.

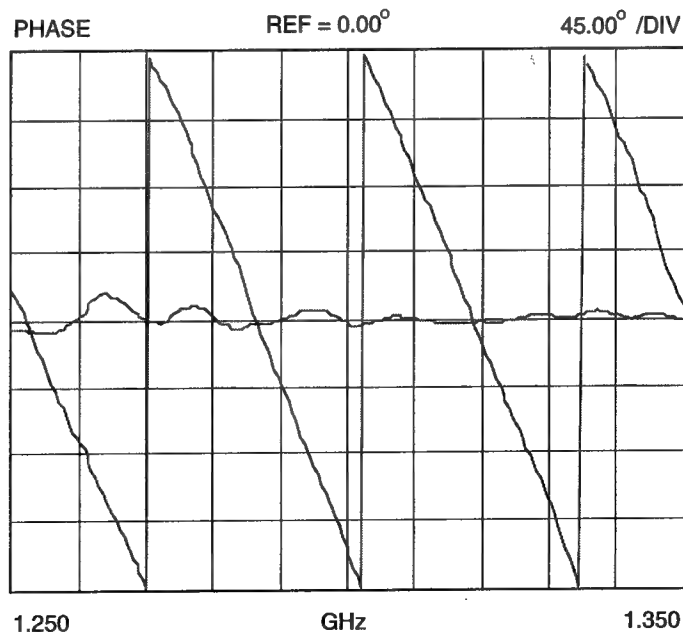


**Figure 54.** Phase vs. frequency for a single channel of the integrated system.

## 6.0 Discussions and Conclusions

Before discussing the results and drawing any conclusions, some basic background is revisited to put the current information in context.

Current state-of-the-art phased array radars implement electronic phase shifters for beamforming. The limitation of the phase shifters becomes apparent if multiple frequencies are transmitted simultaneously. The energy associated with the different frequencies will point in different directions in the antenna's far field causing an increase in beam width. This phenomena, called squint, restricts the phase shift approach to narrowband operation.

Replacing the phase shifter with a set of variable delay lines overcomes the limitation of narrow band operation, and facilitates wide bandwidth operation. A variable delay line system sends properly phased signals with respect to frequency to each of the individual antenna elements. These systems are not afflicted with beam squint. To date, attempts to achieve variable delay line performance have focused mainly on constrained feed systems where different lengths of optical fiber or electrical cable are switched in and out to achieve the proper delay. Constrained feed systems are bulky and inefficient.

This body of work attempts to exploit the spatial processing advantages of photonics for realizing a continuously variable RF delay in a small, efficient package. The photonic concept for generating time delays is based on optical heterodyning. An acousto-optic (AO) cell modulates a laser light carrier with a RF transmit signal. A tiltable mirror selects an appropriately time delayed version of the modulated beam. The signal (or modulated beam) and reference light beam heterodyne, resulting in a properly delayed RF signal for feeding an antenna element.

The current project 4600P210 is a continuation of work started in a previous effort (4600P204). The concepts, theoretical development, and design of the photonic TTD beamformer were completed under effort 4600P204. Project 4600P210 encompasses the development, construction, testing, and evaluation of a breadboard for photonically controlling a 20 element, wide bandwidth (200 MHz) L-Band phased array radar. The culmination of this project was envisioned to be a joint field test of the Rome Laboratory Photonic TTD beamformer and a twenty element L-Band Antenna built by Lockheed Martin.

Like any research and development effort, this one had its share of successes and shortcomings.

The integrated system reported on here is a second generation system. In 1992, Toughlian & Zmuda constructed a free space system which implemented the same basic optical heterodyning concept. The free space system exhibited significant phase deviation away from the desired linear relationship between phase and frequency. Susceptibility to vibration and air currents—often the Achilles heel of any free space system—drove the design of this next generation toward glass enclosure. The integrated system maximizes the use of glass to the extent practical. The motivation for constructing the integrated system was to overcome the observed problems with the free space system. Experimental results confirmed that integrated system indeed minimizes susceptibility to vibration and air currents. Figures 53 and 54 illustrate the gains in performance which have been realized by enclosing the system in glass. The free space system displays massive phase deviation as compared to the integrated system. The integrated systems grossly outperforms the free space system.

As previously stated, the critical function of the TTD line is the establishment of a proper and precise linear relationship between phase and frequency. Tight control of phase is required to achieve the advantages of the TTD line in reducing/eliminating beam squint. Recall that any deviation from the desired linear relationship between phase and frequency causes beam squint.

The Photonic TTD system exhibits an imperfect (non-linear) phase vs. frequency relationship. Figure 29 in the Experimental Results section illustrates the phase vs. frequency of a typical channel for the antenna steered to broadside (0 degrees). Measured phase deviations ranging from  $\pm 9$  degrees over the operational bandwidth infringes upon the system requirement to tightly control the phase vs. frequency relationship.

Imperfections in the system's optical surfaces contribute to the phase deviations. Over 20 separate optical surfaces make up the integrated system. Each of these surfaces has the potential to degrade the system performance with respect to phase. The additive effects from all the surfaces produce the net effect.

Ultimately, the Photonic TTD beamformer fell short of solving the beam squint problem that it was designed to overcome. The phase shifter that the Photonic TTD beamformer was

designed to replace outperformed the photonic system with respect to beam squint. Table 1 in the Experimental Results section summarizes beam squint performance of both systems. Note, that a comparison was made to a perfect phase shifter (i.e. one that applies the same phase shift to all frequencies). In reality, phase shifters do not in fact display such perfect performance. Phase shift varies over the operational bandwidth of a real phase shifter. The comparison made here represents the worst case scenario.

In addition to phase deviation, phase drift beset the Photonic TTD beamformer. Each of the twenty channels drifts rather quickly; approximately a half a degree per second. Vibrations caused by the heating and air conditioning systems in the lab and other vibration sources are likely culprits. Unstable temperature gradients on the surface of the optical table due to poor thermal control in the entire laboratory also contributes. Inter-channel drift or the difference between how two channels drift with respect to one another was measured. The amount of inter-channel drift is considered to be negligible.

The consequence of phase drift is an increased requirement for feedback. To compensate for drift, the system must continually update the positions of all twenty DMD mirror segments. The feedback sub-system as designed falls short of this requirement. The designed feedback sub-system measures only a single channel at a time. It sequences through the channels by opening the shutter associated with the channel of interest and closing the rest. The current system can't cycle through the channels quickly enough to abrogate the phase drift. To meet this new requirement a sub-system capable of simultaneous feedback on all twenty channels is required. Additionally, the feedback and mirror control sub-systems must outpace the phase drift.

Ignoring phase drift, the computer controlled twenty element DMD successfully selected independent time delayed versions of the desired transmit signal as theorized. Mirror jitter, considered a potential problem, turned out to be insignificant. The DMD demonstrated hysteresis as expected—note that the hysteresis was a function of the design & construction of the DMD, and not a result of our control system. For our experiments, the hysteresis was not a factor, but would be in an operational system. The mirror manufacturer, Thermotrex Inc., manufactures an upgraded product, which reduces the hysteresis from 15% to 1%.

In summary, the integrated system demonstrated a leap in performance over its free space predecessor. Shortcomings in its performance, specifically with respect to phase vs.

frequency, are attributed to imperfections in the system's optical surfaces (over twenty). Most of the optical components used were acquired from off-the-shelf stock. We applied this methodology to keep costs manageable. Replacing these off the shelf components with specialized items that maintain stringent phase requirements could potentially make the system viable.



## **7.0 Recommendations & Future Work**

Due to the phase deviation and phase drift problems associated with the Photonic TTD beamformer, Rome Lab and Lockheed Martin have canceled plans to conduct a joint field test.

Rome Laboratory continues to pursue multiple in-house and contractual activities in the optical beamforming area.

## 8.0 References

1. R. Mailloux, "Phased Array Antenna Handbook", Artech House, Massachusetts, 1994.
2. W.L. Stutzman, G.A. Thiele, "Antenna Theory and Design", John Wiley and Sons, 1981.
3. A. Oliner, G.Knittel, "Phased Array Antennas", Artech House, Massachusetts, 1972.
4. A. Korpel, "Acousto-Optics - A Review of Fundamentals", *Proceedings of the IEEE*, Vol. 69, No. 1, Jan. 1981.
5. A. VanderLugt, "Optical Signal Processing", Wiley Interscience, 1992.
6. E. N. Toughlian, H. Zmuda, P. Kornreich, "A Deformable Mirror-Based Optical Beamforming System for Phased Array Antennas", *IEEE Photonics Technology Letters*, Vol. 2, No. 6, June 1990.
7. J.R. Leger, G.J. Swanson, and W.B. Veldkamp, "Coherent Laser Addition using Binary Phase Gratings", *Applied Optics*, Vol. 26, no. 20, pp. 4391-4399, 15 Oct. 1987.
8. H. Zmuda and E. N. Toughlian, "Adaptive Microwave Signal Processing: A Photonic Solution", *Microwave Journal*, Feb. 1992.
9. A. Papoulis, "The Fourier Integral and its Applications", New York: McGraw-Hill Book Co., 1962.
10. E. N. Toughlian and H. Zmuda, "Broadband Photonic Signal Processing for Microwave Applications", *DOD Fiber Optics Conference '92*, March, McLean, Virginia.
11. T. Day and E.K. Gustafson, and R.L. Byer, "Active Frequency Stabilization of a 1.062 mm, Nd:YAG, Diode-Laser-Pumped Non-Planar Ring Oscillator to Less Than 3 Hz of Relative Linewidth", *Optics Letters*, 15, 221-223 (1990)
12. Simonis, G.J. and K.G. Purchase, "Optical Generation, Distribution, and Control of Microwaves using Laser Heterodyne", *IEEE Transactions on Microwave Theory and Techniques*, Vol. 38, No. 5, pp. 667-669, May 1990.
13. L.J. Hornbeck, "Deformable-Mirror Spatial Light Modulators", *Proceedings of SPIE*, vol. 1150-06, August, 1989.

14. Boysel, R.M., J.M. Florence, and W.R. Wu, "Deformable Mirror Light Modulators for Image Processing," *SPIE Proceedings*, Vol. 1151, pp. 183-194, Aug. 1989.
15. B. Hulburd and D. Sandler, "Segmented Mirrors for Atmospheric Compensation", *Optical Engineering*, vol.29, No.10, Oct.1990, pp. 1186-1190.
16. G.A. Melnik, "A Fixed Format Liquid Crystal Device for Spatial Optical Phase Control", Optron Systems Inc, internal document, Bedford, Massachusetts.
17. J.C. Palais, "Fiber Optic Communications", Prentice-Hall, New Jersey, 1984.
18. Harris Corporation, "Pre-sort Processor", Technical Report RL-TR-88-247, 1988.
19. M. King, et al, 'Real-Time Electrooptical Signal Processors with Coherent Detection', SPIE Vol MS 16, pg 357.
20. K. Baldwin, "Computer Aided Design and Simulation of an Integrated Photonic Delay Line System for Phased Array Antenna and Other Microwave Signal Processing Applications", Rochester Institute of Technology, 1993.
21. G. J. Swanson, "Binary Optics Technology: The Theory and Design of Multi-Level Diffractive Optical Elements", Lincoln Laboratory, 1989.
22. Thermo Electron Technologies Corp., "Maintenance Information 20 Segment Mirror for Phased Array Antenna", TTC-2210-N, June 12, 1991.

## **Appendix A:**

# **Design Details of the Spatially Integrated True Time Delay System**

---

### **A-1 Integrated Optical System**

#### **A-1.1 Introduction**

The integrated optical system has been designed to control a 20 element phased array antenna for radar applications, which was built by Lockheed Martin under a Co-operative Research and Development Agreement (CRDA). It is composed of three major subsystems for which the theories of operation have already been described. The first system, "front end," performs optical heterodyning. The second replicates the output of the front end into 25 channels, of which 20 are used, and collimates the 20 individual beams or channels. The third extracts the properly delayed signal for each channel.

The front end breaks the input beam from the laser into a reference and a local oscillator (signal) beam. An RF signal is impressed onto an optical carrier, the local oscillator, via an acousto-optic cell. The AO cell provides a continuum of available time delays. The two beams recombine for heterodyne detection. The output of this portion of the system contains the information required for generation of a single delay line.

The second subsystem replicates the output from the front end into 25 identical beams by the use of a binary optic. Each beam possesses the TTD information required to feed one antenna element. The optical system collimates the individual beams with respect to one another, and each individual delay line is brought to a focus. An array of microlenses then collimates each of the 20 individual delay line beams.

The third subsystem extracts the proper TTD for each antenna element by tapping various locations on the AO cell through the use of a deformable mirror device (DMD.) This is exactly analogous to the function of the DMD in the single photonic delay line system, except that the DMD now represents a two dimensional array of deformable mirrors, one

for each delay line to be utilized. Since each mirror is independently accessible, each delay line is capable of providing a TTD independent of TTDs tapped by other DMD segments.

This Appendix contains information in the form of specifications, mechanical drawings, etc. for the integrated system . Specifications for all major subsystems and components are included.

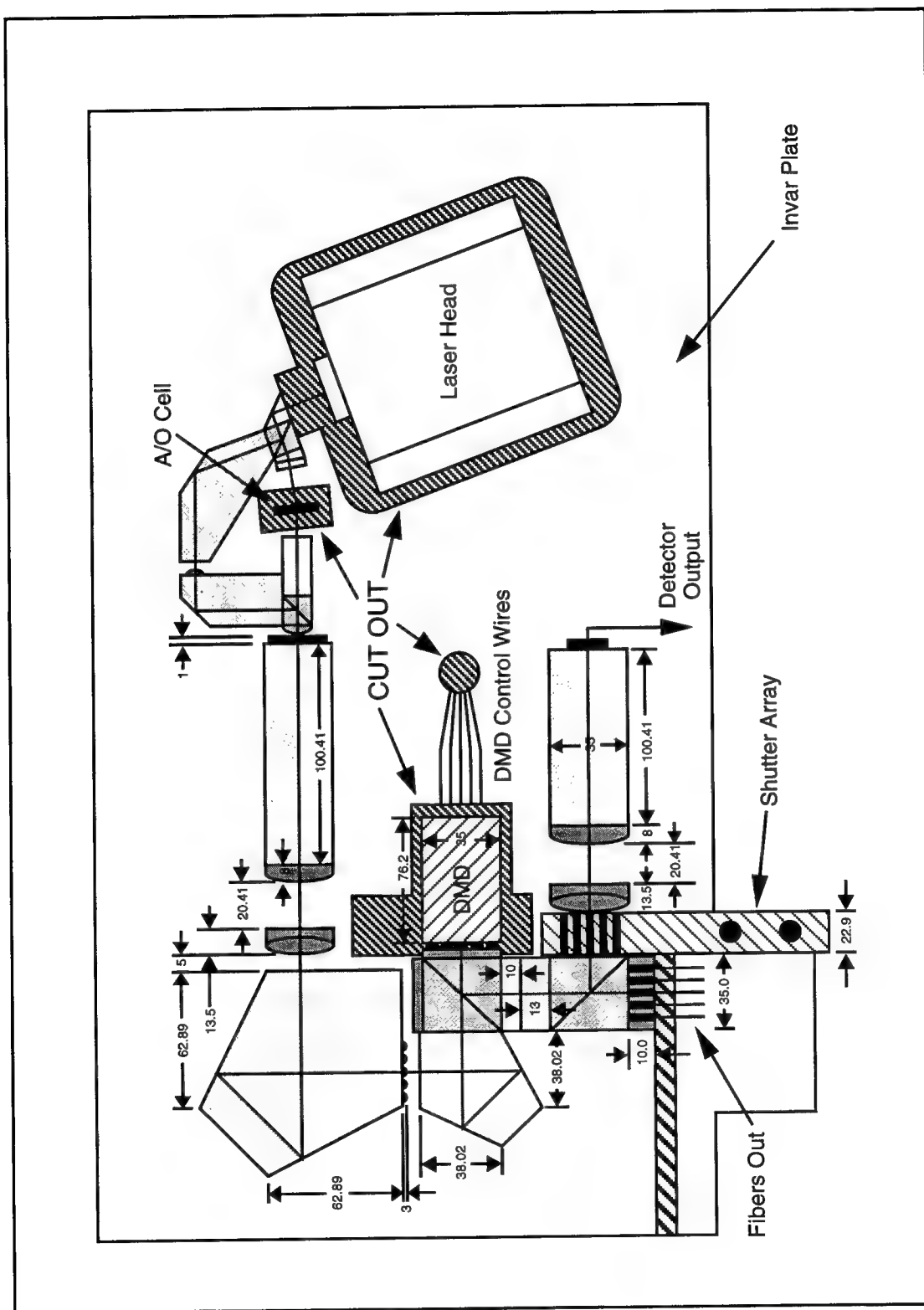
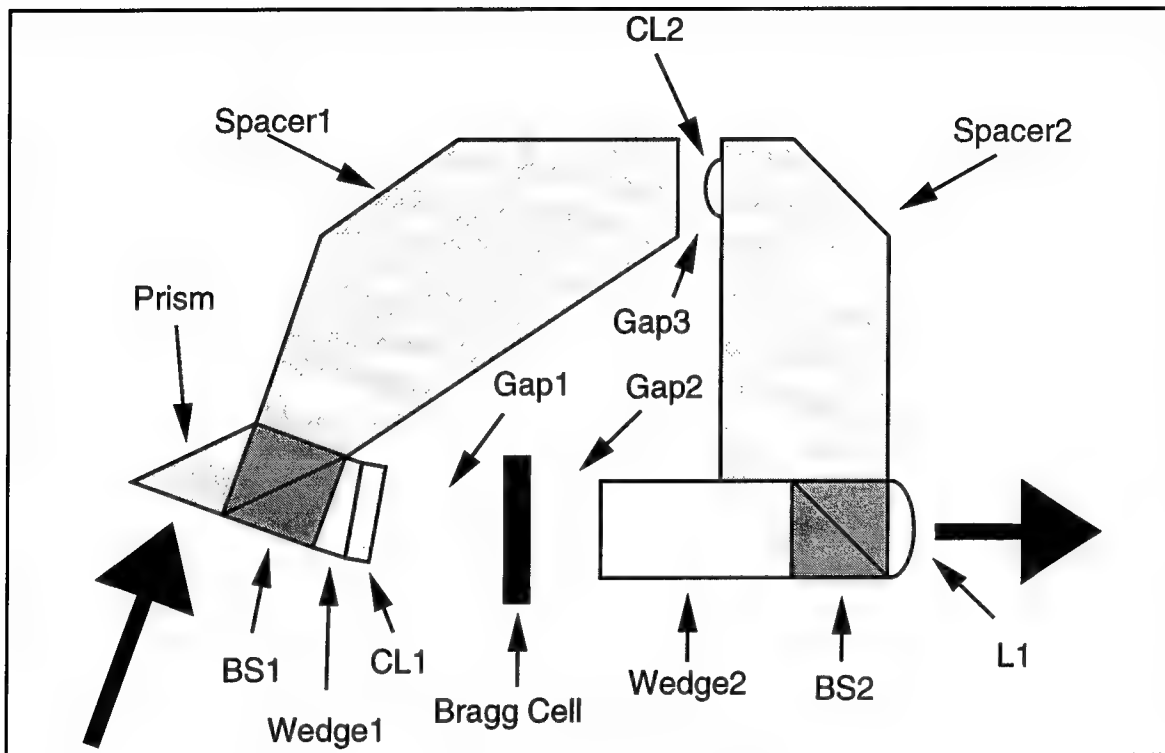
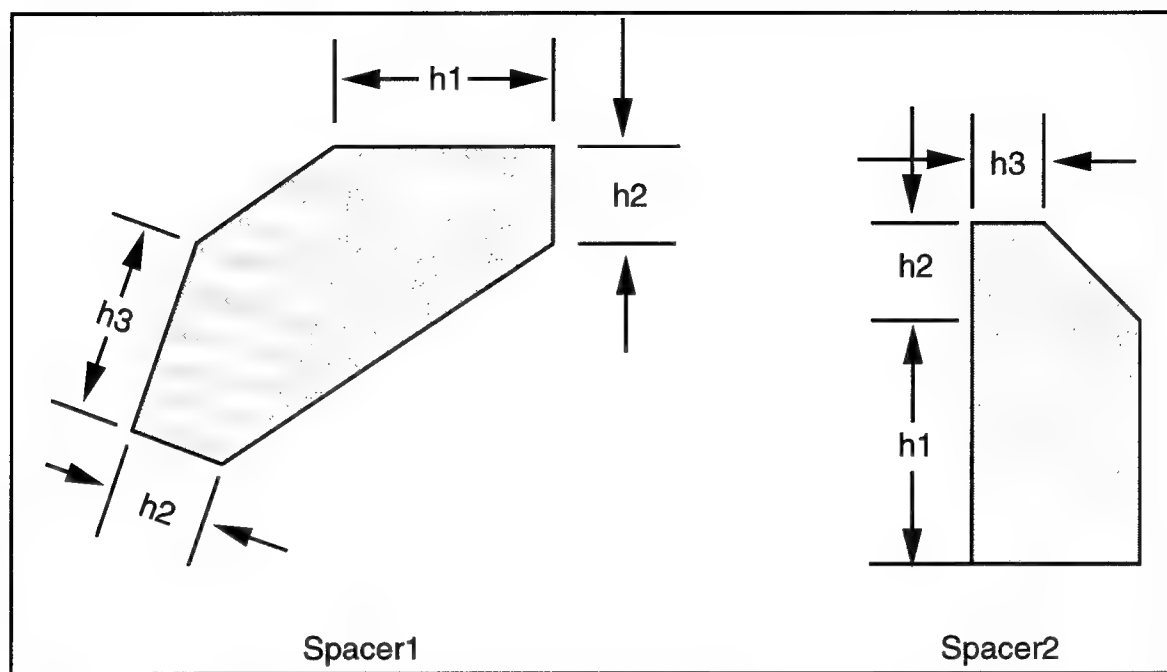


Figure A-1. Mechanical Drawing of Optical Breadboard Design.

## A-1.2 Subsystem 1: Front End



**Figure A-2.** Front End



**Figure A-3.** Schematic of Glass Spacers in Front End



**Table A1.** Specifications of Front End Components [20]

<b>Component Name</b>	<b>Component Type</b>	<b>Thickness in mm</b>	<b>Index of Refraction</b>	<b>ROC in mm</b>
BS1	Beam Splitter	12.7	1.50348	--
Wedge1	Wedge	3	1.50348	--
CL1	Cylindrical Lens	5	1.50348	6.58749
Gap1	Air Gap	12.335413	1.00000	--
Bragg Cell	--	5	3.34	--
Gap2	Air Gap	7.131780220	1.00000	--
Wedge2	Wedge	26.54975	1.50348	--
BS2	Beam Splitter	12.7	1.50348	--
L1	Spherical Lens	3.6	1.50348	18.67320
CL2	Spherical Lens	2.5	1.50348	8.24184
Gap3	Air Gap	4.2	1.00000	--
Spacer1 - h1	Spacer	36.21338	1.50348	--
Spacer1 - h2	Spacer	12.7	1.50348	--
Spacer1 - h3	Spacer	18.37024	1.50348	--
Spacer2 - h1	Spacer	26.10	1.50348	--
Spacer2 - h2	Spacer	12.7	1.50348	--
Spacer2 - h3	Spacer	10.474	1.50348	--

### A-1.3 Subsystem 2: TTD Beam Replicating and Collimating Subsystem

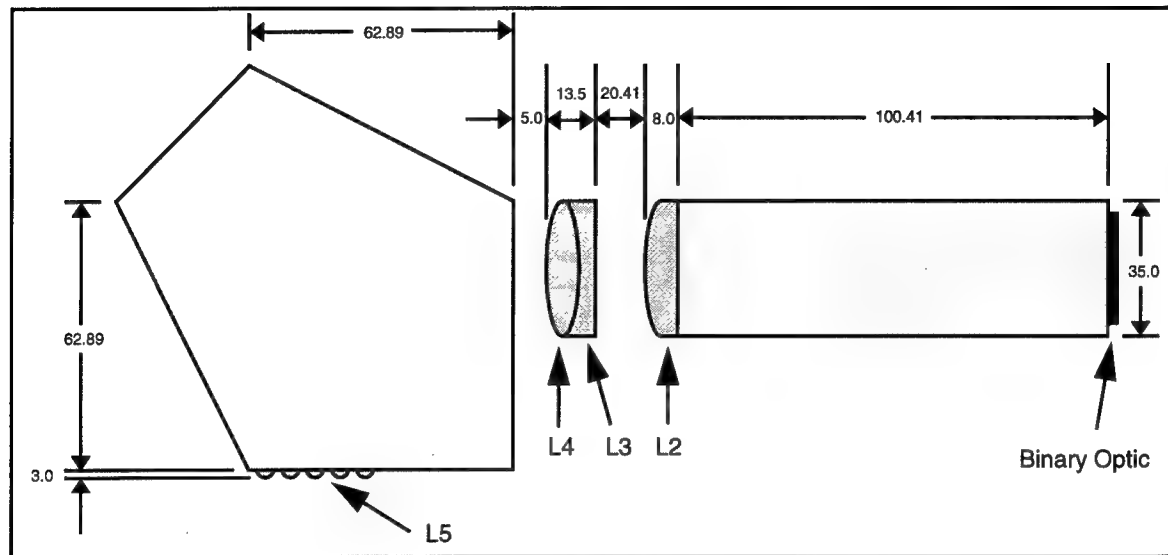


**Figure A-4.** TTD Replication and Collimating Optical Subsystem

**Table A-2.** Specification of TTD Beam Replicating and Collimating Subsystem [20]

Component Name	Component Type	Index of Refraction	ROC in mm
L2	Spherical Lens	1.50348	65.87743
L3	Spherical Lens	1.64653	-341.67405
L4 First Surface	Spherical Lens	1.54944	-80.98038
L4 Second Surface	Spherical Lens	1.54944	120.35830
L5	Spherical Micro-Lens	1.50348	45.76

### A-1.4 Subsystem 3: TTD Selection and Feedback Subsystem

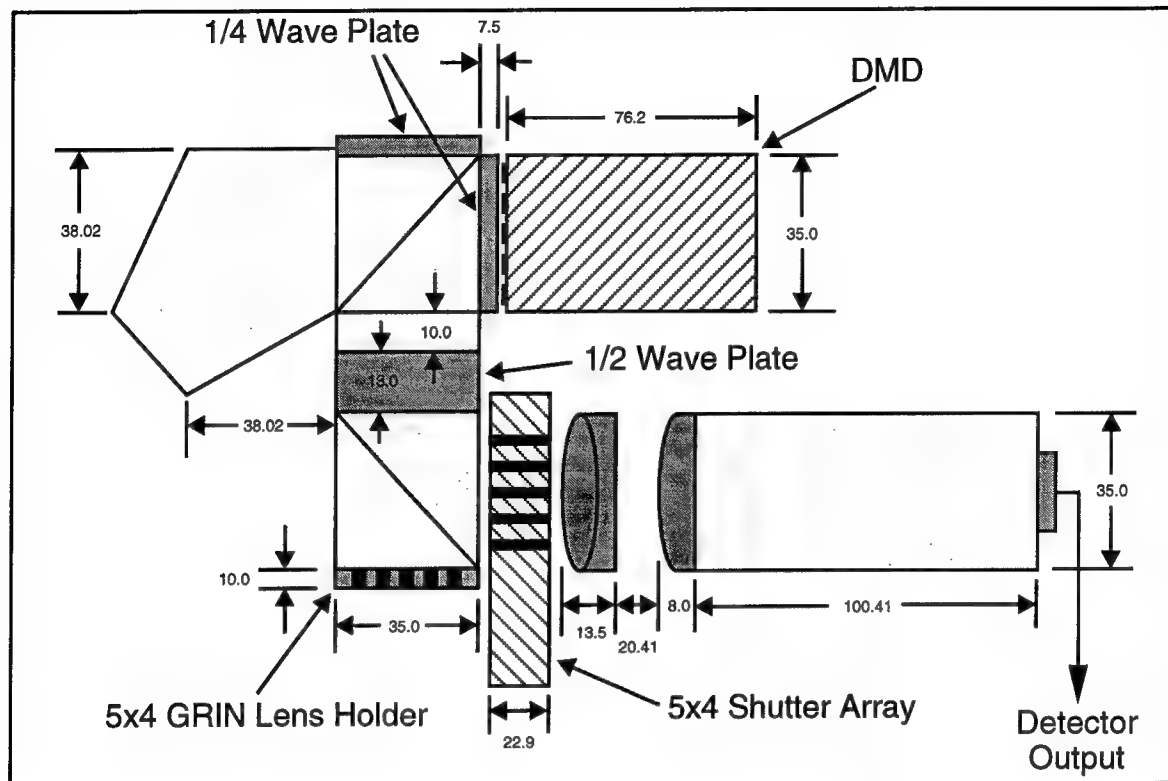


**Figure A-5.** TTD Selection and Feedback Subsystem

## A-2 Active Components

### A-2.1 Laser: 122-1319-150-F Lightwave Electronics<sup>1</sup>

Laser Gain Medium	Nd:YAG
Wavelength	1319 nm
Output Power	150 mW
Typical Beam Characteristics	
Waist Location	50±2mm Behind Aperture
Diameter at Aperture (1/e <sup>2</sup> )	
Vertical	0.5 mm
Horizontal	0.5 mm
Divergence Full Angle(1/e <sup>2</sup> )	
Vertical	8 mrad
Horizontal	10 mrad
Polarization Ratio	Vertical @ >1000:1
Spatial Mode	Diffraction Limited TEM <sub>00</sub>
Power Stability	
Amplitude Noise	≤0.1%rms
Power Drift	≤±2%
Frequency Stability	
Line width	≤5 kHz/msec
Jitter	≤75 kHz/msec
Drift	
At Constant Temperature	≤50 MHz/hour
With Temperature Change	<150 Mhz/°C
Broad Frequency Tuning	
Total Frequency Scanning Range	≥30 GHz
Continuous Scanning Range	≥12 GHz
Frequency Scanning Rate	≥1 GHz/sec
Maximum Input Voltage	±50 V
Fast Frequency Tuning Option (-F)	
Piezoelectric Tuning Coefficient	≥2 MHz/V
Response Bandwidth	>100 kHz
Maximum Voltage	±15 V
Utility Requirements	
Voltage	85 V to 265 V
Frequency	50 Hz to 400 Hz
Power (typical)	approximately 25 W

Environmental Requirements	
Operating Temperature Range	10°C to 35°C
Relative Humidity	10% to 90%
Weight	
Laser Head	1.1 kg
Power Supply	3.4 kg

## A 2.2 Acousto-Optic Cell: IPF-130-40 Brimrose<sup>1</sup>

Medium	Indium Phosphide (InP)
Optical Wavelength Range	1000 nm to 1600 nm
Bragg Angle at 1300 nm	9.5 degrees
Index of Refraction	3.34 @ 1300 nm
Acoustic Beam Height	75µm
Data at Laser Wavelength	1150 nm
Optical Transmission	90%
Maximum Diffraction Efficiency	26%
Active Aperture	0.076 mm
Center Frequency	1300 MHz
Bandwidth (3dB)	350 MHz
Acoustic Mode	Longitudinal
Acoustic Velocity	5.1 Km/sec
Maximum RF Input	1 W
VSWR	2:1
Optical Polarization	Linear

## A-2.3 Binary Optic

### A-2.3.1 Background on Multi-Level Diffractive Optics

The binary optic is a multi-layer phase grating designed to generate a specific wavefront output. For our system, the binary optic produces 25 beams—all of equal amplitude—with nearly 100% diffraction efficiency. Diffraction efficiency is determined by the element's surface profile. In theory, surfaces with perfect diffraction efficiency can be produced but practical constraints limit designs to discrete phase profiles. If the discrete phase profile is not a good match to the desired phase grating, diffraction efficiency will suffer. To achieve a better match to the desired phase grating and higher efficiency, many layers of finer discrete steps can be fabricated. When designing a binary optic, a compromise between diffraction efficiency and ease of fabrication must be made. Figure A6 shows a continuous phase grating with 2 and 4 discrete phase levels. It is apparent from the figure that the larger the number of discrete phase levels, the better the approximation to the continuous phase profile. These multilevel phase profiles can be fabricated using standard semiconductor fabrication techniques. [21]

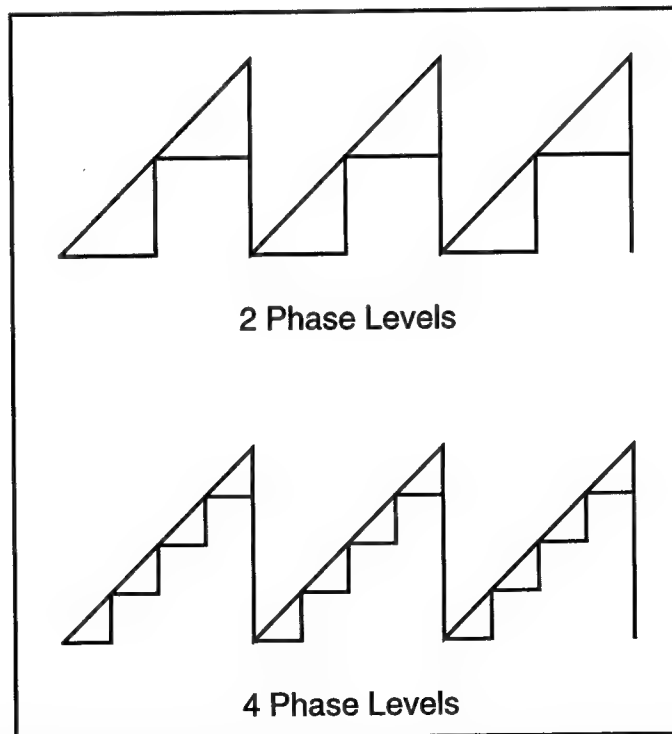


**Figure A-6.** Continuous Phase Grating Compared with 2 and 4 Discrete Phase Levels

Table A-3 lists the diffraction efficiency of a multi-level structure for various values of the number of phase levels.

**Table A-3:** Multi-Level Diffraction Efficiency for Various Numbers of Phase Levels [21]

Number of Levels	First-Order Efficiency
2	0.41
3	0.68
4	0.81
5	0.87
6	0.91
8	0.95
12	0.98
16	0.99

### A-2.3.2 Specifications of the Binary Optic

Number of Elements	32 x 32 Array
Pixel Size	0.5mm x 0.5mm
Period	16 mm
Diffraction Efficiency	73%
Diffraction Angle	9.4 degrees

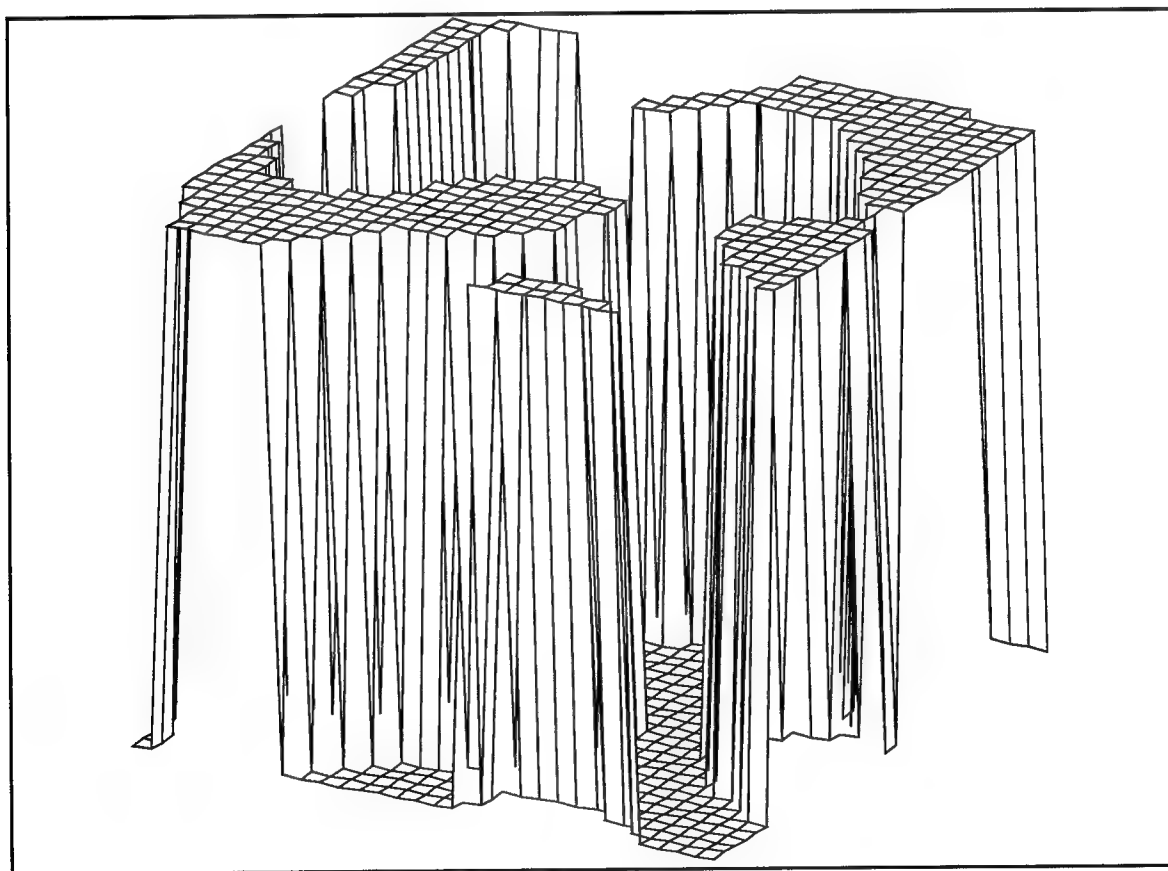


**Figure A-7.** 3 Dimensional View of Single Cycle of the Binary Optic



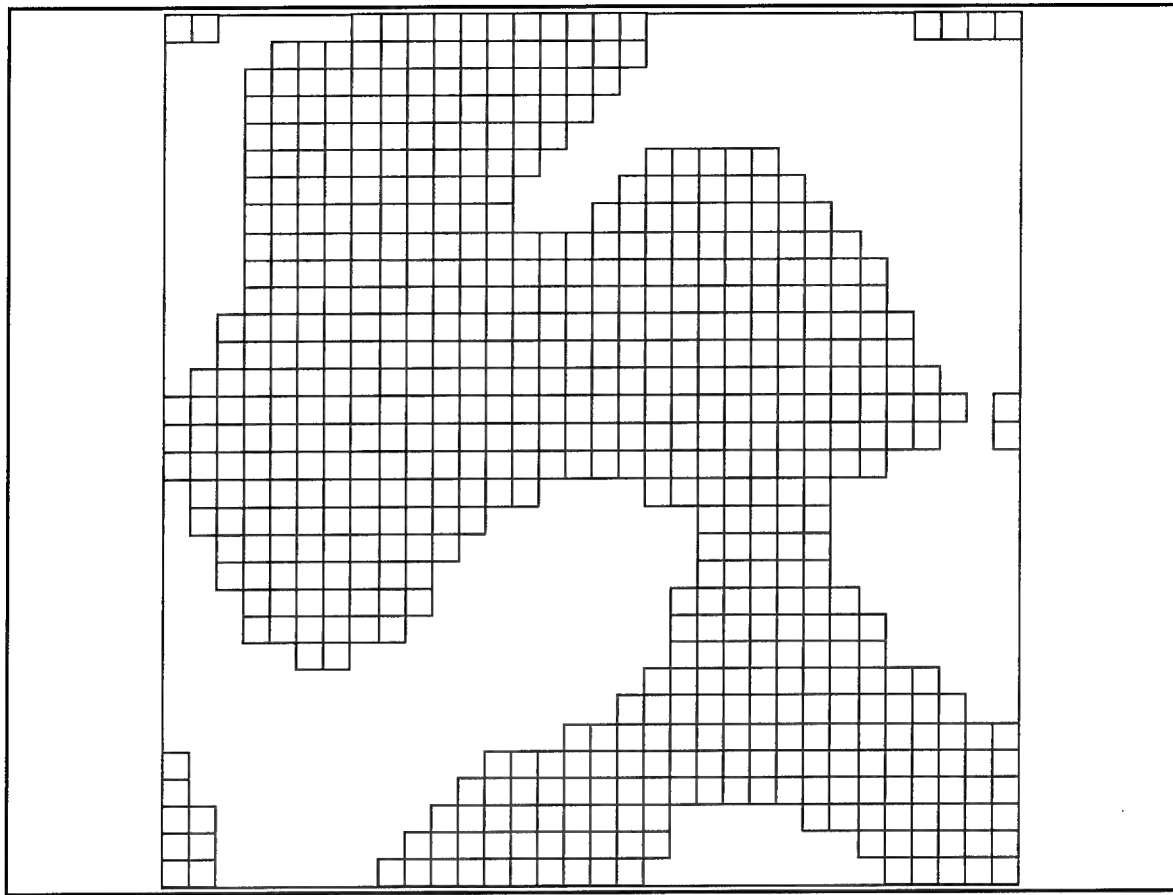


**Figure A-8:**2 Dimensional View of a Single Cycle of the Binary Optic

#### A-2.4 Deformable Mirror Device (DMD): ThermoTrex (formerly Thermo Electron Technologies) <sup>1</sup>

Number of Mirror Segments	20 (5 x 4)
Degrees of Freedom/Mirror	3
Mirror Segment Size	7 mm x 7 mm
Total Actuator Stroke	$\leq 6 \mu\text{m}$
Mirror Flatness	$\leq 2 \mu\text{m}$
Useful Stroke	$\leq 4 \mu\text{m}$
Lowest Actuator Resonance	$\geq 2 \text{ kHz}$
Actuator Drive Voltage	$\pm 225 \text{ V ( max )}$
Mirror Coating	Denton FSS-99
Mirror response Linearity	$< 1\% ^2$
Mirror Actuator Hysteresis	$< 1\% ^2$
Tip/Tilt Bandwidth	$> 2 \text{ kHz} ^2$
Flatness of Response ( DC to 2 kHz )	$< 3 \text{ dB} ^2$
Phase Shift <sup>2</sup>	<div>100 Hz -5 degrees</div> <div>500 Hz -80 degrees</div> <div>1000 Hz -145 degrees</div> <div>2000 Hz -420 degrees</div>
Frequency for 45 Degree Phase Shift	350 Hz <sup>2</sup>

*Note 2:* Test Frequency of 10 Hz with a drive voltage of 300 V<sub>pp</sub> applied to the actuator producing a displacement of approximately 4.5  $\mu\text{m}$ . This specification assumes strain gauge feedback installed. Response down -6 dB at the highest frequency.

The Mirror Control Electronics (MCE) comprise a rack of equipment that is specifically designed by ThermoTrex to control the DMD. The 20 segment DMD is driven by two 32 channel driver boards. Each mirror has three actuators, requiring 1 drive channel/actuator.

Therefore, a total of 60 drive channels are required (leaving two drive output channels on each board unused). The driver boards are controlled by programming the desired output on the VMEbus computer. The gain of each channel is stored in an electrically erasable memory on the driver board and is not lost when power is removed from the board. Ten bit D/A converters are used to drive each of the amplifiers. Each of the 32 amplifiers are capable of outputting voltages between +300 and -300V. An A/D converter allows a read-back of the output voltage setting—to be used by the host computer as necessary to maintain voltage level settings. [22]

## A-2.5 Pigtailed GRIN Lens: BG30 Gradient Lens Corporation<sup>1</sup>

**Table A-4:** Specifications for BG30 Grin Rod

	BG30
Diameter in mm	3
$\lambda$ in nm	633
NA	0.19
2Q (degree)	21.5
1/4 Pitch Length in mm	20.67
Pitch Length in mm	82.67
1/4 Pitch EFL in mm	7.97448
$N_{00}$ Base Index	1.643
$N_{10}$ in $\text{mm}^{-2}$	-0.0048
DN	-0.0107
$\sqrt{A}$ in $\text{mm}^{-1}$	0.076

### Refractive Index Profile

$$N(r) = N_{00} + N_{10}r^2$$

$$N_{00} = \text{Base Index}$$

$$A = -2N_{00}/N_{10}$$

## A-2.6 Detectors: ARX-GP Antel<sup>†</sup>

### Photosensitive Surface Dimensions

Diameter	300 $\mu\text{m}$
Area	0.07 $\text{mm}^2$
Distance From Housing Front Surface	2.0 $\pm$ 0.1 mm
Distance From Window Front Surface	0.5 $\pm$ 0.05 mm

### Absolute Maximum Ratings

Average Power Dissipation	100 mW
Reverse Bias Voltage	-30 V
Peak Output Voltage	-400 mV

### Electrical/Optical Characteristics

Temporal Response ( into 50 $\Omega$ )	
Device Type	Si-PIN
Risetime	<210 ps
Full Width @ Half Max Pulse Response	<370 ps
Bandwidth (3dB)	DC to 2 GHz

### Responsivity ( into 50 $\Omega$ )

V/W	380
As a Density	28 V/W/ $\text{mm}^2$
Minimum Detectable Signal @ S/N = 1	3.5 $\mu\text{W}$

Peak Output Voltage	-400 mV
Output Impedance	50 $\Omega$
Spectral Response 10% pts. Standard Window	500 nm to 1650 nm Glass

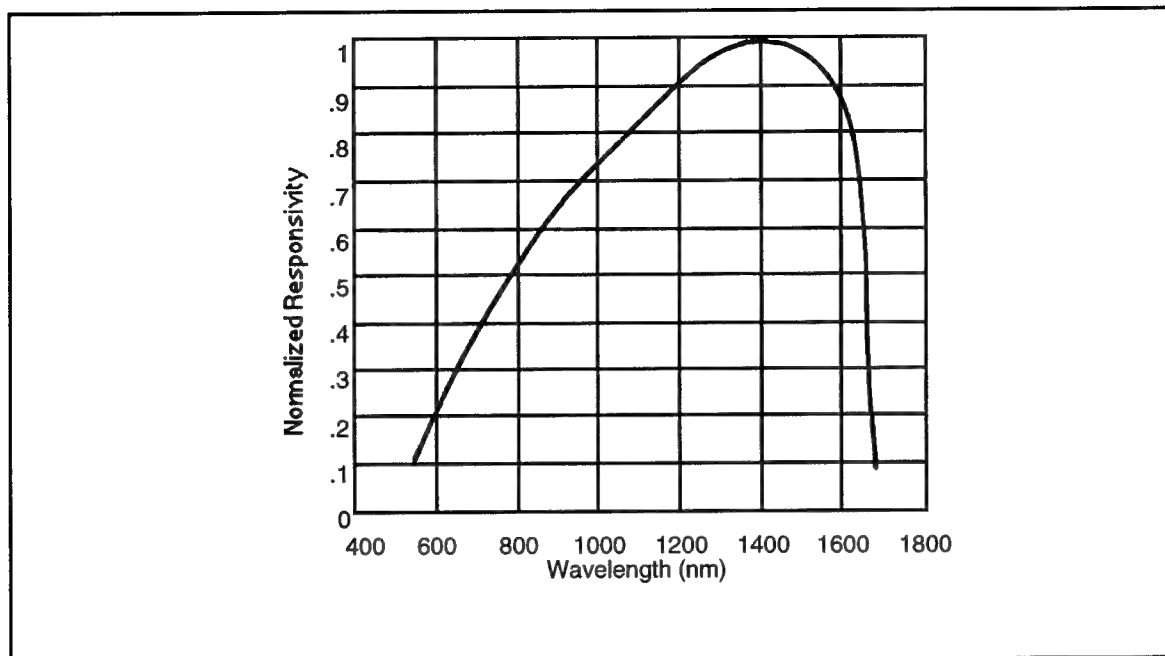


**Figure A-9.** Responsivity of ARX-GP Detector

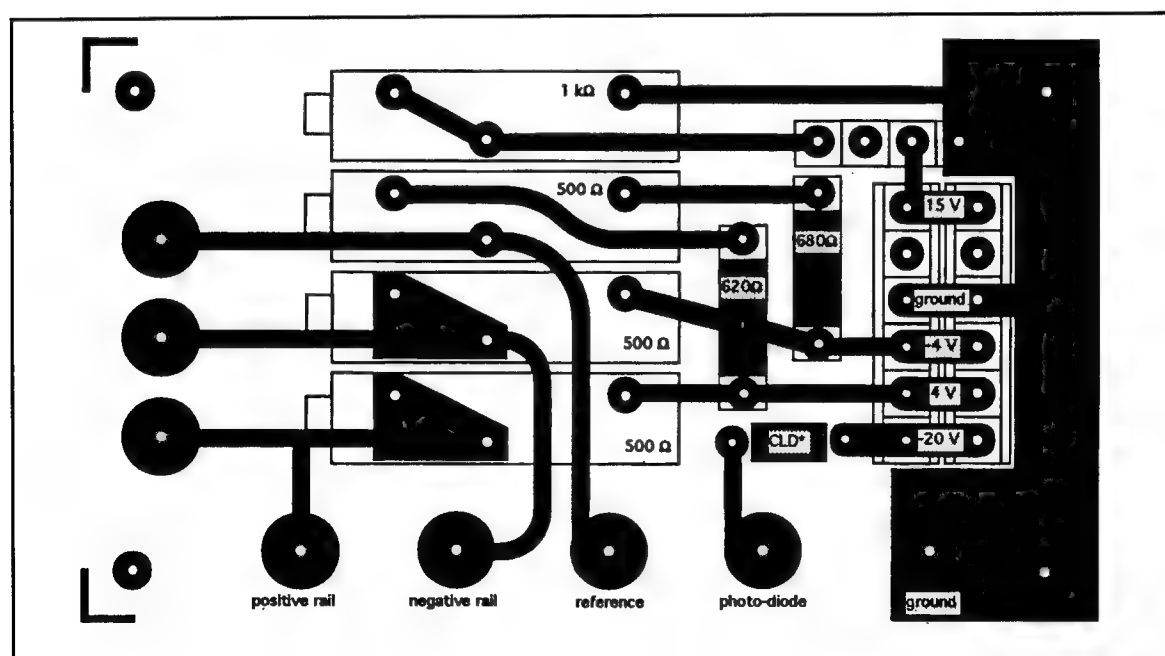


**Figure A-10.** Bias Circuit for ARX-GP Detector

## A-2.7 Matrix Shutter: MSS 4 x 5 NM Laser Products Inc.<sup>1</sup>

Array Size	4 x 5
Shutter Aperture (Diameter)	3.0 mm
Aperture Spacing (Center to Center)	7.0 mm

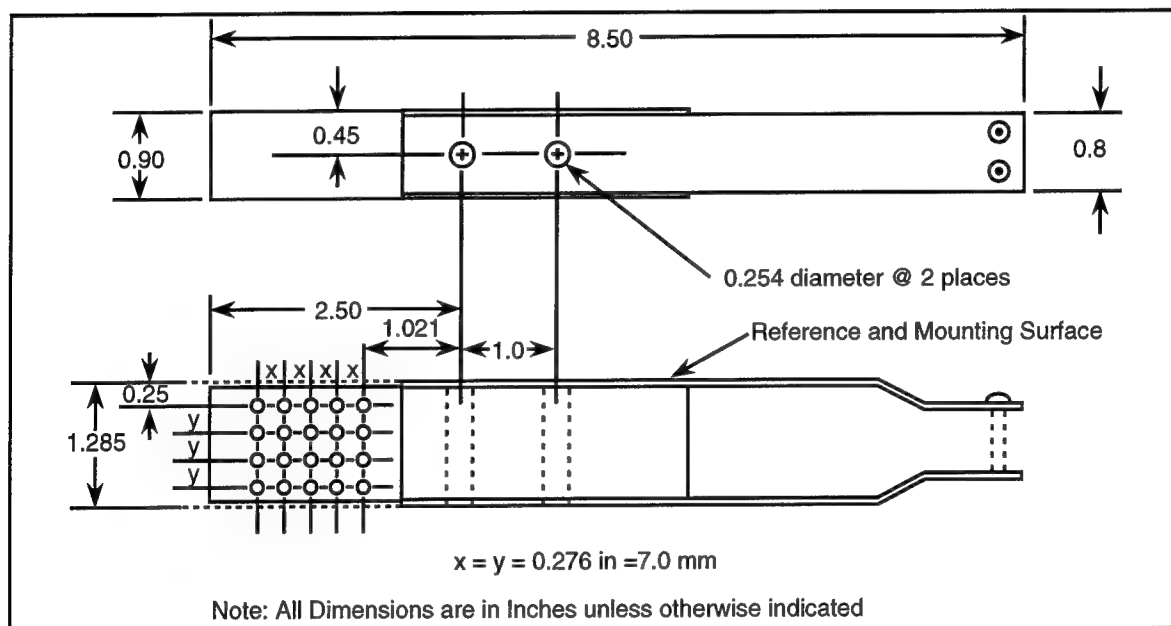


**Figure A-11. MSS4X5 Matrix Shutter Mechanical Drawing**

### Programming the Matrix:

To program the matrix, two ASCII codes are sent over the IEEE bus. The first code sets the switches into the desired position. The second code resets the drivers to accept the next data point.

The programming data must be sent as an ASCII code. This is accomplished in HP Basic and in other programming languages, by sending the number in quotes. For example, to send ASCII code 1 over the IEEE bus, the following HP Basic is required:

```

ASSIGN @MAT to 712
OUTPUT @MAT;"1";
OUTPUT @MAT1"1";

7=HPIB Card, 12=Matrix
OUTPUT ASCII CODE 1 to MATRIX
RESET MATRIX

```

Data on the IEEE bus is a single 8 bit word. The matrix data consists of two, 4 bit words, contained within the IEEE 8 bit word. The following is the programming data:

<b>POSITION</b> (First 10) Position)	<b>IEEE ASCII</b>	<b>MATRIX DATA 2</b> <b>IEEE 8765</b>	<b>MATRIX DATA 1</b> <b>4321</b>
1	1	0000	0001
2	2	0000	0010
3	3	0000	0011
4	4	0000	0100
5	5	0000	0101
6	6	0000	0110
7	7	0000	0111
8	8	0000	1000
9	9	0000	1001
10	10	0000	1010
(Second 10 Position)			
11	16	0001	0000
12	32	0010	0000
13	48	0011	0000
14	64	0100	0000
15	80	0101	0000
16	96	0110	0000
17	112	0111	0000
18	128	1000	0000
19	144	1001	0000
20	160	1010	0000
ALL OFF	0	0000	0000

### Changing the Address:

The Matrix is currently set to address "12"

To change the address, the address pins on the IEEE board are changed accordingly. The address line assignment follows:

<b>ADDRESS LINES</b>	<b>ADDRESS</b>
EDCBA	
01100	12

See connector pin-out for location of address lines.



## IEEE BOARD

Pin 1-Top of board with fingers pointing to the left.

PIN	Thru Hole	PIN NAME	CONNECTS TO
1	+5VDC		
2	o	A	GND
3	o	B	GND
4	o	C	+5VDC ADDRESS=12
5	o	D	+5VDC
6	o	E	GND
7	NO CONNECTION		
8	o	D108	DRIVER BOARD-TOP 12
9	o	D107	DRIVER BOARD-TOP 13
10	o	D106	DRIVER BOARD-TOP 14
11	o	D105	RIVER BOARD-TOP 15
12	o	D104	DRIVER BOARD-BOT 15
13	o	D103	DRIVER BOARD-BOT 14
14	o	D102	DRIVER BOARD-BOT 13
15	o	D101	DRIVER BOARD-BOT 12
16	o	DATA VALID	DRIVER BOARD-TOP 30
17	o	D108	IEEE CONNECTOR Pin 17
18	o	D107	IEEE CONNECTOR Pin 16
19	o	D106	IEEE CONNECTOR Pin 15
20	o	D105	IEEE CONNECTOR Pin 14
21	o	D104	IEEE CONNECTOR Pin 4
22	o	D103	IEEE CONNECTOR Pin 3
23	o	D102	IEEE CONNECTOR Pin 2
24	o	D101	IEEE CONNECTOR Pin 1
25	o	DAV	IEEE CONNECTOR Pin 7
26	o	IFC	IEEE CONNECTOR Pin 10
27	o	ATN	IEEE CONNECTOR Pin 12
28	o	RESET	DRIVER BOARD-BOT 30
29	o	NRFD	IEEE CONNECTOR Pin 8
30	o	NDAC	IEEE CONNECTOR Pin 9
31	o	GND	

## DRIVER BOARD

PIN 1-Top of board with fingers pointing to the left.

Staircase copper traces between IC's is up. This is the top of the board. Pin numbers are referred to TOP (This side) and BOT (Other side).

PIN	TOP PIN NAME	BOT PIN NAME	DRIVER BOARD #2
1	+5VDC	NO CONNECTION	
2	NO CONNECTION	1-10	(3-1)
3	NO CONNECTION	1-9	(3-1)
4	NO CONNECTION	1-8	(3-1)
5	NO CONNECTION	1-7	(3-1)
6	NO CONNECTION	1-6	(3-1)
7	NO CONNECTION	1-5	(3-1)
8	NO CONNECTION	1-4	(3-1)
9	NO CONNECTION	1-3	(3-1)
10	NO CONNECTION	1-2	(3-1)
11	NO CONNECTION	1-1	(3-1)
12	D108	D101	
13	D107	D102	
14	D106	D103	
15	D105	D104	
16	NO CONNECTION	NO CONNECTION	
17	NO CONNECTION	NO CONNECTION	
18	NO CONNECTION	NO CONNECTION	
19	NO CONNECTION	NO CONNECTION	
20	NO CONNECTION	2-10	(3-2)
21	NO CONNECTION	2-9	(3-2)
22	NO CONNECTION	2-8	(3-2)
23	NO CONNECTION	2-7	(3-2)
24	NO CONNECTION	2-6	(3-2)
25	NO CONNECTION	2-5	(3-2)
26	NO CONNECTION	2-4	(3-2)
27	NO CONNECTION	2-3	(3-2)
28	NO CONNECTION	2-2	(3-2)
29	NO CONNECTION	2-1	(3-2)
30	DATA VALID	NO CONNECTION	
31	NO CONNECTION	GND	

**+5VDC CONNECTS TO:**

IEEE BOARD PIN 1  
IEEE BOARD PIN 3  
IEEE BOARD PIN 5  
DRIVER BOARD PIN TOP 1

**GND CONNECTS TO:**

IEEE BOARD PIN 2  
IEEE BOARD PIN 4  
IEEE BOARD PIN 6  
IEEE BOARD PIN 31  
DRIVER BOARD PIN BOT 31  
IEEE CONNECTOR PIN 13  
IEEE CONNECTOR PIN 18 THRU 25

<sup>1</sup>This information has not been experimentally verified by the authors.

## Appendix B:

### MATLAB Software for Beam Pattern Simulation

```
% This Matlab program generates and plots simulated beampatterns for
% a phased array radar. The simulation is based on an N element
% line array. For our purposes, we measured and recorded (stored)
% data (magnitude vs. frequency and phase vs. frequency) on all
% twenty channels of the 4x5 L-Band phased array. This program
% prompts the user for the row (5 elements per row) of interest and
% also for the frequency of interest. It performs an FFT on the
% magnitude and phase data at the frequency of interest and
% plots the beampattern (magnitude vs. angle). The maxima is
% determined and the deviation from that maxima to the desired steer
% angle is the squint.

clear

% Load File "Broadside" which contains the measured values of
% magnitude vs. frequency and phase vs. frequency into matrices
% mag_broadside and phase_broadside respectively. Matrices
% mag_broadside and phase_broadside are 4x1005 elements each.
% mag(1,1) is a 201 element array containing the magnitude vs.
% frequency data for radar element(1,1) in our 4x5 array. f1=1.25
% GHz and f201=1.35 GHz.
%
% mag(1,1) = [mag1,1@f1, mag1,1@f2, mag1,1@f3, ....., mag1,1@f201]
%
% mag_broadside = [mag(1,1), mag(1,2), mag(1,3), mag(1,4), mag(1,5);
%                  mag(2,1), mag(2,2), mag(2,3), mag(2,4), mag(2,5);
%                  mag(3,1), mag(3,2), mag(3,3), mag(3,4), mag(3,5);
%                  mag(4,1), mag(4,2), mag(4,3), mag(4,4), mag(4,5)]

load BroadSide

% Prompt user for ROW of Data (mag_broadside and phase_broadside)
% choose 1,2,3, or 4.

row = input('Enter the Row of Data to use(1,2,3, or 4): ');

% Prompt user for desired frequency within the wideband TX signal.

freq = input('Enter the desired frequency in GHz (x10-9): ');
freq_index = ((freq-1.25)/0.5e-3)+1; % Sets index to access the
% appropriate frequency info
% 1e6 for 200pts

freq_index = round(freq_index);

% Prompt user for desired steer angle.

a = input('Enter the desired steer angle in degrees: ');
```

```

%      Define variables and constants.

max_y = [0];
N = 5;
A = a*pi/180;
fc = 1.3;
d = .3/(2*fc);
m = 1024;
Y = 0;
theta = pi/m*(-m/2:m/2);
theta_deg = (180/pi)*theta;
L = 0.3/freq;

Y = 2*pi*(d/L)*sin(theta);
mag_s=mag_broadside;
phase_s=phase_broadside*(pi/180);
bmstr = round((a + 90)/(180/(m-1))+1);

%      Build a N element vector containng the data at the frequency of
%      interest.

for i=1:N,
    offset=(i-1)*201+freq_index;
    Ys(i) = phase_s(row,offset);
end

%      This is a manual FFT (ie. used in lieu a library function or
%      tool).

for s = 1:m+1
    h = [0];
    for r = 1:N
        h = mag_s(r)*exp(j*Ys(r)-j*(r-1)*Y(s)) + h;
    end
    if abs(h) > max_y
        max_y = abs(h);
        k(1) = s;
    end;
    y(s) = h;
end

```

```

% Determine the index for the upper 3dB point.

for s = bmstr:m
    if abs(y(s)) <= abs(.707106781*max_y)
        k(2) = s;
        break;
    end
    if s == m
        for t = 1:m
            if abs(y(t)) <= abs(.707106781*max_y)
                k(2) = m + t;
                break;
            end
        end
    end
end

% Determine the index for the lower 3dB point.

for s = bmstr:-1:1
    if abs(y(s)) <= abs(.707106781*max_y)
        k(3) = s;
        break;
    end
    if s == 1
        for t = m:-1:1
            if abs(y(t)) <= abs(.707106781*max_y)
                k(3) = m - t;
                break;
            end
        end
    end
end

BW = (k(2)-k(3))*(180/(m)); % Computing the 3dB beamwidth

% Calculate and plot the antenna pattern

hold
G = 10*log10((abs(y/max_y)).^2); % converts to dB
plot(theta_deg,G,'r--'); % plots mag vs. angle
axis([-90 90 -50 0]);
title('');
title(['Antenna Pattern , Steered to ',num2str(a),' Degrees, Frequency ',num2str(freq),' GHz']);
xlabel('Angle (degrees)');
ylabel('Power (dB)');
grid on
hold on
level_3dB = -3.0 * ones(size(theta));
plot(theta_deg,level_3dB,'c--');
hold off
[e1,e2] = max(G); % locates maxima
TTD1=theta_deg(e2)
set(gcf,'DefaultTextColor','black')
text(-50,-7,['dash - Photonic TTD (',num2str(theta_deg(e2)),' Deg)'])

```

***MISSION***  
***OF***  
***ROME LABORATORY***

Mission. The mission of Rome Laboratory is to advance the science and technologies of command, control, communications and intelligence and to transition them into systems to meet customer needs. To achieve this, Rome Lab:

- a. Conducts vigorous research, development and test programs in all applicable technologies;
- b. Transitions technology to current and future systems to improve operational capability, readiness, and supportability;
- c. Provides a full range of technical support to Air Force Materiel Command product centers and other Air Force organizations;
- d. Promotes transfer of technology to the private sector;
- e. Maintains leading edge technological expertise in the areas of surveillance, communications, command and control, intelligence, reliability science, electro-magnetic technology, photonics, signal processing, and computational science.

The thrust areas of technical competence include: Surveillance, Communications, Command and Control, Intelligence, Signal Processing, Computer Science and Technology, Electromagnetic Technology, Photonics and Reliability Sciences.